UNIVERSITY OF OKLAHOMA

GRADUATE COLLEGE

FESHBACH OPTIMIZED PHOTOASSOCIATION OF RUBIDIUM DIMERS

A DISSERTATION

SUBMITTED TO THE GRADUATE FACULTY

in partial fulfillment of the requirements for the

Degree of

DOCTOR OF PHILOSOPHY

By

SEAN PATRICK KRZYZEWSKI
Norman, Oklahoma
2015

FESHBACH OPTIMIZED PHOTOASSOCIATION OF RUBIDIUM DIMERS

A DISSERTATION APPROVED FOR THE
HOMER L. DODGE DEPARTMENT OF PHYSICS AND ASTRONOMY

BY

Dr. Eric R. I. Abraham, Chair

Dr. Michael Morrison

Dr. Deborah Watson

Dr. John Moore-Furneaux

Dr. Susan Postawko

Acknowledgments

First, I would like to thank my advisor, Eric Abraham. He has been a constant source of support and ideas. His knowledge of experimental physics has been invaluable over the years. Second, I would like to thank my lab mate Dr. Thomas Akin. He began working for Eric shortly before I did, and we have been working together for roughly 5 years. We began on the same experiment, but he soon after moved to a different subject. Even so, he has always been willing to help on my experiment, even at the detriment of his own. Without his help, this experiment would not have been possible.

Outside of the laboratory, I have been blessed with two brilliant and patient theory collaborators, James Dizikes and Michael Morrison. Michael has helped me fine tune my abilities in theoretical physics and scientific writing. As I leave the University of Oklahoma, I realize the value of these skills. James began the theoretical calculations of Feshbach optimized photoassociation when I started the experiment. His knowledge of the underlying physics far surpasses my own, and without his help, I would never have been able to convey the science to others. He has also been a constant friend with whom I can complain about the difficulty of the task we set out to complete long ago.

A number of other graduate students and staff have provided me with the help

and friendship I have needed throughout the years. This process would have been far less enjoyable without them.

Finally, I would like my family. They have been supportive of my decisions throughout graduate school and always provided advice and help when needed. Without them, I never would have made it through graduate school.

Contents

List of Figures

Abstract

We report the observation of three different Feshbach optimized photoassociation resonances. The observations are in agreement with theoretical predictions and prior experimental results except for the width of the transitions, which we find to be narrower. This thesis details the steps that lead to this result, including the construction of a cooling, trapping, and imaging apparatus for rubidium atoms.

We also present the design of a zero-crossing Zeeman slower for ^{85}Rb using rings of flexible permanent magnets. The design is inexpensive, requires no power or cooling, and can be easily attached and removed for vacuum maintenance. We show theoretically that such a design can reproduce a magnetic field profile of a standard zero-crossing Zeeman slower. Experimental measurements of a prototype and comparisons to theoretical simulations demonstrate the feasibility of the design and point toward future improvements.

Chapter 1

Introduction

The main goal of this work is progress towards measuring the complete vibrational spectrum of singly excited molecular potential energy curves for $^{85}Rb_2$. This is difficult because of the small wave function overlap between the scattering state and the final excited vibrational state, as will be discussed in Section II. Similar work has begun for other homogeneous alkali molecules, such as Li_2 [4].

One of the major motivations for measuring the vibrational structure of potential curves is the goal of improved efficiency in the creation and control of cold molecules. Molecules offer extra degrees of freedom as compared to atoms. Cold molecules offer properties to manipulate such as the dipole moment, the rotational structure, and Lambda doublet splitting that can be used for quantum computation [5, 6] and quantum memory [7]. Molecules with large polarizabilities can create degenerate Fermi gases with strong anisotropic interactions that could lead to information on Cooper pairs [8]. Cold molecules can be used for coherent control of chemical reactions [8, 9, 10]. They can also be used in tests of fundamental symmetries such as parity and time reversal [11, 12, 13], and in the variation of fundamental constants [14, 15, 16].

There are two methods for creating ultracold ground state molecules, starting with room temperature molecules and cooling them down or starting with cold atoms and forming molecules. Atoms can be cooled on cycling transitions (which will be discussed in Chapter 2) down to the micro to nano Kelvin regime. Molecules do not have closed cycling transitions because of their rich electronic structure. There are other cooling mechanisms for molecules, but these cannot reach the same temperatures as laser cooled atoms (μK versus mK [17]. Therefore, molecules created from cold atoms can be at a much lower temperature than cooled molecules.

There are three main methods for creating molecules from a cold atom source. In the first method, atoms are photoassociated into an excited molecular state by a single cw photon (Fig. 1.1 (a)). This creates an excited state molecule in a stationary state, where the probability wave function is concentrated at the outer turning point of the molecular potential. Only the energy levels near the dissociation limit need to be known to accurately model the interaction. The excited state molecule can spontaneously decay or be driven into a lower vibrational state by a second cw laser source [18]. Stimulated emission has created ground state molecules, but the molecules were in high vibrational levels [19]. This method fails to create ground state molecules in low vibrational levels because branching ratios preferentially populate the higher vibrational states.

Molecules can also be created by photoassociation via a pulsed laser source using one or two photons (Fig. 1.1 (b)). This technique uses a laser with a frequency

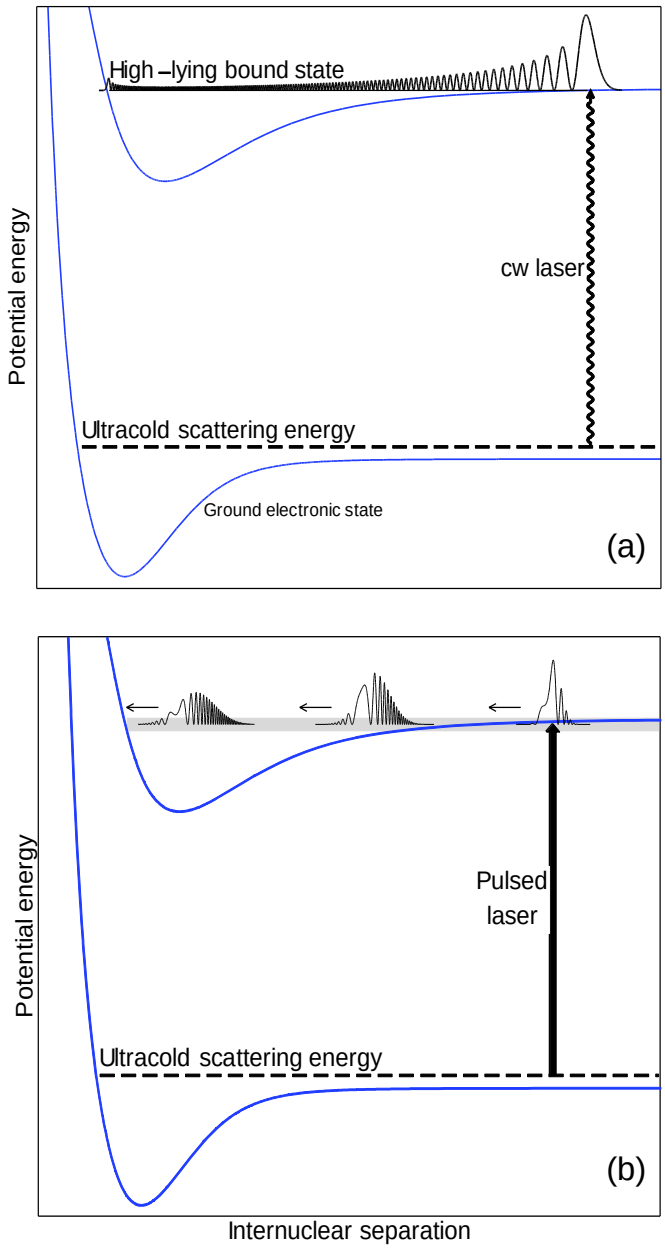

Figure 1.1: (a) One-photon cw photoassociation. (b) Pulsed laser photoassociation.

width that is large compared to the vibrational level spacing to photoassociate the atom into a superposition of excited states. The molecule is initially localized near the outer turning point of the superimposed vibrational states. The wave packet can propagate towards a smaller internuclear separation and decay. The overlap of the wave packet with the wave function of a low lying state is increased as compared to the outer turning points, and a larger number of low vibrational ground state molecules are formed as compared to cw photoassociation. Because the molecules move throughout the entire potential, it is necessary to know all of the vibrational states, from the near dissociation states to the states deep into the well [20, 21, 22]. Multiple experiments have created ground state molecules in this manner [23, 24, 25, 26]. Two photons can be used to improve the control over the final vibrational level of the ground state molecule [27, 28, 29, 30, 31, 32, 33].

The final method used to create ground state molecules is sweeping through a Feshbach resonance, which creates ultracold molecules directly [34]. A Feshbach resonance and stimulated Raman adiabatic passage has produced KRb molecules in their lowest vibrational state [35, 36].

In each of these 3 methods, an improved molecular potential leads to better knowledge of excitation frequencies and probabilities, spontaneous decay rates into the ground state and branching ratios from the excited state.

Beyond cold molecules, knowledge of the complete vibrational structure leads to improvements in quantum information science and atomic clocks. Trap loss via

ground and excited state collisions leads to decoherence and limited trap lifetimes [37] in clock states. An expanded knowledge of the potentials will reduce the systematic errors from these effects. Increased accuracy in molecular potentials also leads to an expanded knowledge of precision measurements such as retardation effects [38].

1.0.1 Singly Excited Potentials of Diatomic Rubidium

The literature is rich with publications on molecular potentials and notation ([39] and references therein). For the purpose of this discussion, we are only interested in the singly excited potentials for diatomic rubidium and where these potentials are unknown.

The interaction between the atoms in a homogeneous diatomic molecule is determined by the distance between the atoms R, and is labeled by its Hund's case. For small R, the molecular states are best described by Hund's case (a). The electronic orbital angular momentum $\vec{L}$ and spin angular momentum $\vec{S}$ are coupled to the internuclear axis $\vec{R}$. The states are designated by $\Lambda_{g/u}^{+/-}$, where Λ is the projection of $\vec{L}$ on $\vec{R}$, g/u describes the symmetry when the electron's position is reflected through the center of mass, and $+/-$ is the symmetry through a plane containing the nuclei. For large R, the Hund's case (c) best characterizes the system. The spin-orbit interaction is the relevant energy scale, and $\vec{L}$ and $\vec{S}$ uncouple from the internuclear axis [40]. The state is denoted as $\Omega_{g/u}^{+/-}$, where Ω is the projection of $\vec{J} = \vec{L} + \vec{S}$ on $\vec{R}$, and the rest are the same as Hund's case

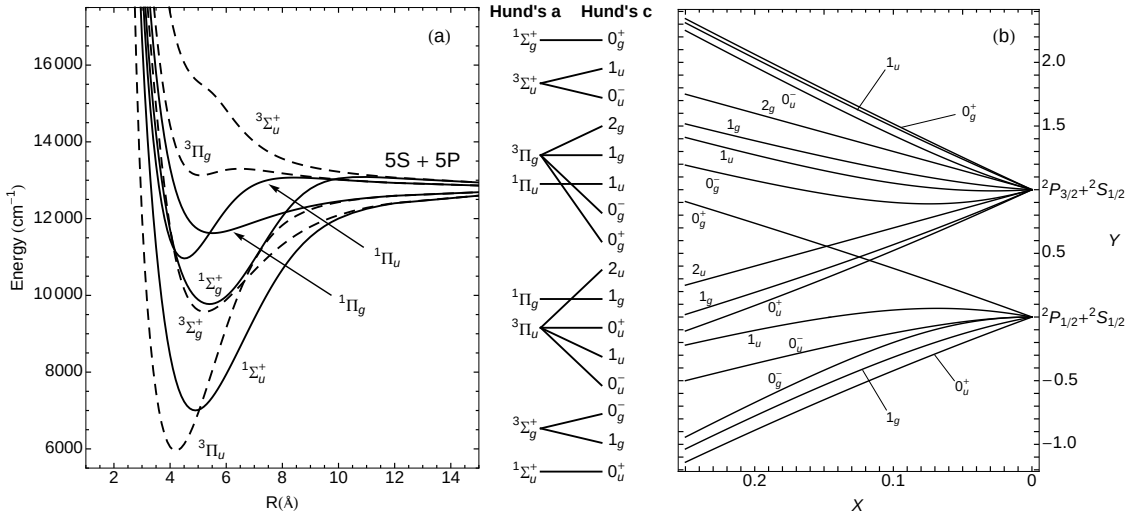

Figure 1.2: Potential curves for singly excited diatomic Rubidium associated with the Hund's case (a) and the Hund's case (c).

(a). Figure 1.2 shows the potential curves for singly excited diatomic Rubidium from Hund's case (a) [41] and how they connect to the Hund's case (c) [42]. The separation between atoms at large R (Hund's case (c)) is parameterized by $X = A/9\Delta R^3$, where Δ is the atomic fine-structure splitting, and A is the square of the radial atomic dipole matrix element [42]. The vertical axis in Fig 1.2(b) is normalized to Δ. The table below reflects the amount of knowledge of vibrational levels for the various states of $^{85}Rb_2$. The table is categorized by whether the outer turning point of the vibrational level is in the Hund's case (a) or (c) region of the potential. As seen from the table, there are still large areas of the excited potential that are unknown.

Hund's case (a)			Hund's case (c)		
state	% of well depth covered by experiment	reference	state	energy range covered from dissociation	reference
$^3\Pi_u$	70%	[43, 44]	$0_g^-(P_{1/2})$	1.5 – 12.5 cm^{-1}	[45]
$^1\Sigma_u^+$	60%	[43, 44]		1.8 – 21.2 cm^{-1}	[46]
$^3\Sigma_g^+$	< 20%	[47, 48]	$0_u^+(P_{1/2})$	70 cm^{-1}	[49]
$^1\Pi_g$	80%	[50]		0.7 – 12.5 cm^{-1}	[45]
$^1\Sigma_g^+$	35%	[50, 51]	$1_g(P_{3/2})$	0.43 – 35 cm^{-1}	[52, 53]
$^1\Pi_u$	> 90%	[54]			

Chapter 2

Theory

This chapter will walk through an explanation of the theory related to cooling atoms, storing the atoms, transferring the atoms to an all optical trap, and inducing photoassociation and a Feshbach resonance. Each of these steps is crucial in the experiment with the ultimate goal of measuring Feshbach optimized photoassociation. The first step is the cooling of rubidium atoms to sub-milliKelvin temperatures.

2.1 Basic Slowing and MOT Theory

2.1.1 Doppler Cooling

Consider a two level atom with an excited and ground state e and g, respectively, with energy difference $\hbar\omega_0$ as seen in Fig. 2.1. The atom interacts with a laser at frequency ω_l that is slightly detuned to the red of the atomic transition, given by

$$\delta = \omega_l - \omega_0, \tag{2.1}$$

and is counter-propagating with the atom (Fig. 2.2).

Absorption of the near resonant photon causes a change in the momentum of

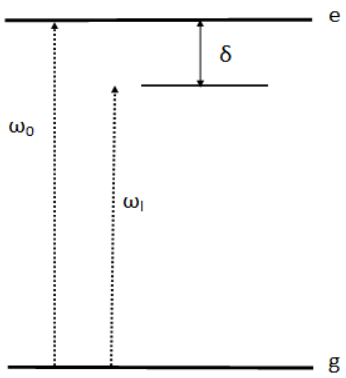

Figure 2.1: Simple two-level atomic energy diagram. A transition is driven from the ground state g to the excited state e via a photon of frequency ω that is detuned from resonance by an amount δ.

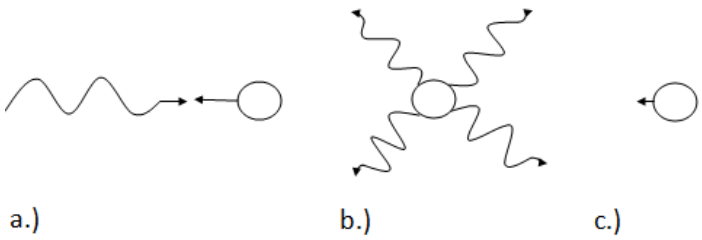

Figure 2.2: a.) An atom absorbs a photon and it is changed from the ground to the excited state. The atom feels a kick opposite its direction of motion from the photon. b.) The atom spontaneously decays to the ground state and emits a photon in a random direction. c.) After many absorption and emission events, the net effect is the slowing of the atom.

the atom opposite its direction of motion, and exerts a force on the atom, given by [43]:

$$\mathbf{F} = \frac{\hbar \mathbf{k} s_0}{2(1 + s_0 + (2(\delta - \mathbf{k} \cdot \mathbf{v})/\Gamma)^2))}, \tag{2.2}$$

where $\mathbf{k}$ is the wave vector of the photon, Γ is the linewidth of the transition, and s_0 is the saturation parameter, given by I/I_s, where I is the intensity of the laser beam and I_s is the saturation intensity of the driven transition. This results in the atom being slowed opposite its direction of motion by momentum $\hbar k$, and changes the internal state from the ground to the excited state. The atom will emit a photon as it returns to the ground state, either through stimulated emission because of the near resonant laser field, or through spontaneous decay and emission of a photon. If the intensity of the slowing laser is low compared to the saturation intensity, spontaneous emission will dominate, and the photon will be emitted in a random direction after the lifetime τ (tens of nanoseconds for alkali metals). Although our laser intensity in the experiment will be larger than the saturation intensity, the low intensity theory still explains the basic physics because enough of the excited atoms undergo spontaneous emission. Over thousands of cycles, there is no net direction of the spontaneously emitted photon, and the only net change in momentum is opposite the direction of the motion of the atom.

If we introduce a second, equally detuned laser counter-propagating with the first, the atom can be cooled in one-dimension, regardless of its initial direction of motion in that dimension. The force that the atom feels in each direction becomes

[43]

$$\mathbf{F}_{\pm} = \pm\frac{\hbar\mathbf{k}\Gamma}{2}\frac{I/I_s}{1 + I/I_s + (2(\delta \mp \mathbf{k}\cdot\mathbf{v})/\Gamma)^2}, \tag{2.3}$$

where the sign denotes the direction of the photon relative to the atom. After many absorption and emission cycles, the Doppler shift is small ($\mathbf{k}\cdot\mathbf{v} \ll \Gamma$), and the net force on the atom can be expanded in a power series, approximated as [43],

$$\mathbf{F} = \frac{8\hbar k^2 \delta s_0 \mathbf{v}}{\Gamma(1 + s_0 + (2\delta/\Gamma)^2)^2}. \tag{2.4}$$

The force is proportional to $\mathbf{v}$, and can be interpreted as a damping force of the form $\mathbf{F} = \beta\mathbf{v}$. If the system is expanded from 2 counter-propagating beams to 3 sets of orthogonal beams (2 counter-propagating in each dimension), this creates a sort of "optical molasses", where the atoms are not trapped, but are slowed. Their temperature is determined by the spontaneous emission given by [43],

$$T_D = \frac{\hbar\Gamma}{2k_B}. \tag{2.5}$$

Some initial experiments performed with optical molasses found the temperature of the sample to be much colder than this limit [44]. This was explained through the mechanism of sub-Doppler cooling.

2.1.2 Sub-Doppler Cooling

To explain sub-Doppler cooling, we must move beyond the two-level atom and include the magnetic sub-levels of the ground state. Each of these sub-levels will experience a different energy shift, called the light shift,

$$\Delta E_g = \frac{\hbar\delta s_0 C_{ge}^2}{1 + (2\delta/\Gamma)^2}, \tag{2.6}$$

where C_{ge} is the Clebsh-Gordon coefficient. When making the transition from $J = 3/2$ to $J = 1/2$ as we will see momentarily, the light shift is 3 times larger for the $m_F = 1/2$ than the $-1/2$ state when driven by σ^+ light, and the reverse when driven by σ^-. When the atoms are optically pumped, the state with the larger light shift (which corresponds to lower energy) will contain a larger fraction of the population.

There are two types of sub-Doppler cooling, $lin \perp lin$, and σ^+/σ^-. Each of these schemes are only rigorously true for low J transitions, which is not the case for Rb, but the basic theory is still applicable and fairly accurate. For a more rigorous treatment, see [43].

In $lin \perp lin$, two counter-propagating beams with orthogonal linear polarization create a standing wave pattern that leads to a rotating polarization gradient. As seen in Fig. 2.3, the overlap of the two beams leads to an alternation between σ^+ light, to linear and to σ^-. To begin, take an atom at z=0 in the state F=1/2,

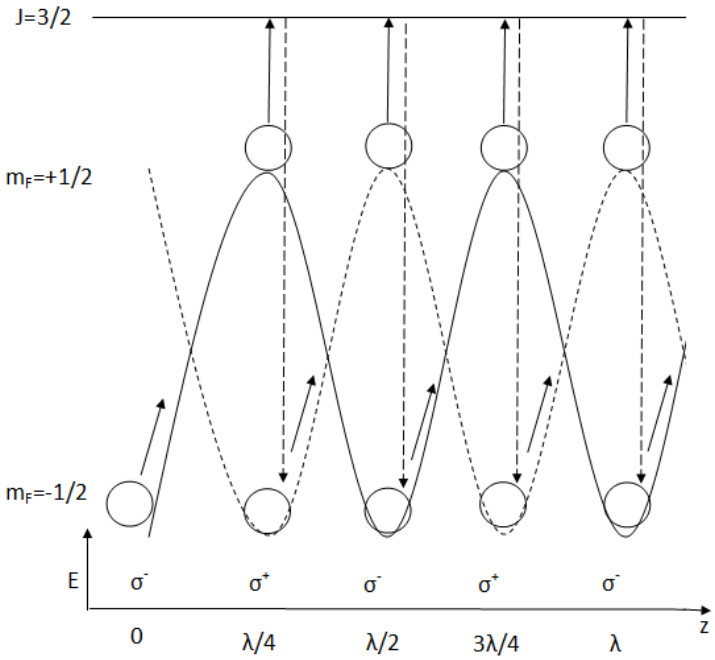

Figure 2.3: An atom begins at z=0 in the F=1/2 state, where the atom sees the light as σ^-. The σ^- light drives most of the atoms to $m_F = -1/2$ state due to the light shift. At the peak, the atom absorbs a photon (assuming the laser has the correct detuning) and is excited into the $F = 3/2$ state. It decays to the $m_F = 1/2$ state because of the σ^+ light. The energy of the photon radiated is higher energy than the one absorbed, leading to a loss in energy from the atom.

where the light is initially σ^-. The σ^- light drives most of the atoms into the to $m_F = -1/2$ state due to the larger light shift. As the atom moves through the field, the atom losses kinetic energy as it moves to a higher potential and becomes less strongly coupled to the light field. At the peak, the atom absorbs a photon (assuming the laser has the correct detuning) and is excited into the $F = 3/2$ state. However, the polarization of the light has changed to σ^+, and the atom preferentially decays to the $m_F = 1/2$ state as it is lower in energy. Therefore, the energy of the photon radiated is at a higher energy than the one absorbed, leading to a loss in energy from the atom. As the atom moves along, it once again is climbing the hill, converting kinetic to potential energy as the field changes to σ^- polarization. At the peak, the atom absorbs a photon, is excited to the $F = 3/2$ state, and decays down to the $m_F = -1/2$ state which is energetically lower than the $m_F = 1/2$, releasing energy from the system. This process repeats and the atom continuously loses energy until the atom can no longer reach the peak of the hill. Because of the continuous climbing of a hill, this method is also referred to as Sisyphus cooling.

For σ^+/σ^- cooling, the combination of the two counter-propagating beams leads to a field with constant magnitude and linear polarization, forming a helix [1] Figure 2.4. We will not have a changing light shift to cool the atoms as we had in Sisyphus cooling. Light shifts of the ground state sub-levels are constant, but they have different energies because of the different values of m_F. For our system,

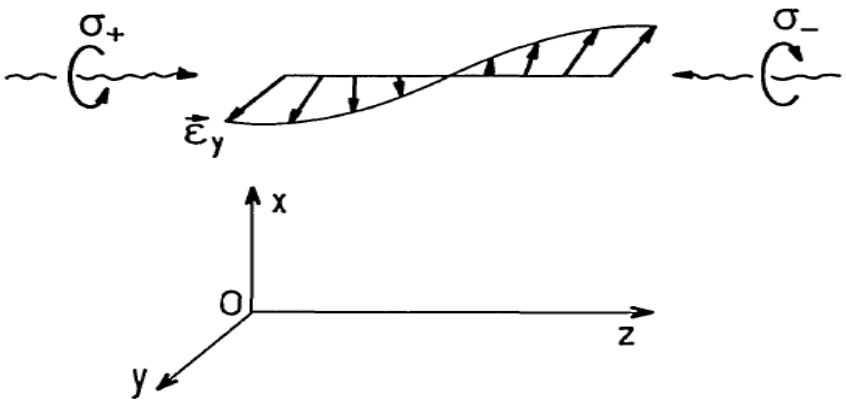

Figure 2.4: The combination of two counter-propagating circularly polarized beams leads to a linearly polarized beam. The angle of the linear polarization rotates in space. The figure is taken from [1]

we will work only with F=1 to F=2 transitions. If the velocity of the atoms is 0, the atoms will collect in m_F=0 state. This can be understood when looking at the Clebsh-Gordon coefficients and branching ratios (Figure 2.5). The branching ratios into a m_F=0 state will be 9/17, while the +1 and -1 state will be 4/17., leading to a pile up in the m_F=0 state. You can also depict this via the light shift. In the zero velocity case, the light shift of the m_F=0 state is lower than either of the stretched states (the positive or negative extremes i.e. m_F=+1 or -1), making it more energetically favorable.

Now we will assume the atom moves with some velocity v, and we will take the frame where the polarization is in a fixed direction. Applying Larmors theorem, an inertial field will arise from the rotating frame [1]. This incorporates a new term into the Hamiltonian that couples ground state sub-levels. This term is

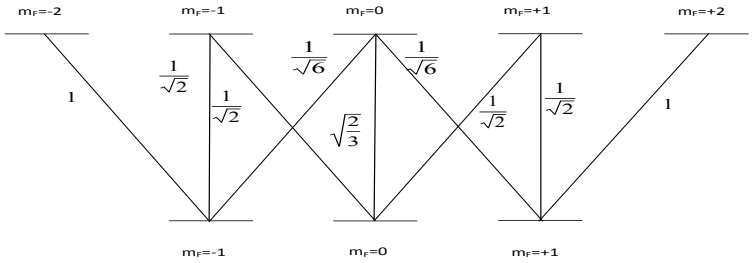

Figure 2.5: The Clebsh-Gordon coefficients for a F=1 to F=2 transition.

proportional to kv, where k is the wave vector. To first order, the inertial term leaves the energy unchanged. Depending on the direction of v and the detuning of the laser, the stretched states do not have the same populations. For a rigorous mathematical proof, see [1].

We can look at the two different scenarios of the atoms in each of the stretched states. First, assume the atom is moving in the positive z direction and the detuning is negative. If the atom is in the -1 state, it will be 6 times as likely to absorb a σ^- photon traveling towards the atom than a σ^+ photon traveling away from the atom. If the atom is in the +1 state, it will be 6 times as likely to absorb a σ^+ photon traveling towards the atom than a σ^- photon traveling away from the atom. This leads to a radiation pressure difference between the two polarizations, and the atom's motion will be damped. As described in [1], this leads to a viscous

damping force that goes as:

$$F \backsim \alpha v, \tag{2.7}$$

where α is the damping constant.

This phenomenon only works at very low velocities for a small range, unlike Doppler cooling, because of the small energy of the inertial term [1]. Eventually, the recoil limit is reached and the atoms are no longer slowed.

At this point, we have a source of cold atoms. However, the atoms are not confined, and will drift out of the interrogation region before they can be studied. Therefore, the atoms must be trapped and held in a small region. This will be done using a magneto-optical trap.

2.1.3 Magneto Optical Trap

All of the cooling techniques discussed thus far will only slow atoms, not trap them. The first laser based trap used to both cool and store neutral atoms is the magneto-optical trap (MOT) by Raab *et al.* [45]. The MOT begins in the same fashion of an optical molasses, but provides a position dependent restoring force that keeps the atoms in a specific region.

A diagram of the level structure and interaction of the MOT is given in Fig. 2.6. To explain the physics, we will assume a simple atomic picture of a two level atom, with $F = 0$ and $F = 1$, and motion only in 1-dimension. As seen in Fig. 2.6, a magnetic field created by a pair of anti-Helmholtz coils breaks the

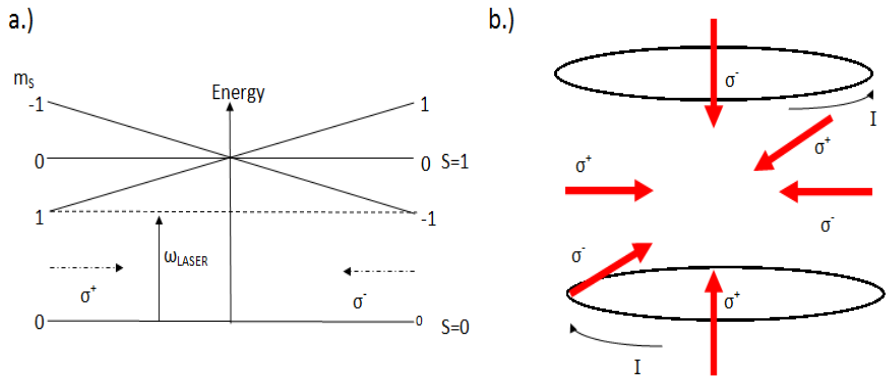

Figure 2.6: a.) The two-level once-dimensional cooling scheme for a magneto-optical trap. b.) The orientation of the laser beams, their polarizations, and the magnetic field coils for a magneto-optical trap.

degeneracy of the F=1 state into each of its magnetic sub-levels, m_F=0, ±1. The magnetic field at the center of the anti-Helmholtz coils goes to zero and no energy splitting is seen, but each side splits in opposite directions leading to a difference in the energy. Two counter-propagating beams with opposite circular polarization overlap with the magnetic field. When an atom moves away from B=0, the atom will absorb the light preferentially based on the polarization of the light. Looking from the left, the atom will absorb the σ^+ light and be excited into the $m_F = 1$ state. As the atom moves away from the center, it will be pushed back towards B=0. The atom will be less likely to absorb the σ^- light as it is further detuned from resonance, and will feel no force away from B=0. Thus, the main direction of force will be towards the center of the trap. The same principals are applied to the right hand side, except that the σ^- will be absorbed, pushing the atom back

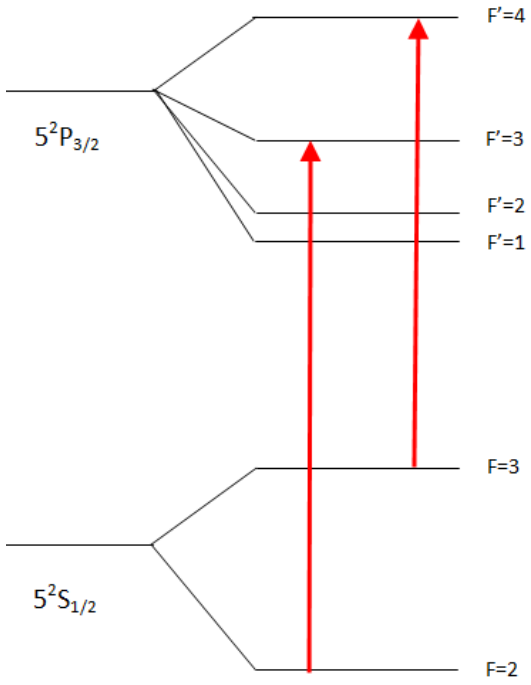

Figure 2.7: The energy levels used for the trapping ($F = 3 \rightarrow F = 4$) and re-pump ($F = 2 \rightarrow F = 3$) beams in a ^{85}Rb magneto-optical trap.

towards the center, and the σ^+ light will have no effect.

When expanding this concept to a multi-level system, we artificially create a two-level atom by driving cycling transitions (Fig. 2.7). For Rubidium 85, the trapping laser drives the transition between the F=3 to F'=4 state. The transition is driven via circularly polarized light, and the atoms populate one of the stretched states. The atoms decay from the F'=4 state preferentially to the F=3 due to dipole selection rules, and the process continues between these two states. This is referred to as a cycling transition. However, there is a possibility that the atom is excited into the F'=3 state, which can decay into the F=2 ground

state. Although the excitation into the F'=3 is very unlikely when compared to the F'=4 transition (roughly 1 out of a thousand), the large number of transitions per second leads to a build-up of atoms in the F=2 state that are unaffected by the trapping laser. This quickly leads to atom loss, and a MOT is not observed. A second laser called the re-pump is tuned to the F=2 to F'=3 state to prevent a build-up of atoms in the lower state. This leads to a majority of the atoms staying on the F=3 to F'=4 transition and the atoms are trapped. The intensity of the re-pump beam can be relatively small when compared to the trapping beams and does not need to be in all directions because its sole purpose is to depopulate the F=2 state. The trapping process happens on time scales of the spontaneous decay, and cools down a large number of atoms (10^9 for ^{85}Rb) within seconds to temperatures in the tens of μK.

At this point, the atoms are cold and held in a small region, but inducing a magnetic Feshbach resonance while the atoms are in the MOT will lead to energy level shifts from the quadrupole field. It will also prevent us from studying the effect of atoms specifically at the Feshbach resonance since the atoms will feel a different field based on their position in the quadrupole field. To circumvent this issue, we move into an all optical dipole trap.

2.2 Dipole Trap Theory

We begin with a semi-classical approach to the interaction of an intense laser beam interacting with a two-state atom. This approach is used for alkali atoms

because it reproduces actual results to within a few percent [46], and is sufficient for explaining the necessary physics.

We start with an atom in an electric field from a laser, where the electric field is described by,

$$\vec{E}(\vec{r},t) = \hat{\epsilon}E(\vec{r})e^{-i\omega_l t} + c.c., \tag{2.8}$$

where r is the position, t is the time, ω_l is the laser frequency, and $\hat{\epsilon}$ is the unit vector in the direction of the electric field. The electric field will induce a dipole moment $\vec{p}(\vec{r},t)$ in the atom, described as,

$$\vec{p}(\vec{r},t) = \hat{\epsilon}p(\vec{r})e^{-i\omega_l t} + c.c. \tag{2.9}$$

The relationship between the electric field and the dipole moment is,

$$\vec{p} = \alpha\vec{E}, \tag{2.10}$$

where α is the polarizability of the atomic cloud.

To find the polarizibility, we first assume a Lorentz model of the system [46]. This model assumes the nucleus is bound to the electron, the electron has a charge of $-e$, and a mass m_e that is much less than the mass of the nucleus. The two are attached as an oscillator with angular frequency ω_0, where ω_0 is the eigenvalue of the system and the atomic transition frequency. The position of the electron is

described as,

$$\ddot{x} + \Gamma_\omega \dot{x} + \omega_0^2 x = \frac{-e}{m_e} E(t). \tag{2.11}$$

We can make the same argument for the dipole moment [47], where

$$\ddot{p} + \Gamma_\omega \dot{p} + \omega_0^2 p = \frac{-e}{m_e} E(t). \tag{2.12}$$

Solving for p, we find [46],

$$p = \frac{e^2 E_0}{m_e} \frac{1}{(\omega_0^2 - \omega_l^2) + i\omega_l \Gamma_\omega}. \tag{2.13}$$

By relating this to the relationship between the induced dipole moment and electric field, we arrive at an expression for the polarizibility,

$$\alpha = \frac{e^2}{m_e} \frac{1}{\omega_0^2 - \omega_l^2 - i\omega_l \Gamma_\omega}, \tag{2.14}$$

where Γ_ω is the classical damping rate due to the energy loss defined as,

$$\Gamma_\omega = \frac{e^2 \omega^2}{6\pi\epsilon_0 m_e c^3}. \tag{2.15}$$

The polarizibility is a complex number whose real and imaginary parts lead to different physical phenomena. The real part of the polarizibility describes the dispersion, which is the interaction energy of the field with the electron. This is

used to write the potential energy of the electron in the laser field,

$$\begin{aligned} U_{dip} &= -1/2\langle pE\rangle \\ &= -\frac{1}{2\epsilon_0 c}\mathrm{Re}(\alpha)I(\vec{r}) \\ &= \frac{3\pi c^2}{2\omega_0^2}\left(\frac{\Gamma_\omega}{\omega_0-\omega_l}+\frac{\Gamma_\omega}{\omega_0+\omega_l}\right)I(\vec{r}), \end{aligned}$$

where $I(\vec{r}) = 2\epsilon_0 c|\vec{E}|^2$ is the intensity of the laser beam. The factor of $1/2$ is because the dipole is induced and not a permanent. The potential will determine trap depth, and therefore the number of atoms that will be transferred from a MOT to the optical dipole trap.

The imaginary part of the polarizability describes the absorption, which is related to the dissipation of energy or the scattering of photons off of the electron. Taking the imaginary part, the power absorbed is [46],

$$P_{abs} = \frac{\omega_0}{\epsilon_0 c}\mathrm{Im}(\alpha)I(\vec{r}). \tag{2.16}$$

If we consider the light to be a continuous flux of photons with energy $\hbar\omega_l$, we can write the scattering rate Γ_{sc} as,

$$\begin{aligned} \Gamma_{sc} &= \frac{p_{abs}}{\hbar\omega_l} \\ &= \frac{1}{\hbar\epsilon_0 c}\mathrm{Im}(\alpha)I(\vec{r}) \\ &= \frac{3\pi c^2}{2\hbar\omega_0^2}\left(\frac{\omega_l}{\omega_0}\right)^3\left(\frac{\Gamma_\omega}{\omega_0-\omega_l}+\frac{\Gamma_\omega}{\omega_0+\omega_l}\right)^2 I(\vec{r}). \end{aligned}$$

The value of Γ_{sc} partially sets the lifetime of the optical dipole trap, and thus, is extremely important for a long trap lifetime.

There are 3 regions where approximations can be made to simplify the equations for the potential and the scattering rate. They are near resonance, far from resonance, but still in the optical, and very far detuned. This thesis specifically works in the second regime, and the trap is commonly referred to as a far-off resonance trap, or FORT [48]. In this regime, the laser is far-detuned from the atomic transition, D1 or D2, and the rotating wave approximation ($\omega_l/\omega_0 \approx 1$) is used. The potential and scattering rate are simplified and re-written as

$$U_{dip} = \frac{3\pi c^2}{2\omega_0^3}\left(\frac{\Gamma_\omega}{\delta}\right) I(\vec{r}), \tag{2.17}$$

and,

$$\Gamma_{sc} = \frac{3\pi c^2}{2\hbar\omega_0^3}\left(\frac{\Gamma_\omega}{\delta}\right)^2 I(\vec{r}). \tag{2.18}$$

Writing the potential and scattering rate in this form illuminates two different points. First, the sign of the detuning determines whether the trap collects atoms at the minimum or maximum of the potential. For atom with $\Delta < 0$ (red detuned), the atoms will move towards the trap maximum. Applying this notion to the Lorentz model, it is the equivalent of the electron being driven in-phase with the electric field. For an atom with $\Delta > 0$ (blue detuned), the atoms move towards the intensity minimum. In the Lorentz model, this is the equivalent of the electron

being driving out of phase with the electric field. Second, the dipole potential is inversely proportional to the detuning, while the scattering rate is inversely proportional to the square of the detuning. Thus, a large detuning and high intensity leads to a large trap depth and a small scattering rate, ideal for most atom trapping.

So far only the semi-classical two level has been discussed. This model agrees to within a few percent of the experimental values for alkali metals because of the strong dipole allowed transition from the ground state. For a more in-depth coverage that includes a multi-level explanation, see [46].

A common method for creating a FORT is a single Gaussian beam. A collimated Gaussian beam of wavelength λ and waist ω_0 (not to be confused with the atomic transition frequency) is focused by a lens of focal length f. The beam waist after focusing, ω_0' is described as [49],

$$\omega_0' = \frac{\lambda}{\pi\omega_0} f, \tag{2.19}$$

and the Rayleigh range z_0', which describes the collimated length of the focus, by,

$$z_0' = \frac{\pi\omega_0'^2}{\lambda}. \tag{2.20}$$

From these, we can re-write the dipole potential using more experimentally relevant

parameters, as given by [50].

$$U(r,z) = U_0 \frac{\mathrm{e}^{-2r^2/\omega(z)^2}}{1+(\frac{z}{z_0'})^2}, \tag{2.21}$$

where,

$$U_0 = \frac{\hbar\gamma I_0}{24 I_{sat}} \left(\left(\frac{1}{\delta_{1/2}} + \frac{2}{\delta_{3/2}} \right) - g_f m_f (1-\epsilon^2)^{1/2} \left(\frac{1}{\delta_{1/2}} - \frac{1}{\delta_{3/2}} \right) \right), \tag{2.22}$$

where γ is the natural linewidth, I_0 is the peak intensity of the beam, I_{sat} is the saturation intensity of the transition, g_f is the Lande g factor, m_f is the Zeeman sub-level of the atom, $\delta_{1/2}$ and $\delta_{3/2}$ are the laser detunings from the D1 and D2 transition, respectively, and ϵ is the ellipticity of the beam. Normally, a linearly polarized beam ($> 99\%$) will not experience any decrease in the potential. However, it is worth noting that any significant ellipticity quickly leads to a decrease in the dipole trap potential [50].

For a red detuned trap like the one used in this work, the atoms will be collected at the focus of the beam. The size and density of trap will be determined by the Rayleigh range and the waist at the focus. A tighter focus, which implies a shorter Rayleigh range for the same initial pre-focused waist, will lead to a higher density. However, the loading efficiency decreases with a tighter focus. We balance the loading efficiency and trap size to maximize the number of atoms and density in our trap.

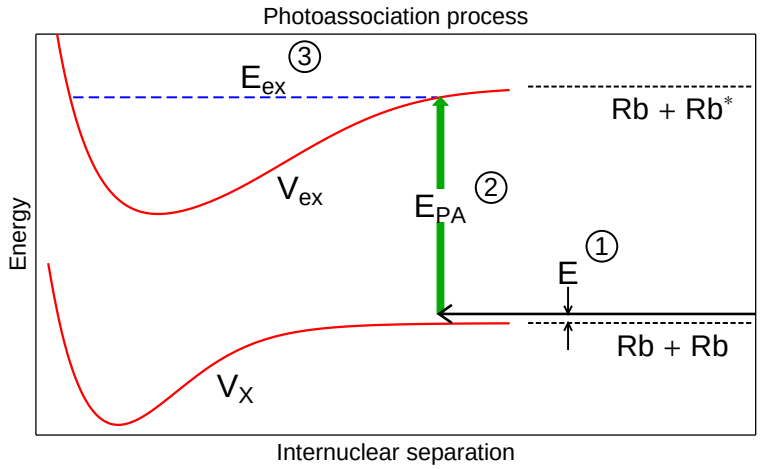

Figure 2.8: A diagram of the photoassociation process. (1) Two atoms in a trapped, ultracold gas collide with relative kinetic energy E. (2) The atoms absorb photons of energy E_{PA} from the laser. (3) The atoms are excited into a molecular state with energy E_{ex}. The figure is take from [2].

2.3 Photoassociation

Photoassociation has been important for a better understanding of a variety of atomic and molecular properties. It has allowed the study of long range interactions between atoms, of binding energies, and of atomic properties such as radiative lifetime, photodissociation, predissociation, and autoionizing [22]. It has also been used in studying retardation effects [38]. Retardation is the changing of molecular bong strength because of the finite time that information can be passed from one atom to another. Photoassociation studies the high vibrational levels whose properties can be connected to the separated atoms, leading to information on retardation. It also measures the scattering length, which at low-energy, determines whether or not an atom can Bose condense [38].

Photoassociation begins with two free incoming atoms at a temperature T under the influence of the ground state molecular potential (Fig 2.8). At long range and ignoring retardation effects, the potential goes as,

$$V = -C_6 R^{-6} + \frac{h^2 l(l+1)}{2\mu R^2}, \tag{2.23}$$

where C_6 is a van der Waals dispersion coefficient that describes the quadrupole interaction, R is the inter atomic separation, l is the partial wave, and μ is the reduced mass of the system. A photon of frequency ν_1 and energy $\hbar\omega_0 - kT$, where $\hbar\omega_0$ is the spacing between the ground and excited molecular states, interacts with the atoms, leading to the formation of a bound excited state molecule. For homogeneous atoms, the bound excited state potential is described as,

$$V = -C_3 R^{-3} + \frac{h^2 l(l+1)}{2\mu R^2}, \tag{2.24}$$

where C_3 is a van der Waals dispersion coefficient that describes the dipole interaction. This process is represented as [22],

$$K + K + h\nu_1 = K^*(\nu', J'), \tag{2.25}$$

where K is the atom, J is the rotational state, and ν is the vibrational state. Prior to laser cooling, the spread in the initial kinetic energy of atoms at room

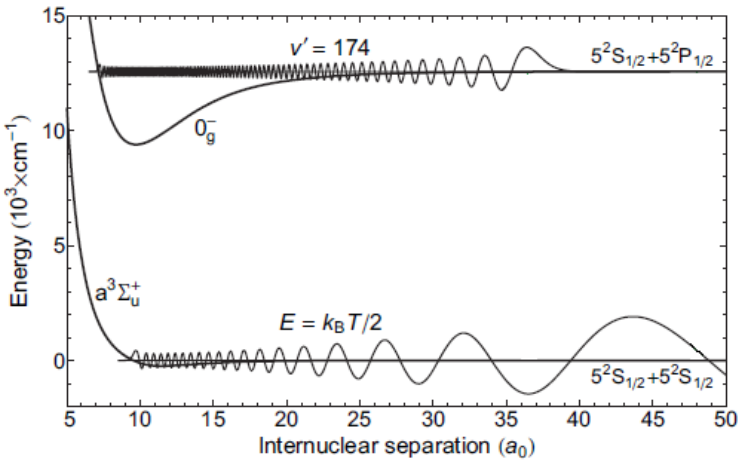

Figure 2.9: The wave function of the scattering state of two atoms and the 0_g^- potential for v'=174. The wave function overlap determines the photoassociation rate.

temperature was large (∼10 THz)[51]. For photoassociation to be effective, the spread of energy in the initial atoms must be near to or less than the linewidth of the photoassociation transition, usually in the tens of MHz. Photoassociation lines were not observed because the large spread in initial kinetic energy compared to the width of photoassociation transitions. With the advent of laser cooling and trapping, the small kinetic energy spread (sub MHz) of the incoming atoms relative to the vibrational level spacing allows for a single state to be populated [51]. An added benefit of low temperature is the small number of partial waves to consider for the scattering states (low l). To conserve angular momentum when transitioning to the bound molecule, the final product must also comprise of a relatively small number of partial waves needed for modeling [38]. This leads to a relatively simply spectra of the bound state, drastically simplifying analysis.

The rate at which the bound excited state molecules are formed (photoassociation rate) is [52]

$$K_{PA}(T,\omega_L) = \langle \frac{\pi v_{rel}}{k^2} \sum_{l=0}^{\infty} (2l+1)|S_{PA}(E,l,\omega_L)|^2 \rangle \tag{2.26}$$

where $v_{rel} = \frac{\hbar k}{\mu}$ is the velocity of the atoms, and $S_{PA}(E,l,\omega_l)$ is the S-matrix element. Averaging over a Maxwell-Boltzmann distribution at temperature T, the rate becomes

$$K_{PA}(T,\omega_L) = \frac{1}{hQ_T} \sum_{l=0}^{\infty} (2l+1) \int_0^{\infty} |S_{PA}(E,l,\omega_L)|^2 e^{(-E/k_B T)} dE \tag{2.27}$$

where

$$|S_{PA}(E,l,\omega_L)|^2 = \frac{\Gamma\gamma_s}{[(\delta + \frac{E-E_{v,J}}{\hbar})^2 + ((\Gamma+\gamma_s)/2)^2]} \tag{2.28}$$

where Q_T is the translational partition function, γ_s is the natural linewidth of the PA transition, $E = \frac{\mu v_{rel}^2}{2}$, $E_{v,J}$ is the bound state energy, and δ is the detuning of the PA laser from the atomic transition. Γ is the stimulated linewidth and given as

$$\Gamma = \frac{\pi I}{\epsilon_0 c} |\langle \phi_{v,J}|D_t(R)|\Psi_{\gamma=l,m_l}(E,R)\rangle|^2 \tag{2.29}$$

where I is the PA laser intensity, ϵ_0 is the vacuum polarizability, c is the speed of light, $D_t(R)$ is the transition dipole moment, $\Psi_{\gamma=l,m_l}(E,R)$ is the wave function for an incident partial wave, and $\phi_{v,J}|D_t(R)$ is the wave function for the final excited

state. The overlap of the initial and final state $\langle \phi_{v,J} | D_t(R | \Psi_{\gamma=l,m_l}(E,R) \rangle$ is known as the Frank- Condon factor (Fig. 2.9) [52].

The amplitude of the scattering state wave function increases with probability as one moves away from the potential barrier as R^2 (Fig 2.9). For the bound excited molecular state, the wave function is approximated by a harmonic oscillator deep within the well, but transitions into an anharmonic oscillator as it moves towards the dissociation energy. Thus, for the states near dissociation, the atom spends most of its time near the classical turning point. Thus, the overlap is minimal in the inner regions of the molecular potential. Therefore, atoms are unable to be photoassociated into deep portions of the well. As one moves out in the potential well, the overlap increases and reaches a maximum near the dissociation limit of the bound molecular state, where the photoassociation rate is a maximum. Photoassociation has been used extensively to study these upper levels [38, 22].

After the formation of a long-range molecule in such a state, it decays by two possible methods [22]. First, the molecule can decay via a bound-bound transition to a new vibrational state deeper within the same potential well and release a photon of the energy difference,

$$Rb_2^*(\nu', J') \rightarrow Rb_2(\nu'', J') + h\nu_2. \tag{2.30}$$

The second method is a bound-free transition where the molecule separates to two

free atoms and a photon,

$$Rb_2^*(\nu', J') \rightarrow Rb + Rb + h\nu_3. \tag{2.31}$$

As the transition probability is determined by the wave function overlap, the bound-free transition is the dominant decay mechanism.

One of the most common methods of measuring the photoassociation rate is to measure the number of atoms lost from a trap. Molecules that decay via bound to bound transitions are no longer in resonance with the confining forces of the trap and are lost. The bound to free decay does lead to atoms that can potentially be trapped; however, the decay usually leads to some increase in the kinetic energy of the final atoms, depending on the depth of the potential of their original molecular state. For a deep trap such as a MOT, the added kinetic energy may be small relative to the trapping potential, and the atoms are recaptured. This is especially true for the weaker molecular potentials such as the double well states of the 0_g^- and 1_u. In order to see trap loss due to the weakly bound states, a much shallower trap such as an optical dipole trap or magnetic trap is necessary. In these instances, the bound to free decay leads to a measurable trap loss.

2.4 Feshbach Resonance

The basic physics of a Feshbach resonance has already been extensively covered in other sources [53], [54] [55], but I will cover the necessary physics to understand

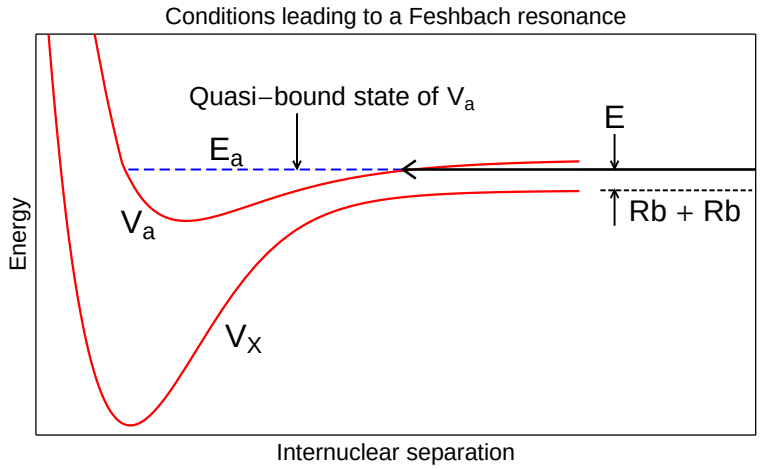

Figure 2.10: Two atoms initially in the separated atoms state collide with relative kinetic energy E. A magnetic field shifts V_x into resonance with V_a, leading to a Feshbach resonance [2].

the work presented in this thesis. We begin by looking at two molecular potential curves (Fig. 2.10), $V_x(R)$ and $V_a(R)$, as described in [53]. The lower potential, $V_x(R)$, is the ground electronic molecular potential or background potential of two incoming atoms. At large R, this potential goes to the separated atoms limit and the atoms maintain their basic atomic structure. This energy is referred to as the open channel. The higher potential, V_a, represents an electronically excited molecular potential that has bound states able to support a molecule, and is commonly referred to as the closed channel.

A Feshbach resonance is observed when the open channel energy is brought near the closed channel, leading to a mixing of the open and the closed channel [53]. This occurs because the bound state is brought near zero energy and the atoms can transition from the free to the bound state temporarily. If the two levels are made

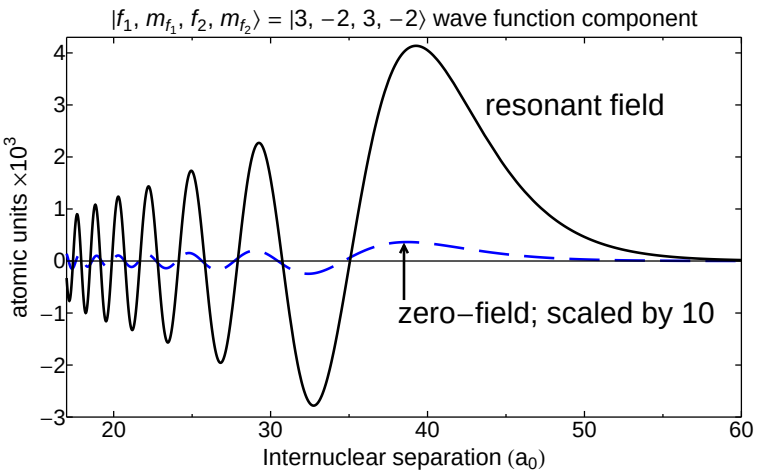

Figure 2.11: The wave function far from a Feshbach resonance and on resonance [2].

degenerate, the elastic cross section and the scattering length become infinite [54]. A major consequence is the modification of the open channel wave function. As seen in Fig. 2.11, the amplitude of the open channel wave function increases and a phase shift is introduced, increasing the probability of the finding the atoms at smaller R.

The energy difference between the open and closed channel can be controlled by either optical or magnetic fields. Here, we focus only on magnetically tunable Feshbach resonances. To magnetically tune a Feshbach resonance, the magnetic moments for each states must be different. If the field is swept through the resonance, the result is a Feshbach molecule in a highly excited vibrational state, near dissociation energy, with a small binding energy compared to the vibrational ground state [53].

The properties of the interaction between atoms at low temperature is deter-

mined by the s-wave scattering with scattering length a [53],

$$a(B) = a_{bg}\left(1 - \frac{\Delta}{B - B_0}\right), \tag{2.32}$$

where a_{bg} is the background scattering length far from the Feshbach resonance, Δ is the width of the Feshbach resonance, and B_0 is the position of the Feshbach resonance when $a \to \infty$. Near the Feshbach resonance where a is large (known as the universal regime), the relevant energy is given by the "dressed" molecular state,

$$E_b = \frac{\hbar^2}{2\mu a^2}, \tag{2.33}$$

where μ is the reduced mass. As described in [53], there are two types of resonances, narrow (width $< 1G$) and broad (width $> 1G$), where a is large and the universal regime is valid. We focus specifically on a broad resonance for this work.

So far, I have described everything as a simple two channel model. However, for the real scenario, multiple channels interact because of the multiple hyperfine states and not including these channels leads to inaccurate physics [54]. I will use the specific Feshbach resonance in ^{85}Rb that this research revolves around to clarify the point. The open channel for the Feshbach resonance at 155 G is the $|F = 2, m_F = -2\rangle + |F = 2, m_F = -2\rangle$ state. The total $m_F = -4$ of the initial

state leads to 4 possible closed channels,

$$|F = 2, m_F = -1\rangle + |F = 3, m_F = -3\rangle,$$

$$|F = 2, m_F = -2\rangle + |F = 3, m_F = -2\rangle,$$

$$|F = 3, m_F = -1\rangle + |F = 3, m_F = -3\rangle,$$

$$|F = 3, m_F = -2\rangle + |F = 3, m_F = -2\rangle.$$

The wave function of the incoming pair must be expanded as the initial incoming channel and the 4 possible closed channels to accurately describe the interaction [54]. Only after including all of these channel into the calculation can the correct results, such as the scattering length, be determined.

As mentioned, we focus specifically on the broad Feshbach resonance in ^{85}Rb for the $|F = 2, m_F = -2\rangle$ state. We do so because the relatively low magnetic field and the large width of the transition make it easier to reach experimentally. This resonance has been extensively studied [56], with most of its properties being well-known to high precision. The relevant parameters are $a_{bg} = -443(3)a_0$, $B_0 =$ 155.041 G, and $\Delta = 10.71$ G.

2.5 Feshbach Optimized Photoassociation

The current methods of spectroscopy for alkali metals include bound-bound spectroscopy and photoassociation. Bound bound spectroscopy [57] measures vibrational states by exciting a gas of molecules at room temperature and measuring

the absorbed frequencies of light. These frequencies are used to measure the molecular energy levels. However, this usually only excites the deeply bound states. Photoassociation, as mentioned, is able to measure states near the dissociation energy because of the significant overlap between the scattering and bound state. However, this technique is limited because of the lack of wave function overlap when moving down in vibrational number. Overall, there are roughly 150 unmeasured energy levels between the two spectroscopic techniques for the 0_g^- state [2]. These levels are important because they define the potential energy curves used by theorists in a variety of experiments. To increase the range at which photoassociation can be used, the wave function overlap must be increased to have a significant photoassociation rate. As seen in the previous section, tuning near a Feshbach resonance drastically increases the average wave function amplitude in all regions for almost all the levels. By combining the two techniques, vibrational levels far below the current limit can be measured, increasing the accuracy of molecular potentials. For an in depth theoretical discussion of Feshbach optimized photoassociation (FOPA), see [2].

Some studies have been performed in the past combining both Feshbach resonances and photoassociation. The first study used an enhancement in the photoassociation rate to determine the position and characteristics of a Feshbach resonance in ^{85}Rb [58]. A study was performed in $^{133}Cs_2$ [59] using a Feshbach resonance to enhance the photoassociation rate deep in the well, as we do for $^{85}Rb_2$. A number

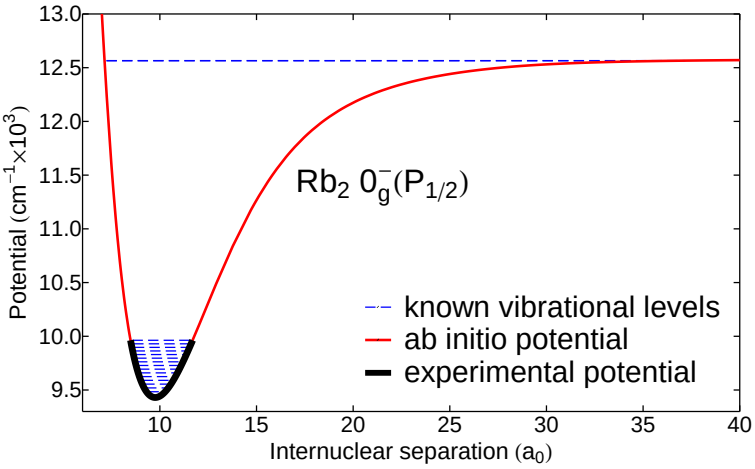

Figure 2.12: The current vibrational levels known for the $^{85}Rb_2$ 0_g^- potential. The known vibrational levels deep in the well are known by bound bound spectroscopy, and the near dissociation states are known from photoassociation studies. Figure taken from [2].

of theoretical studies have been performed studying the enhancement effects and on the creation of ultracold molecules [60], [61] [62], [63]. Most recently, Semczuk *et al*. [4] have used FOPA as part of the process to measure for the first time a series of vibrational levels in $^6Li_2$. The work presented here deviates from these previous publications in that it is done with Rb at a lower vibrational level than previous Rb experiments. We also study effects such as temperature, polarization, and laser linewidth on the FOPA transition.

Chapter 3

Experimental Construction

3.1 Vacuum Chamber

3.1.1 Chamber Design

Our vacuum chamber is a two region system designed for ultra-high vacuum (10^{-10} Torr) (UHV). A diagram of the chamber is shown in Figure 3.1. We use a series of different pumps to reach ultra-high vacuum. The first pump is either a Varian DS 102 mechanical pump or a diaphragm pump, depending on our needs. Each pumps our system to the mTorr regime necessary to start the next pump stage, a turbo pump. The mechanical pump can go lower and does so more quickly than the diaphragm, but it can leak oil into the system, which can be catastrophic. It also requires regular maintenance such as checking the oil. We currently use a diaphragm pump because of its ease of operation. A Varian V250 turbo pump (a differential pump with a turbine spinning at 56k rpm) will reduce the pressure in our system to 10^{-6} Torr before the bake out. This pump must be securely mounted to prevent movement during operation. If not and the turbo pump moves a lot during operation, the consequences can be catastrophic. The next pumps used are two Varian ion pumps, V30 and V60, which pump at speeds

30 L/s and 60 L/s, respectively. These pumps ionize particles, guide them with a magnetic field so that they adhere to a titanium surface inside the pump. These pumps need to be baked out from time to time to remove built-up particulate. After bake-out (which will be covered shortly) the valve to the turbo pump is shut, sealing the chamber, and the mechanical/diaphragm and turbo pumps are removed from the chamber. The ion pumps run continuously to maintain ultra-high vacuum. The final pump is composed of strips of getter material placed within the chamber. When the chamber is baked, the strips are activated and particles are adsorbed by the material. After the chamber cools, the strips become inert, sealing the adsorbed particles and no longer have a pumping effect. The addition of the getting strips reduces the time to reach ultra-high vacuum.

A steel toothpaste-like tube contains a rubidium ampule. The tube is crushed after reaching ultra-high vacuum, releasing rubidium into the chamber. The tube is wrapped with heater tape to increase its temperature, and therefore, the pressure of rubidium in the system. The flow of rubidium into chamber is blocked by a steel ball moved via a magnet. The rate at which the ampule needs to be replaced varies greatly, but we have only replaced the ampule once in four years.

An 18.5 inch by 0.5 inch tube holds a Zeeman slower and sets a pressure differential between the two regions. Ultimately, a Zeeman slower is not used in our experiment, but a pressure differential is maintained. The differential is calculated

by the conductance through a long tube in the molecular flow region [64],

$$C_{long\ tube} = \frac{\pi}{12} v \frac{d^3}{l}, \tag{3.1}$$

where v is the velocity of particles, d is the diameter of the tube, and l the length. For the short apertures on each side of the tube, the conductance is,

$$C_{short\ tube}(m^3/s) = 121 \frac{d^3}{l}. \tag{3.2}$$

The overall conductance adds inversely,

$$1/C_{total} = 1/C_{long\ tube} + 1/C_{short\ tube}. \tag{3.3}$$

Thus, the overall conductance is reduced, leading to a pressure differential.

The next section of the chamber is a rectangular 9.5 inch by 1.5 inch glass cell. The rectangular cell allows for a large degree of optical access compared to traditional ports. However, traditional 2 3/4 inch ports allow for easier alignment using the ports as a guide. Cylindrical cells are used by some, with arguments for and against provided in [65]. Our cell is not anti-reflection coated.

The final piece of the chamber is a 6 port stainless steel cylinder. A 30 L/s ion pump is attached to pumps the second half of the chamber. An ion gauge is attached to determine the pressure of the cell. Finally, two viewports are installed,

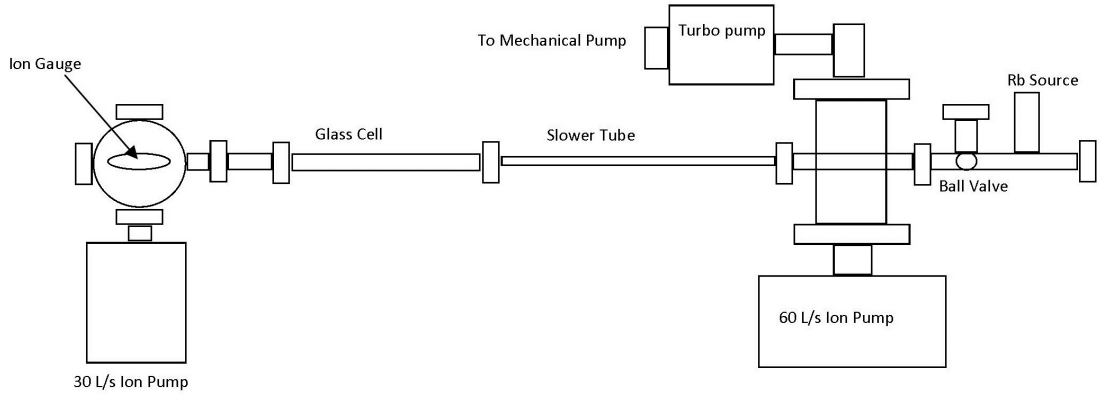

Figure 3.1: The vacuum system used for this experiment. All pieces are labeled except for windows.

with one being used for the Zeeman slower, and the bottom is sealed by a stainless steel plate.

3.1.2 Cleaning Procedure

A clean vacuum system is essential for achieving a UHV system. Any particulates, especially oil based, can outgas for an extended period of time and prevent UHV. In each step of the cleaning process, the vacuum parts and equipment used must always be cleaner than the previous steps. At each step, a new pair of powder free latex gloves are worn. Any equipment that comes into contact with any piece of the vacuum must have undergone the same cleaning procedures as the previous pieces (except for baking), including the tongs used to hold cleaning tissues. An extra amount of time spent on cleanliness at this point will save time in the long term.

The first step is to remove oil from the parts, even if the part is directly from the factory. We start by hand scrubbing all parts in a strong detergent. Next, we submerge the parts in a sonicator with a strong soap that will remove most of the remaining oils. The parts are hung in a crate in the sonicator so they do not come in contact with particulates at the bottom. Not all parts, such as those with lubricants like our right angle valve, can be sonicated. We hand scrub these parts. Next, each part is scrubbed with deionized water, Ultima acetone, and Ultima methanol using clean chemical wipes. As mentioned, this must be done with clean powder free latex gloves. The tongs used are the first pieces cleaned through the entire process, then they are used in the cleaning of the vacuum parts. The parts are rinsed with Ultima acetone and Ultima methanol. The combination of acetone then methanol is meant to remove any organic substance or water, and then remove the residue of the acetone.

The cleaned pieces are placed on aluminum foil. Standard aluminum foil from a grocery store is coated with oil that will contaminate the parts. Oil free aluminum is used for all the pieces beyond this point. All of the solid metal pieces are placed in an oven and baked at 400 ° C for a few hours. No pieces with glass or valves are baked, as the temperature of the oven and the heating rate will destroy the seals. We did not bake or sonicate the vacuum pieces for the first assembly of the chamber, but any part added or future chambers included these steps.

3.1.3 Construction of Chamber

Each piece of the vacuum system is connected by a copper gasket and silvered bolts. All vacuum components are stainless steel. A dissimilar metal must be used for the bolts and gaskets to prevent seizing after baking or while tightening. If steel bolts must be used, it is necessary to lubricate the bolts with an anti-seizing gel. The gel is terrible for vacuum and extreme care must be taken when using it.

A copper gasket is placed between the knife edge of each vacuum part. Viton gaskets are not used as they cannot be baked as high or hold vacuum to as low in pressure as copper gaskets. The knife edge and the copper gasket are cleaned again with Ultima acetone and methanol before assembly. The bolts are inserted and tightened in a star pattern. This pattern ensures a uniform clamping of the copper gasket. Each screw should be tightened roughly the same amount and multiple iterations must be done before the screws are completely tightened and there is no gap between the vacuum parts. The amount of copper seen between the gap should be roughly the same after each stage of tightening. When the gap is small, we use a flashlight and view along the axis of the gap for the shine of the copper. If one side is completely tightened too early, the connection will have to be disassembled, and the copper gasket removed and discarded. A new copper gasket will be used and the gasket and knife edge re-cleaned.

Once the entire vacuum system is assembled, a mechanical or diaphragm pump is used to pump down the system to the mTorr range. A thermocouple between the

turbo pump and mechanical/diaphragm pump monitors the pressure. Once the system is near a mTorr, we turn on the turbo pump. The turbo pump will make loud high frequency sound while coming to full speed. This can be dangerous to one's hearing, and you should minimize the amount of time spent near the turbo pump warming up. The temperature of the turbo pump is monitored during the pumping to prevent overheating. The temperature is indicative of the pressure, and can indicate a leak. After roughly 15 minutes, an ion gauge is turned on and monitors the pressure. There will be an initial increase in the pressure from particulates coming off of the ion gauge. The ion gauge is first degassed to remove any particulates on the filaments that would affect the pressure reading. After 10 minutes, the degass is turned off and the pressure is recorded. The system should be in the 10^{-6} Torr range.

At this point, the vacuum system is checked for leaks. Methanol is sprayed on each joint and the pressure is monitored. If a leak is found, tightening the bolts around that seal may fix the issue. If not, the connection will have to be undone, a new gasket used, and the screws re-tightened. The same construction procedure as before will have to be followed. This step does not guarantee there are no leaks in the system, only that there are no leaks on the order of 10^{-6} Torr.

3.1.4 Bake Out Procedure

The system is baked out at a high temperature (over 200 °C) for a long time (days) to remove any contaminants in the system. This process is done in stages,

and each stage should be done thoroughly or else all stages will be repeated. We followed the procedure from [65] with some variations for our specific system.

The process begins by placing Teflon coated thermocouples at temperature sensitive points on the chamber. This includes any glass to metal junction, the inlet valve for the turbo pump, and the magnets on the ion pumps. These components have lower temperature requirements and glass to metal seals have heat rate requirements. For example, the glass to metal seals typically cannot be heated more than a couple °C per minute or else the seal will be destroyed, and UHV cannot be reached. Because of this, we minimize the number of glass windows on our system. Multiple thermocouples are placed across the chamber to monitor the temperature and uniformity. The glass cell is wrapped with fiberglass cloth to prevent scratching.

The entire system is wrapped in resistive heater tape. This is must be done uniformly across the entire chamber. If not, cold spots can form causing particles to stick to these areas and prevent ultrahigh vacuum. Each heater tape is controlled by a separate variac controller. Different styles of heater tape and different sections require different supply voltages to reach the same temperature. Fiberglass insulation is wrapped around the chamber to prevent heat loss. Standard aluminum foil is wrapped around the fiberglass to secure it. We heated the entire chamber to 250 °C (except for the turbo pump inlet valve which is kept at 120 °C) while continuously running the mechanical and turbo pump. As previously

mentioned, the glass to metal seals limit the heat rate of the chamber. We try to stay below a rise in the temperature of 1.5 °C per minute. This number is set by the manufacturer of the windows.

For our first vacuum system, the magnets for the ion pumps were removed during baking. For subsequent vacuum systems, the ion pump magnets remain on during baking which we suggest for a higher vacuum. The system is heated to a little below 300 °C, limited by the windows and magnets. After baking with only the mechanical and turbo pump for roughly a day, we turn on the ion pumps. This allows for most of the particulates to be removed by the turbo pump, as opposed to the ion pump that has a limited amount of material it can pump. The valve between the ion pump and turbo pump is mostly closed. The mechanical, turbo, and ion pump continues pumping for a few days until the pressure reaches 10^{-9} Torr.

At the end of the bake, the variacs are turned down over the course of hours to allow the system to cool slowly and prevent excess strain. The system should be in the 10^{-10} Torr range after cooling. If so, the valve to the turbo is completely shut and the turbo and mechanical pumps are turned off. You must follow the procedure in the turbo pump manual for turning off these two pumps. If this is done incorrectly while using a mechanical pump, oil will be sent through the turbo pump and into the system. The entire vacuum system will need to be re-cleaned and the turbo pump will need to be sent back to the manufacturer to be cleaned.

After the first pump down of our chamber, we used a diaphragm pump to avoid any trouble involving oil.

If the system pressure increases after closing the valve to the turbo pump, there is most likely a leak in the system. The system must be unwrapped, and methanol is sprayed on all the joints. The pressure is monitored after spraying methanol on each joint to determine the location of the leak. If no leak is found, helium is spayed near each joint, and the pressure is monitored. If a leak still cannot be found, we use a leak detector system that includes a roughing pump, turbo pump, and ion gauge. Once again, tightening the screws around the joint may solve the issue. If not, the joint needs to be dissembled, re-sealed, and the pump down and baking process is repeated.

3.2 Lasers

3.2.1 Low Power Diode Lasers Construction

Our system has used two different generations of external cavity diode lasers for the trapping, re-pump, and probe laser. The main goal is a narrow linewidth laser (less than 1 MHz) that is stable in frequency for hours. These two goals must be met for increased accuracy when measuring atomic transitions and for long periods of data taking. The stability is achieved through mechanical, temperature and current stabilization. An in depth guide to building laser diodes has already been written [66]. I will describe only briefly our specific lasers.

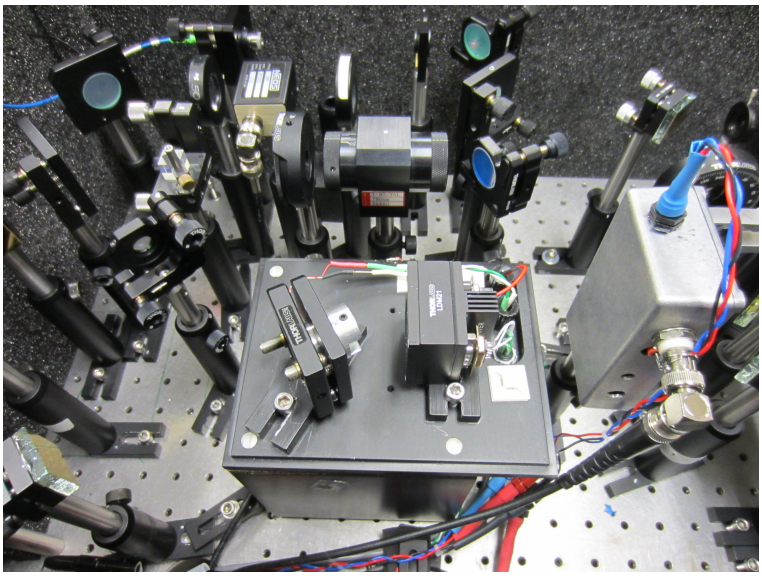

Figure 3.2: The original external cavity diode laser set-up as well as the optics for locking and coupling into a fiber. The laser is placed on a large aluminum block, which is placed on sorbathane pads. This minimizes the mechanical fluctuations coupled to the laser. The diode mount on the right side of plate houses the diode, the optics for collimation, and the electrical connections for cooling the diode and supplying current. The grating is inserted into a Thorlabs mount on the left side of the plate.

The first generation is based on the system presented in [67]. Our design has some differences, and so the system will be discussed. A picture of the assembled laser is shown in Figure 3.2. The base of the laser is a 4 inch x 4 inch x 6 inch anodized aluminum block. The large block reduces the effects of mechanical vibrations, and acts as a heat sink. The block is anodized to prevent current flow and oxidation. It is placed on four 1/2 inch sorbathane pads to reduce the mechanical vibrations coupled to the optical table.

A thermoelectric cooler (TEC) is placed between the large base and a 1/2 inch thick anodized aluminum plate. A platinum transducer (TH100PT) is inserted into

the side of the plate to monitor the temperature with a Wavelength Electronics PTC 2500 temperature controller. The temperature controller is connected to the TEC and maintains the temperature at 1 °C above room temperature.

A Thorlabs LDM21 laser diode mount with a Thorlabs diode (GH0781JA2C) is attached to the plate. The laser diode mount provides connections for the diode current and temperature control as well as a lens for collimation. The connection cables are secured to the plate to minimize vibrations that may travel through the cables that effect the laser diode stability. A Thorlabs LDC500 diode driver powers the diodes, and a Wavelength Electronics PTC 2500 controls the temperature.

The output of the diode strikes a Thorlabs blazed 1200/mm ruled diffraction grating (GR13-1205) specified for 500 nm. The grating is inserted into a machined mount that is secured in a Thorlabs KM100 optic mount. A piezeoelectric transducer (PZT) is placed between the face of the mount and the tilt screw for precision horizontal control. The distance between the grating and diode laser is kept constant by the heated plate. A change in the cavity length will lead to instability in the lasing frequency. The voltage applied to the PZT is controlled by a sidelock servo.

A steel lid is placed over the laser to minimize mechanical/acoustic vibrations and thermal fluctuations. A hole is drilled for the output of the laser and covered with AR coated glass. The entire laser, along with the Dichroic Absorption Vapor Laser Lock (DAVLL) locking system are covered in an isolation box. The box is

a three layered system to minimize acoustic vibrations, effects of airflow and acts as a Faraday cage.

We have an instantaneous linewidth of less than 5 MHz with our laser locked. However, we find the laser is too susceptible to acoustic and mechanical vibrations leading to jumps ($\geq$ 5MHz). Because of this, we switched most of our lasers to a design that is more robust and solidly constructed.

Our most recent design is taken from the Shaffer group. A picture of the design is given in Fig. 3.3. The new design is completely made of aluminum that bolts together and is a much more solid, sturdy design. The larger mass and more solid construction makes the laser less susceptible to mechanical and acoustic vibrations, but lacks the temperature stability of the previous design.

The enclosure of the laser is cut out of a single piece of aluminum. A recessed area is cut into the block and holes are drilled in the back for BNC connections. The enclosure attaches to the same large aluminum block as the old laser diode design. Once again, four 1/2 inch sorbathane pads are attached to the bottom of the block to minimize the effect of vibrations. A TEC is placed between the enclosure and the plate holding the grating and diode. A hole is drilled in the side of the plate for a platinum transducer, and the temperature is controlled by a Wavelength Electronics controller.

A small diode block is attached to the plate to hold the diode as well as the collimating lens block. Thermal paste is placed between the diode mount and plate

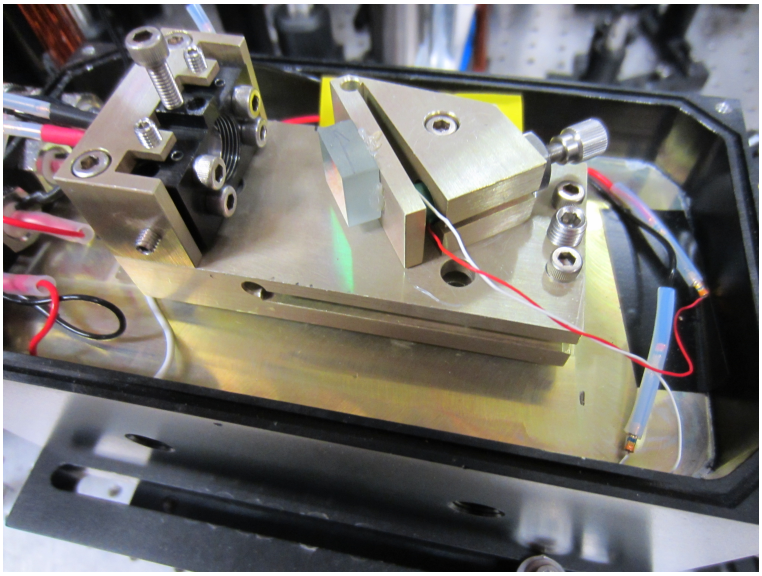

Figure 3.3: The current external cavity diode laser set-up used for most of the lasers in the lab. The enclosure holding the laser mount and grating is screwed into a large aluminum block resting on sorbathane. Between the plate holding the diode and grating, and the enclosure is a TEC. On the side of the plate, a platinum transducer is inserted to measure the temperature of the plate. The diode is inserted into the mount from behind, and the collimating lens is attached to the anodized piece in front of the diode. The grating is glued onto a mount that screws into the plate. A fine-thread screw moves the grating horizontally with respect to the diode. The vertical is adjusted by the three screws at the end of the plate.

to ensure good thermal contact. A 9 mm can diode is inserted through the back of the diode block. The diode is secured by a screw with a hole in the middle for electrical leads. The lens block is attached to the diode block with 4 front plate screws. Two screws on the top and bottom are used to move the lens block up and down, and a screw on each side moves the lens block left and right. The lens is screwed in and out of the block to adjust the distance from the diode.

Collimating the output is slightly different between the two laser diode set-ups, and I will address both of them here. Collimating begins with the orientation of the diode. In the old laser diode set-up, the laser diode mount ensures that the diode laser output is either along the vertical or horizontal axis. However, on the new set-up, the diode must be rotated to the correct orientation. Next, the output is viewed on a large card a few inches away from the diode with an IR viewer. The output will be very large, as there is no collimating lens yet. The center of the out which should be an oval is marked. Any defect in the diode can usually be seen at this point. Dust on the diode will create a circular diffraction pattern in the diode output. If rings are seen, the diode facet should be cleaned.

Next, the collimating lens in inserted. The position of the lens is moved around until the output of the diode is centered on the mark. For the old laser diode set-up, this process can be a bit difficult due to the limitations of the mount. The four screws in the corners of the faceplate are mostly screwed in, but there must be enough slack to adjust the faceplate. The faceplate of the lens mount is moved

by hand, and once the spot overlaps the mark, the screws in the corner are fully secured. There is a fairly small amount of play in the movement, and we sometimes find it necessary to drill the screw holes out a bit more. Then, the diode output is imaged a far distance away as compared to the length of the experiment. The diode lens is rotated to move the position of the lens in or out. The output is focused far away, but will end up being an oval.

The lens mount on the new set-up is slightly more complicated, but it allows for more control. The lens on the new diode mount is moved around via six screws, four for the vertical and two for the horizontal. This allows for a more precise positioning of the lens, but it can also take longer. The output is once again focused at a point a large distance away with respect to the experiment. The lens is screwed in and out to adjust its position with respect to the diode. The lens is then secured by a screw through the top of the mount. As the screw is tightened, the position of the lens may change slightly. This is enough to bring the lens out of focus, and the securing of the screw must be done very gently. After correctly collimating the diode, the four front plate screws are fully tightened.

A ruled diffraction grating is epoxied onto an aluminum mount, which is secured to the plate. Thermal paste is placed between the grating mount and the plate to ensure good thermal contact. A PZT and ultra fine screw are used to push the front of the grating mount, controlling the horizontal alignment of the beam. A space is cut in the center of diode plate for roughly three quarters of the length.

Three screws at the end of the plate are screwed in or out for vertical alignment of the grating with respect to the diode.

After alignment, an aluminum lid is secured over the enclosure. The top and bottom of the lid are in electrical contact, forming a Faraday cage. A hole is cut for the output of the laser and a AR coated window covers the hole to prevent airflow.

3.2.2 Frequency Control and Stabilization

We use three methods to tune and stabilize the frequency of our diode lasers: current, grating, and temperature. The first step is the temperature control of the diode. The electrical connections for the temperature control have already been discussed in the laser diode construction. We set the temperature by adjusting a trim pot on the controller until the desired voltage (which corresponds to the resistance on the platinum transducer for a specific current) is reached. We stablize the temperature by adjusting the maximum current to the TEC and the gain of the controller. We attach aluminum fins on the back of the controller to prevent overheating. Unstable temperature control leads to a steady drift in the frequency. We usually see a few tenths of a GHz per minute drift without any temperature control. The temperature is also used to tune our lasers an up to an additional 5 nm by heating or cooling the diode, changing the length of the diode cavity.

Grating feedback is the next step towards frequency control and stabilization. The position that the output of the diode strikes the grating is extremely important

for stability and tuning of the laser diode. The horizontal position determines the frequency that is feedback into the diode, while the vertical determines the stability. Once again, each laser diode set-up has a slightly different procedure for grating alignment.

The first step for each laser set-up is to align the horizontal beam path. When first aligning the grating, we intentionally misalign the grating so that we can see the 1st order reflected beam on a card. We then adjust the angle of the grating so that the first order is overlapped with the output of the diode. On the each diode set-up, this is done by rotating the entire grating mount. Once close, the mount is secured and the fine threaded screw is used to make small changes to the horizontal position.

Next, the vertical position of the first order reflected beam is adjusted to bring the output over the diode facet. The current is turned down to just above lasing threshold. The vertical is adjusted and the output of the laser is observed until a flash in power is seen. The current is turned down and the vertical adjusted until another flash is seen. This is done iteratively until the current threshold is minimized.

After initial alignment, we adjust the horizontal angle of the grating with respect to the laser with the ultra-fine thread screw. Depending on the diode and grating, we tune the laser no more than 5 nm with the 500 nm grating because of the loss of feedback into the diode. While tuning, the vertical alignment of the

grating must be redone every few hundred GHz to maintain good coupling. We typically use a grating at 500 nm so that less light is in the first order, increasing the light in the zeroth order for the experiment. If we need to pull the diode more than 5 nm with the grating, we typically use a grating specified for 750 nm. The added power in the first order increases the feedback to the laser, allowing us to maintain stronger coupling while further detuned.

Once we are near the desired frequency (within 50 GHz), we begin fine tunning the frequency with the current, PZT, and small changes in temperature. We usually only use the current and the PZT because we can tune the laser roughly 2-3 GHz with the large PZT stacks and current modes are usually around 4 GHz apart. However, every once and awhile the desired frequency is on the edge of a grating or current mode, and we will tweak the temperature slightly to give us the extra movement in frequency.

Once we have reached the desired wavelength, we use a DAVLL to control the PZT and stabilize the frequency of the laser. The general set-up is seen in Figure 3.4. The theory behind the locking system is discussed more in-depth in [68]. In brief, a frequency ramped circularly polarized beam is passed through a Rb vapor cell in a field of roughly 100 G. The magnetic field splits the level degeneracy, changing the amount of light absorbed in the right and left circular polarization as described by Δm= $\pm$1. Each polarization is separated into linear orthogonal components by a $\lambda/4$ wave plate and a polarizing beam splitter cube. The two

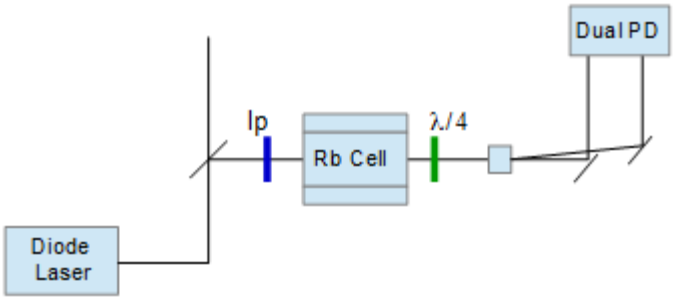

Figure 3.4: The DAVLL set-up used for locking all of our diode lasers. A weak pick off beam is sent through a linear polarizer to ensure there is no polarization fluctuation overtime. The beam travels through a Rb vapor cell in a magnetic field, and through a quarter wave plate. The light is split into separate polarizations by a Glan-Thompson polarizer and each polarization is focused on a photodiode.

signals are sent into separate photodiodes. The two signals are subtracted from one another. As the frequency ramp is reduced, the error signal flattens out and is set to 0 V. We typically compare the DAVLL spectrum to a saturated absorption spectrum to choose the desired frequency. The laser frequency can be tuned small amounts (up to hundreds of MHz) with a bias to the error signal.

3.2.3 Beam Shaping and Control

The output from most diodes is asymmetric and must be reshaped into a more Gaussian profile. Two methods are used depending on the purpose of the beam. For example, the re-pump beam profile is not as important because of the low amount of power needed to pump the atoms. However, the probe beam must match a Gaussian profile because of its use in absorption imaging.

The first step is correcting the beam asymmetry with a prism pair. This optic

expands the beam in only one dimension, correcting some of the asymmetry. The amount of expansion is set by the angle between the prisms. This creates a beam that is close to being circular. This level of symmetry is acceptable for some applications, such as the re-pump and when it is used in the dark spot MOT configuration.

For our probe and trapping laser, we further clean up the profile by passing it through an angle polished polarization maintaining optical fiber. This ensures a constant polarization of the beam and a Gaussian profile. The Gaussian output of the trapping laser leads to a uniform atom distribution in the MOT. We fit our absorption images to a Gaussian profile, so the probe laser must match this profile for accurate modeling.

To align the polarization maintaining fiber, we align the key of the fiber to be parallel or perpendicular to the polarization of the laser. To fine tune the polarization alignment, we place a $\lambda/2$ wave plate before the fiber optic input coupler and a $\lambda/2$ wave plate and polarizing beam splitter (PBS) cube after the fiber. A photodiode measures the output of each beam from the PBS. We set the input polarization, rotate the output, and measure the difference between the two photodiode signals. We rotate the input polarization until the difference is maximized. Another common technique is to strain the fiber while watching the power output of the fiber and rotating the half wave plate. When the effect is minimized, the fiber is correctly aligned. Not aligning the polarization leads

to drifts in the power while running the experiment, which can skew absorption imaging results and change the MOT number over time.

All lasers are controlled with an acousto optic modulator (AOM), a mechanical shutter, or both. The two different methods of shuttering provide different performance. The AOM is an extremely fast shutter (less than 1 μs for a well focused beam) and allows for intensity control. However, a portion of a beam can bleed through the first order, even when no voltage is applied to the AOM. This can be an issue in absorption imaging. The probe laser is used for absorption imaging, and so pulses of a few hundred microseconds are necessary. We use an AOM on the re-pump laser because the intensity must be decreased during the loading of the FORT. Ideally, an AOM would also be on the Ti:S to stabilize the power output in real time and on the trapping laser to reduce the intensity during FORT loading. We do not stabilize the power of the Ti:S, but find that the laser is stable enough to produce a somewhat consistent trap.

A mechanical shutter completely extinguishes the light, but does so much more slowly (on the order of a millisecond). We use mechanical shutters on the Ti:S, trapping and probe lasers. It is very important for each of these to be completely extinguished, and without it, there would be experimental ramifications such as trap loss or unwanted optical pumping.

3.2.4 Tapered Amplifier

We have built our tapered amplifier (TA) with a design provided by the group of Dr. Shaffer. We amplify the trapping beam to increase the number of atoms in the MOT. The diode mount is shown in Figure 3.5. We use a 1 W tapered amplifier chip from M2K. The chip is secured into the mount with a screw, with the back and bottom side flush against the mount. The diode must be in good contact with the mount to ensure good heat exchange and current flow. The diode is actively cooled to prevent overheating. A thermoelectric cooler is placed between the mount and an aluminum base. A platinum transducer is inserted into the side of the mount. The resistance from the platinum transducer is read by a Wavelength Electronics temperature controller that actively cools the mount via the TEC. We keep the diode 1 °C below room temperature.

The general set-up for the trapping laser and TA can be seen in Figure 3.6. To align the TA, the chip is turned on with no seed laser, and an output is seen on each side. We collimate the output from the back of the tapered amplifier. The collimation is done in the same manner as the second generation diode laser design. Next, the trapping beam is mode matched and overlapped with the back beam from the TA. Mode matching the two will focus the trapping beam to the correct dimensions for the chip. At the very least, we make the trapping beam slightly larger than the backwards beam from the TA so the entire beam is focused on the chip. Focusing the beam too hard with too much power can damage the

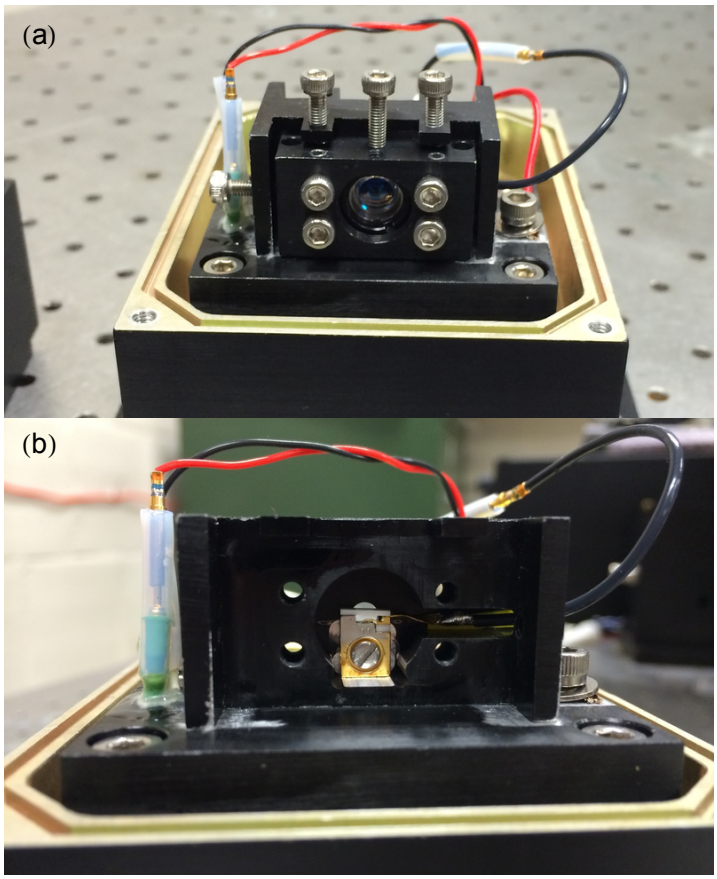

Figure 3.5: (a) The mount used to hold the tapered amplifier and high power diodes with the collimating lens. The two top screws on the outside and the two screws on the side of the mount move the collimating lens block to center the lens on the diode. The top middle screw is used to secure the position of the collimating lens. The four front screws secure the collimating block in place. The current runs through the block through the wire attached on the side and secured with a screw. The thermistor is inserted on the left side of the block. (b) The block without the collimating lens. The return current is sent through a wire connected to the tab of the c-mount.

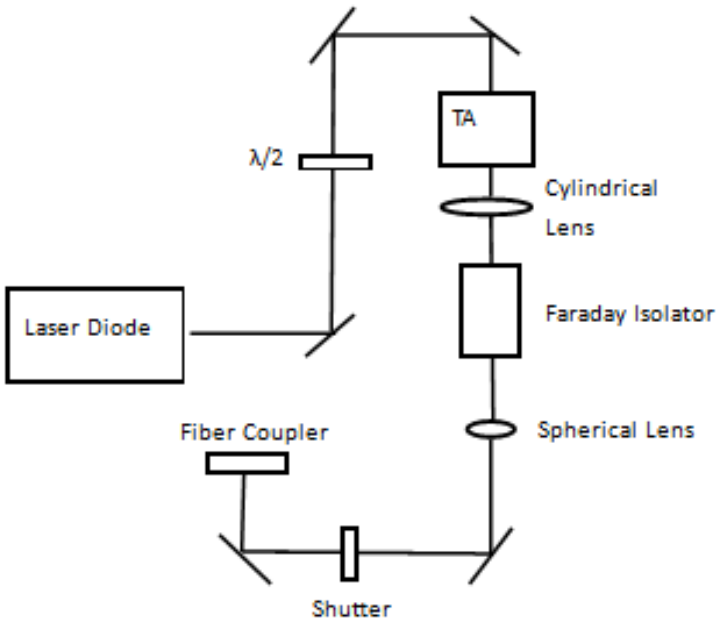

Figure 3.6: The tapered amplifier set-up. The seed laser passes through a $\lambda/2$ wave plate to adjust the input polarization. The output is collimated using a series of cylindrical and spherical lenses. The beam is coupled into a fiber to clean up the profile.

chip. The output of the TA with a seed laser is monitored on a power meter. When the trapping laser is properly aligned, the output of the TA will flash and the power will increase drastically. The power is maximized with the alignment and polarization of the input beam.

Next, the output of the TA is re-shaped to be Gaussian and collimated. The output from these diodes have a large divergence in each dimension. This requires a separate collimation for each axis. First, an aspherical lens (f=3.1 mm) collimates the output in the vertical dimension. Next, we use a cylindrical lens to collimate the horizontal dimension to 1 inch. After collimating, one should expect an output

similar to a square. The output is focused and coupled into a angle polished polarization maintaining fiber with roughly 45% efficiency. The fiber provides a more Gaussian output and better pointing stability.

3.2.5 808 nm diode laser

We have constructed a 4W diode laser at 808 nm for use as a far off resonance trap (FORT). These diodes are inexpensive (less than $100) when compared to the standard lasers used for a FORT. A transversely multi mode c-mount diode is inserted into the same mount as our tapered amplifier. The beam had a node in the middle of output, destroying the Gaussian characteristics. Multiple diodes of the same brand were used, but each had the same characteristic. This can be seen in the focused beam profile (Fig. 3.7). The construction is the same as the tapered amplifier except there is no seed laser. The divergence is larger than the TA, requiring more collimation optics.

The beam was spatially filtered to determine the amount of power in the Gaussian mode. Over a Watt of power was focused into a pinhole with only a few mW output. We do not suggest spatially filtering the beam, and expect a lower output from a fiber. We have experience with other high power c-mount diodes that do exhibit more Gaussian characteristics.

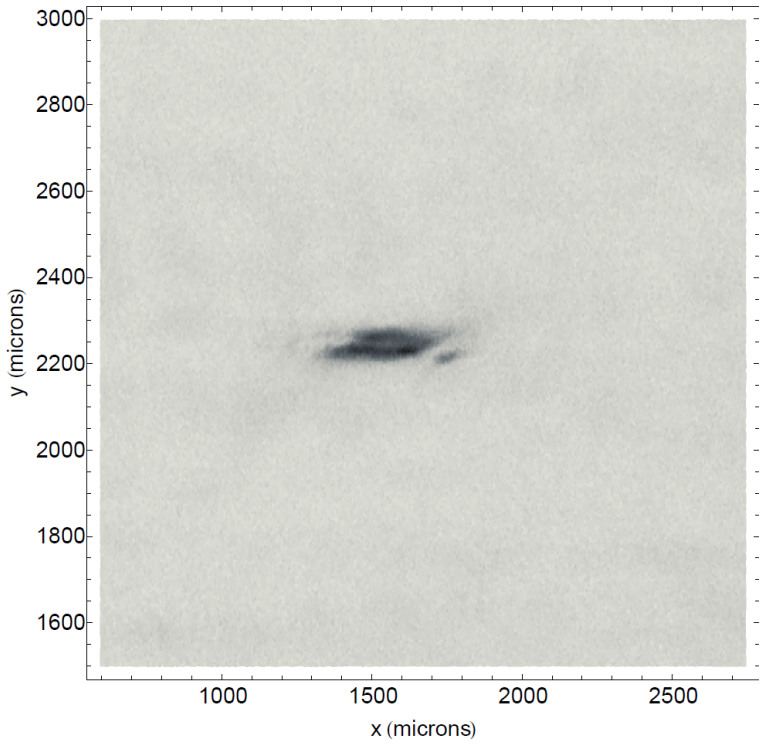

Figure 3.7: The 808 nm laser focused down displaying the two different high intensity regions.

3.3 Magnetic Field Coils

Control of the magnetic field is necessary in three different stages of the experiment. This requires 10 different coils, with ranges in magnetic field strength from a few to hundreds of Gauss. Two anti-Helmholtz coils create the quadrupole magnetic field necessary for the MOT. A general design of our quadrapole magnetic field coil for the MOT is seen in Fig. 3.9. The coils are 46 wraps of 14 gauge copper wire at an average diameter of 16 cm and a separation of 8 cm. The coils fit into the inner edge of our Feshbach coils. This ensures that the zero of the MOT magnetic field is roughly at the center of the Feshbach coils. The design also minimizes the overall space used for coils, as 10 coils around the chamber make beam alignment and the placement of optics difficult. The wire wraps are encased in a plastic shell with no active cooling.

The suggested magnetic field gradient for a Rb MOT is 10 G/cm [43]. We pass 10 A through the coils to achieve this field. The coils are powered by a Sorensen HPD 15-20 power supply with a maximum current of 20 A, allowing for a max gradient of roughly 20 G/cm. The power supply can only be controlled via GPIB. This leads to a large amount of error in the trigger to turn off the magnetic field and takes tens of milliseconds to completely turn off. The magnetic field needs to be turned off quickly and accurately to allow for efficient loading of our optical dipole trap and accurate imaging of our cold atoms. To solve this problem, we built a circuit similar to that in [69]. The circuit uses a high power insulated gate

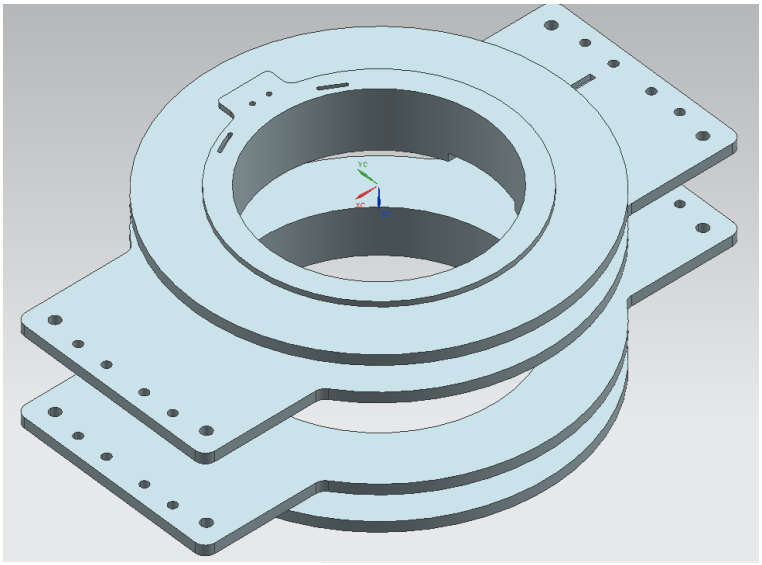

Figure 3.8: A CAD drawing of the coils used to create the MOT magnetic field and the Feshbach resonance. The larger outside coils are used for the Feshbach resonance, while the inner coils are used for the MOT quadrupole field. Overlapping the coils aligns the magnetic field from each coil.

bipolar transistor (IGBT)(International Rectifier IGBT 250 V) to quickly switch off or on the current. The schematic can be seen in Fig. 3.10.

When the IGBT is in conducting mode, the current flows through the coils, creating a magnetic field. The IGBT can be switched to nonconducting mode by a TTL pulse. We use a simple non-inverting amplifier circuit to amplify the TTL pulse from a computer to control the switch. The quick switch time creates a large back emf that slows down how quickly the coils can turn off. To reduce this time, the current is sent to a series of transient voltage suppressor (TVS) diodes (Littelfuse 54 V TVS diode). As explained in [69],when triggered, the diodes

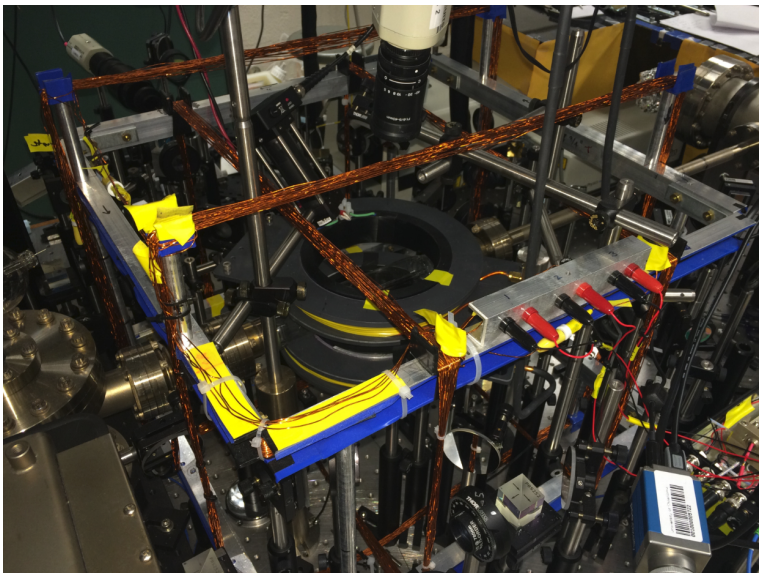

Figure 3.9: A picture of our current set-up showing all the magnetic field coils in use.

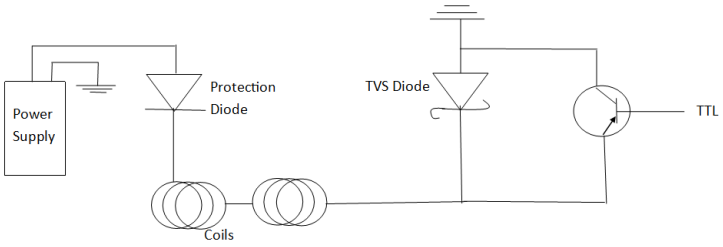

Figure 3.10: The current switch used to turn off or on the current to the MOT coils quickly (less than 30 μs). The current runs from the power supply through protection diodes that prevent back EMF from damaging the supply. The current passes through the magnetic field coils and then through an IGBT. When the IGBT is conducting, the current is able to flow back to the supply. When the IGBT is switched to non-conducting mode, the current is unable to flow. The transient voltage suppressor (TVS) diode prevent back EMF.

conduct and the amount of time to turn off the current is given by,

$$\frac{dI}{dt} = -\frac{V_z}{L}, \tag{3.4}$$

where I is the current, t is the time, V_z is the breakdown voltage of the TVS array and L is the impedance. The fastest switching time is found when V_z is slightly less than the max IGBT voltage. Anything more may damage the IGBT and diodes. Our typical turn off time is 20μs. A set of protection diodes (Vishay Rectifier 1200 V 475 A) protect the power supply from damage while using the switch.

Three pairs of bias coils are used to zero the background magnetic field from the Earth and other constant stray magnetic fields. We cancel these fields to achieve sub-Doppler cooling of the MOT, and therefore, to increase the loading efficiency of our optical dipole trap. Each pair consists of two square 46 cm by 46 cm coils for each dimension. We use larger coils to increase volume of uniform magnetic field. The frame is constructed from U-shaped aluminum coated with electrical tape. Each corner is bolted together and holes are drilled to suspend the frame with 1/2 inch round aluminum posts. Each coil is wrapped 46 times with 20 gauge wire. The current is provided by a Circuitspecialist CSIPPS33T DC power supply with three different power ports and 0.001 A precision. This precision is necessary to cancel the background magnetic field to sub-Gauss level to achieve sub-Doppler cooling.

The final set of coils used in the experiment are the Helmholtz coils necessary

to create the field for the magnetic Feshbach resonance. The coils are made from copper tubing and wrapped around a Phenolic base. Roughly 60 A is needed to produce the Feshbach resonance at 155 G. This leads to significant heating of the coils if they are run continuously for an extended period of time. The coils can be water cooled, but we currently do not because of the short amount of time that the coils experience a current (less than 1 s for every 10 seconds). The average radius of the coils is 11.2 cm, with a separation between the coils of 11.2 cm. The coils are powered by a Walker Scientific HS 52400-4SS power supply. The supply can deliver up to 400 Amps with a stability in 1 part to the 10^7.

We must balance the amount of time that magnetic field is applied for the Feshbach resonance with the amount of time in the FORT. The longer the Feshbach resonance is applied, the larger the effect of Feshbach optimized photoassociation. However, the longer the atoms remain in the FORT, the lower the signal to noise. This is especially true in the early trap times when the density of cold atoms is the greatest. The supply turns on or off the current within 30 milliseconds, totaling 60 milliseconds of the current either ramping up or down. To maximize the amount of time that Feshbach resonance is induced, we have built another high power IGBT switch. The general design of the switch is the same as the one used for the MOT coils; however, this switch is capable of taking up to 220 A. A picture of the switch is shown in Fig. 3.11. Ten protection diodes (Vishay Rectifier diodes 22 A 1000V) in parallel are placed before the switch to prevent damage to the power supply. A

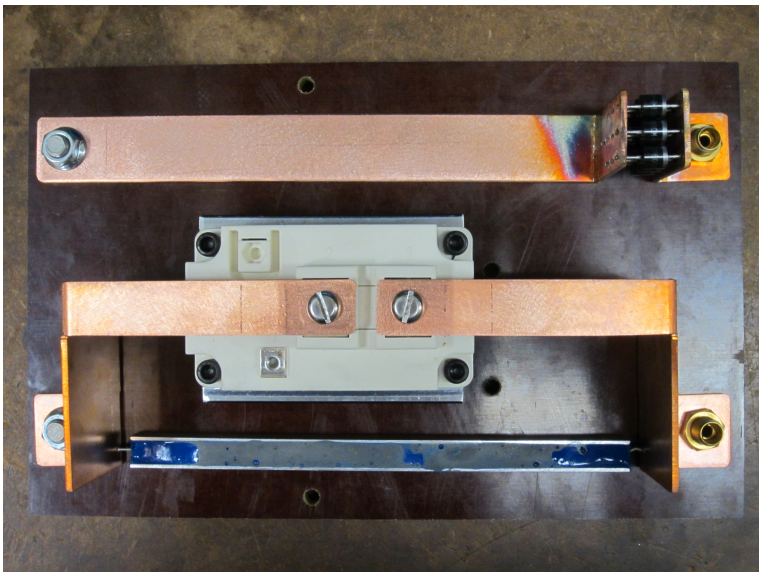

Figure 3.11: The IGBT current switch used for the large current supply. The operation is the same as the switch used for the MOT coils; however, the switch can take up to 200 A.

Infineon Technologies 600 A 1200 V IGBT is used as the switch. Ten TVS diodes (Vishay 5000 W 70 V) are placed in series to dissipate the current when the IGBT is switched to non-conducting mode. With the switch, the turn on/off time are now 20 ms/0.1 ms, respectively.

3.4 Magneto-Optical Trap

Our first generation magneto-optical trap (MOT) comprised of retro-reflecting 3 beams as seen in Fig. 3.12. The average MOT number was on the order of 10^8 atoms with peak density of 10^9 atoms/cm^3 and the temperature in the mK range. We split the beams using a $\lambda/2$ wave plate and polarizing beam splitter cube so the power in the 3 beams are equivalent and linearly polarized. The beams pass

through a $\lambda/4$ before the glass cell so that all beams are circularly polarized. After the cell, the beams pass through another $\lambda/4$ twice, reversing the polarization by π so they have the opposite polarization as the counter-propagating beam. Unfortunately, a trap with atoms in the mK regime is too hot to load an optical dipole trap due to its shallow trap depth (hundreds of μK to a few mK). To have a lower temperature MOT, we must cool below the Doppler limit [43]. This is done by zeroing the magnetic field and having equal power in all six beams. We are able to zero the magnetic field with 3 sets of Helmholtz coils, one in each axis. However, we could not create equal intensity in each of the six beams. The glass cell used is not anti-reflection coated (a chemical film deposited on the surface of the glass), and we lose 4% of the light off of each surface as compared to anti-reflection coated glass which reduces the reflection to roughly 0.5%. Including the light lost from the retro-reflecting mirror and quarter wave plate, we lost roughly 20% of the power in each beam. This placed a limit on the temperature of the MOT, preventing us from efficiently loading a dipole trap.

In the second generation MOT, we split a single beam into six so that no beams are retro-reflected (Figure 3.13). This allows for more control over the power in each beam, allowing for a much colder temperatures. However, the alignment is much more difficult and so it will be discussed here.

First, we equalize the power in each beam right before sending them through the glass cell. This is done by changing the angle of the half wave plate before each

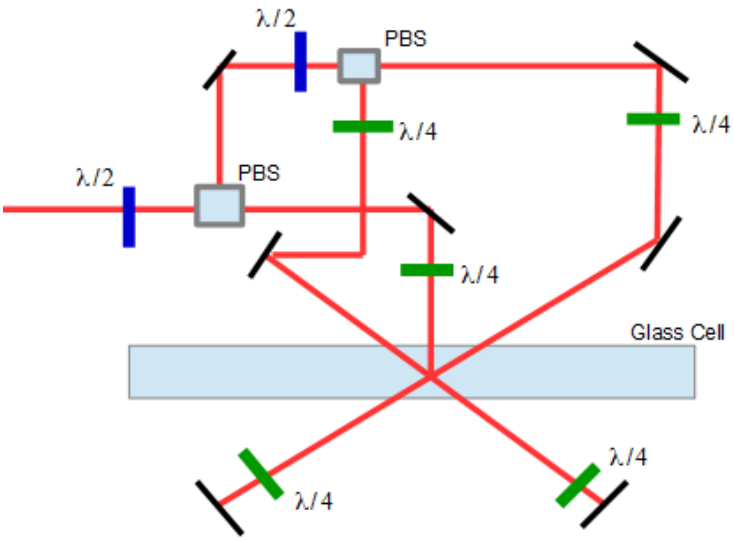

Figure 3.12: The old magneto optical trap (MOT) set-up. We retro-reflect 3 beams to create the 6 necessary for a MOT.

polarizing beam splitter cube iteratively, until all the powers are roughly equivalent (about 5%) just before the glass cell. The power will need to be adjusted in the future, but this will be sufficient to create a MOT.

We then use a tool to assist in aligning the MOT beams. It consists of two perpendicular steel rods with an iris hanging down on each arm. The tool is secured to the MOT coils and the trapping beam is irised down slightly. We align each horizontal beam through its closest and furthest iris, where the iris is slightly larger than the beams. We iris the beam down more and repeat the process until the irises are almost completely closed. A hole in the center of the alignment tool and a long narrow tube are used to align the lower MOT beam. Afterwards, the entire tool is removed and the upper vertical beam is overlapped with the lower. Next, we

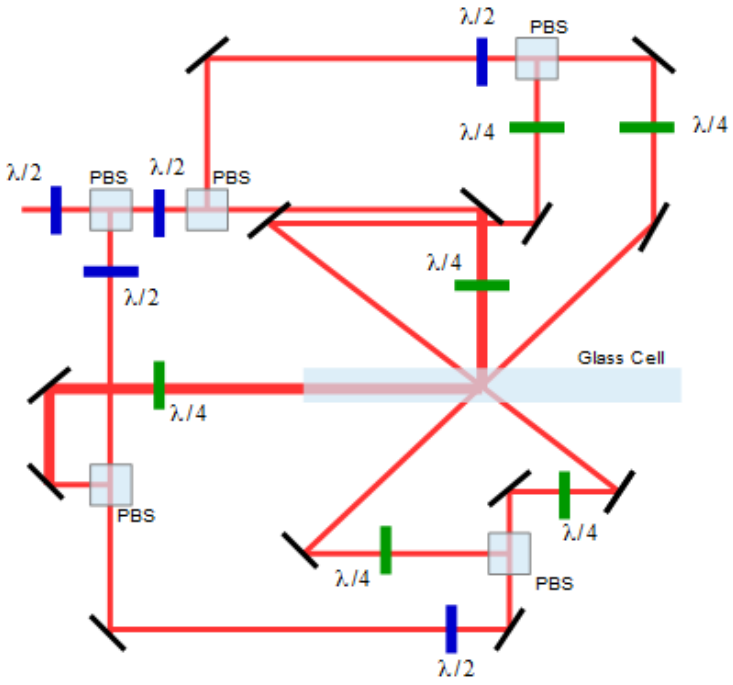

Figure 3.13: The set-up currently used magneto-optical trap (MOT). We no longer retro-reflect beams because of the loss in power after passing through the uncoated glass cell. The thicker red beam indicates the beams that travel in the vertical dimension.

overlap the re-pump with the trapping beams. The MOT iris is completely opened and we turn on the anti-Helmholtz coils. At this point, all counter-propagating beams should be orthogonal and overlapped at the center.

After creating a MOT, the atom number and symmetry are maximized following [65]. We iris down the MOT beams and maximize the number and roundness. We open the iris a bit and repeat this process until the iris is completely opened and the number is maximized. These adjustments should be small, assuming the field is zeroed well and the beams are overlapped with the zero point of the quadrupole field. Next, we pass a large current through the quadrupole coils that reduces the size of the MOT and places it at the zero. The magnetic field is turned down and the MOT cloud becomes diffuse. The cloud will drift away from the zero field position in the direction of the more intense trapping beams. We adjust the half wave plates to move the MOT into the center of the zero magnetic field position. We turn the coils back up to a reasonable field and turn off the current quickly. The MOT should dissipate somewhat slowly and uniformly, indicating sub-Doppler cooling. This process of turning the magnetic field up, then down, and readjusting the half wave plates is repeated until the cloud dissipates slowly and uniformly. At some point, it may be necessary to realign some of the beams, but it should be very small changes. With the new set-up, the temperature of the MOT is roughly 25 μKelvin. This temperature is sufficient for loading an optical dipole trap.

3.5 Computer Control

We use a NI PCIe-6323 board connected to two NI SCB-68 controllers to control all the devices on the experiment. The boards combined have a total of 32 analog inputs, 4 analog outputs from -10 V to 10 V, and 48 digital I/O lines. We control the mechanical shutters, current switches, and cameras with TTL pulses. The AOMs, sidelock servo bias voltage, and large current supply for the Feshbach coils are controlled via the analog ports.

In early phases of the experiment, we controlled multiple devices through GPIB commands. However, GPIB controlled devices do not have the level of accuracy that is needed for our experiments. We find the time uncertainty of GPIB controlled devices on the order of a few milliseconds and so we switched to all TTL or analog devices. We control all of the ports via a LabView program created for each different imaging sequence. The Labview code/boards allow for accuracy on the order of a μs if you write your own clock sequence. For higher accuracy, we would need to switch to a field programmable gate array, making the sequence independent of the computer clock and processes.

3.6 Loading an Optical Dipole Trap

3.6.1 Alignment

Our main FORT is loaded from our MOT by focusing down our Ti:S laser. As seen from Eq. 2.16, the potential is dependent upon the intensity, which in turn

is dependent on the beam waist by

$$I = \frac{2P}{\pi\omega_0^2}, \tag{3.5}$$

where P is the power, and ω_0 is the beam waist ($1/e^2$ radius). The deeper the potential, the larger the fraction of atoms that can be trapped within the FORT from the MOT. As observed in [50], a FORT with a larger waist loads more efficiently, but has a reduced density. Due to spatial limitations, we focus our FORT beam with a 70 cm archromatic doublet from Thorlabs. The achromatic doublet is used to focus all the light to the same position, which is not guaranteed with a spherical lens. The waist of the trap is controlled by the size of the beam prior to the lens, as given by [49],

$$\omega_0' = \frac{\lambda f}{\pi\omega_0}, \tag{3.6}$$

where λ is the wavelength, and f is the focus of the lens. The Rayleigh range describes the length of the focus, given by

$$z_R = \frac{\pi\omega_0^2}{\lambda}. \tag{3.7}$$

When aligning a FORT, both the waist and the Rayleigh range are taken into consideration. It is easier to initially align a FORT with a longer Rayleigh range because it is easier to overlap with the MOT. However, a longer Rayleigh range means a larger waist, which places density limitations on the FORT.

Aligning the FORT with a Ti:S laser is relatively simple because the laser can be tuned to a resonance and the effects on the MOT can be observed. A general schematic of our set-up is shown in Figure 3.14. We begin by expanding the beam to a waist of roughly 1 cm. We linearly polarize the beam with a polarizing beam splitter cube and control the polarization with the half wave plate. We place a shutter near the focus of the beam expander to minimize the turn-off time, but far enough away that we do not melt the shutter. The beam passes through a 70 cm lens to focus the beam near the center of the MOT. We tune the Ti:S to the D2 transition and direct the beam to blow away part of the MOT. At this point, we know we are at least in near the correct placement, except for the point of the focus.

To course align the focus, we place a mirror between the lens and the MOT to re-direct the Ti:S beam. We measure the distance from the MOT to the front surface of the mirror. We place a card this distance from the front surface of the mirror and focus the FORT beam at this point. The position of the focus should be near the center of the MOT. With all of the axes roughly aligned, we pass the focused Ti:S beam through the MOT creating a hole. The beam is aligned to the center of the MOT by viewing the position of the hole with the CCD camera. Now, the Ti:S should be aligned well enough to load a FORT, but still needs to be optimized.

We have also used a high power 808 nm diode laser to create a FORT. However,

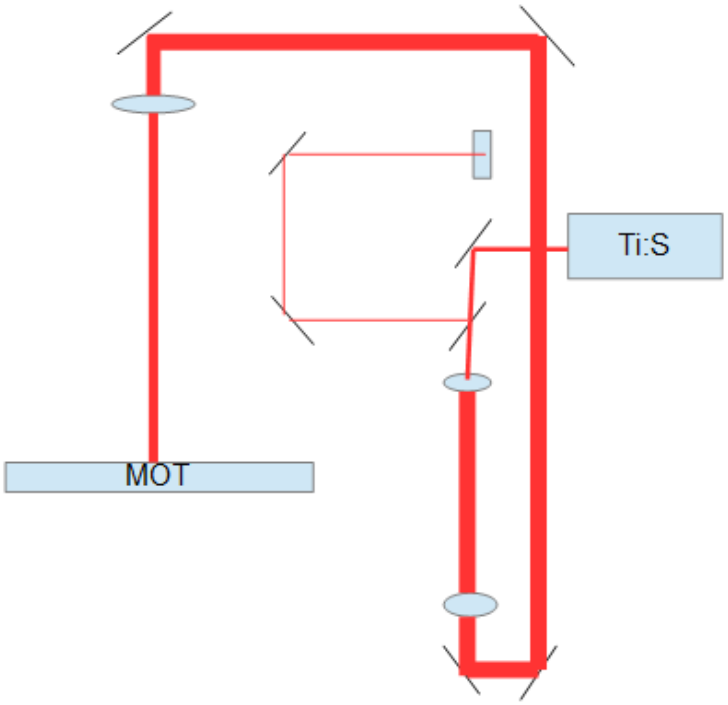

Figure 3.14: The general set-up for our FORT. We begin by picking off part of the beam for wavelength and power measurements. The beam is then expanded and refocused down with a 20 cm achromatic doublet to form the FORT potential.

the alignment is more difficult as we cannot tune the wavelength to a rubidium transition. To overcome this, we overlap the 808 nm laser with a collimated probe beam on resonance with the $4S_{1/2}\, F = 3 \rightarrow 4P_{3/2}\, F = 4$ transition. We pass each beam through a polarizing beam splitter cube and overlap the beams both close and far away. Overlapping the beams allows us to determine the position of the FORT by observing the effects of the probe beam on the MOT. We then follow the same procedure for alignment as the Ti:S.

Our FORT loading sequence was derived from [50], and will discuss it briefly (Figure 3.15). We begin by loading our MOT with an average temperature in the tens of μK. The temperature must be below the Doppler limit to efficiently load the FORT. We find that a molasses indicates a trap cold enough for creating a FORT. After 5 seconds, we detune the trapping laser by roughly 120 MHz to the red, reduce the re-pump laser intensity to 0.5 μW/cm^2, and open the Ti:S shutter. We typically load for the ODT for 100 ms. The trapping and re-pump lasers are turned off in under 2 msec. The trapping light is turned off 1 ms after the re-pump to populate only the lower hyperfine state. This reduces the amount of atoms lost in the FORT due to hyperfine changing collisions. The magnetic field is turned off in under 30 μs. We hold the atoms in the FORT for a least 70 msec before imaging to ensure that all the MOT atoms have left the region.

We use fluorescence imagining for initial alignment of the focused Gaussian beam. After loading and releasing the FORT, the re-pump and trapping light are

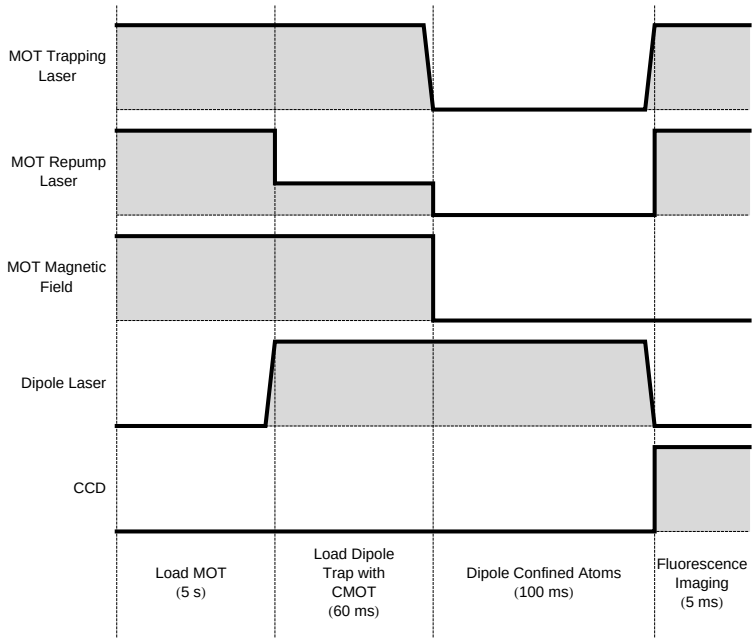

Figure 3.15: The timing sequence used for loading our FORT. We being with both the trapping and re-pump, as well as the magnetic field on for 5 seconds to load the MOT. The Ti:S shutter is opened, the trapping laser is detuned and the intensity of the re-pump is decreased. The FORT is loaded for 60-80 ms. The trapping and re-pump laser, and the magnetic field are turned off and the atoms are held in the FORT for at least 100 ms. The Ti:S shutter is closed and the MOT lasers are flashed on the CCD camera collects the photons emitted by the fluorescing atoms.

turned on simultaneously. The atoms fluoresce, which is imaged by a PCO Tech pixelfly *qe* CCD camera via an adjustable focus lens. A fluorescence image of our 808 nm FORT is shown in Figure 3.21. Once we see an optical dipole trap, we use absorption imaging to optimize the various parameters. We optimize the atom number by adjusting the position of the focus, the intensity of the re-pump, the detuning of the trapping laser, and the loading time. A graph of the optimization of the final three is shown in Figs. 3.16, 3.17, and 3.18. We also optimize the polarization of the light, as seen in Fig. 3.19, and investigate how long the atoms can be left in the FORT while still having a strong signal to noise (Fig. 3.20). We currently do not have a theory on the oscillatory nature of the polarization optimization figure. As there is no magnetic field while the atoms are held in the FORT, the orientation axis is set by the laser field. This may lead to different background two body loss rates due to the polarization of the laser field. The polarization may also affect the loading of the dipole trap. As seen in previous FORT studies, the ellipticity drastically affects the number of atoms loaded into the trap. We may be seeing this effect with the introduction of the half wave plate, but we are currently uncertain on the exact cause. This subject is still under further investigation.

3.7 Imaging

We use fluorescence and absorption imaging in our experiments to image cold atom clouds. Fluorescence is used to monitor the atom number and for quick

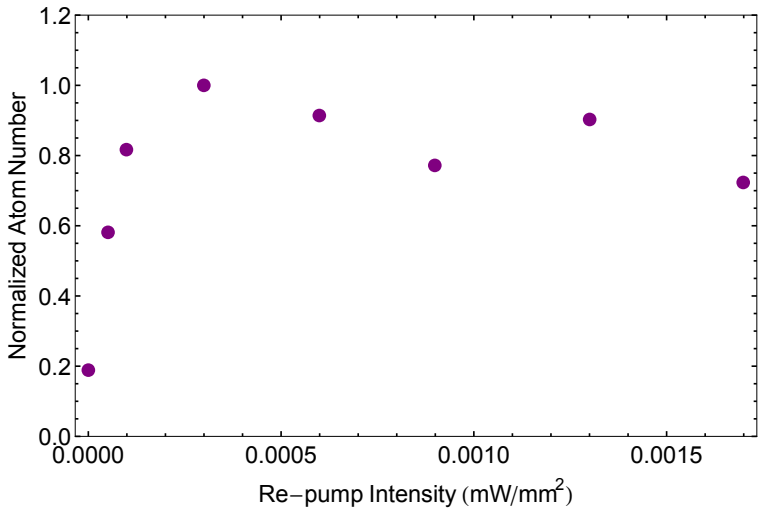

Figure 3.16: The effect the re-pump power during the loading stage on the number of atoms loaded into the FORT. The signal peaks between 3 and 5 μW/cm^2.

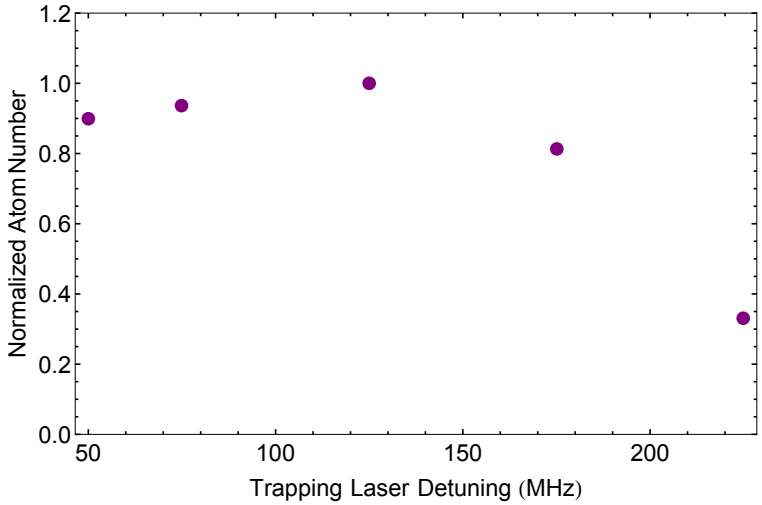

Figure 3.17: The effect the trapping laser detuning during the loading stage on the number of atoms loaded into the FORT. The number of atoms loaded peaks near 120 MHz.

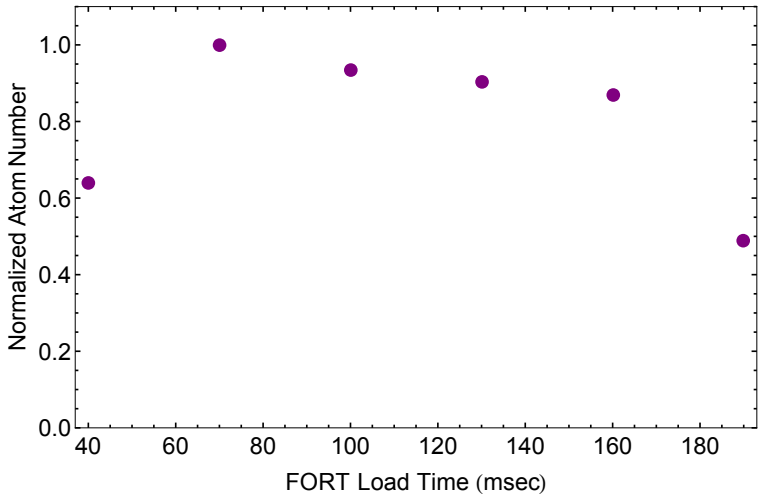

Figure 3.18: The effect of the duration of the FORT loading stage on the number of atoms loaded into the FORT. The atom number peaks at 80 msec.

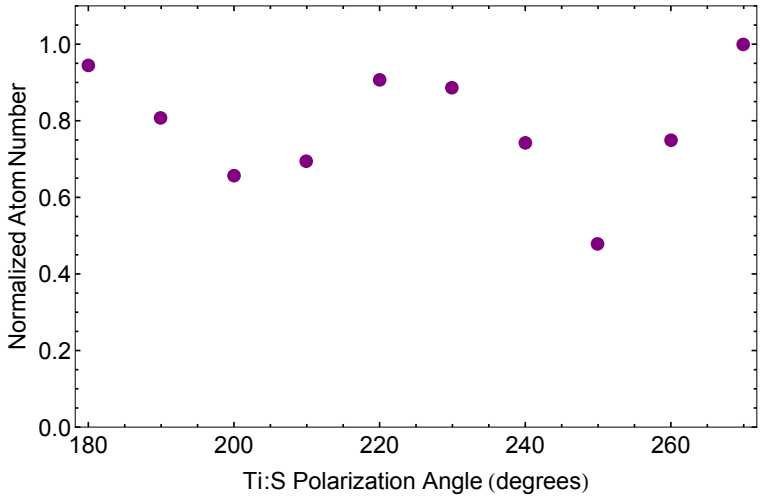

Figure 3.19: The effect of the polarization angle of the Ti:S on the number of atoms loaded into the FORT. The signal cycles to a maximum every 45 degrees

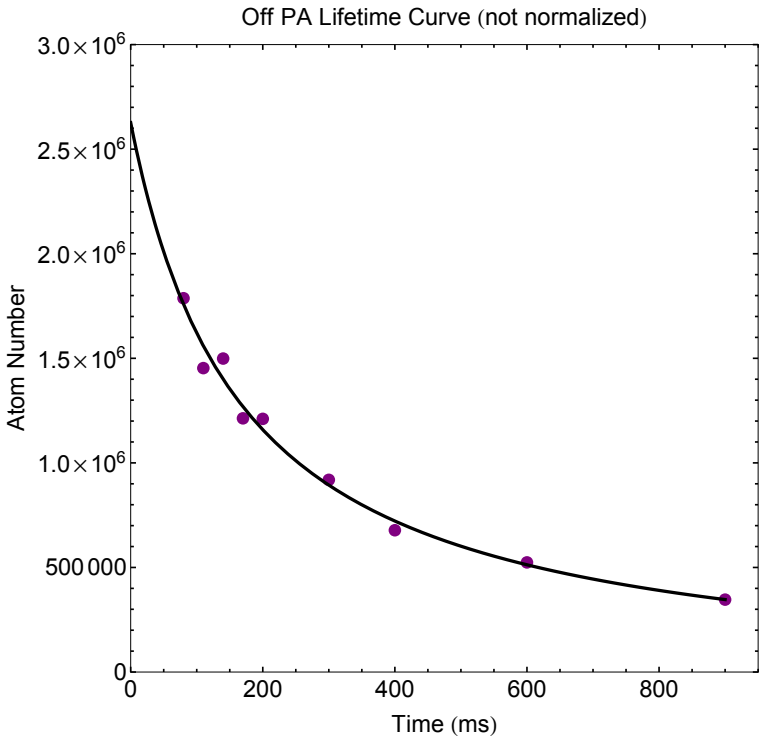

Figure 3.20: A typical lifetime curve for the FORT.

measurements. Absorption imaging is more difficult to set-up, but it yields a more accurate atom number and directly provides the density. In our experiments, we mainly use fluorescence imaging for the initial alignment of the MOT or FORT and initial optimization. We use absorption imaging when we need an accurate and reliable number on the atom number and density, and for the major results in this thesis.

3.7.1 Fluorescence Imaging

A photodiode and lens assembly provide reliable everyday measurements and allow optimization of our MOT numbers. We use a Thorlabs DET20C photodiode due to its large active region (3.14 mm^2), making alignment simpler, but increasing the background noise. We use a narrow band neutral density filter to minimize the background light when necessary. We typically connect the photodiode to an oscilloscope with 1 $M\Omega$ resistance to increase the signal. When taking fast measurements we change the resistance to 50 Ω and amplify the signal. The photodiode is attached at the end of a cage system with a 5 cm lens at the front. The distance between the photodiode and the lens is equal to the distance between the lens and MOT and is 10 cm. To initially align the photodiode, we place the cage system at roughly the correct distance from the MOT and change the orientation of the cage until a signal is shown on the oscilloscope. Our glass cell is not AR coated, and so initial signal can be due to a reflection of a laser beam instead of the fluorescing atoms. To check, we tap the table while viewing the output of the

photodiode. If the signal drops, the photodiode is imaging the MOT. If the signal does not, a reflection is being imaged.

The atom number in the MOT can be determined by considering the geometry of the imaging system and a conversion of the output of the photodiode. The general method followed is from [65]. The number of atoms from the fluorescence signal is

$$N = \frac{4\pi V}{(R)(Solid\ Angle)(Responsivity)(h\nu)(SR)(0.96)^k}, \tag{3.8}$$

where V is the voltage, R is the resistance of the load (usually 1 MΩ), ν is the frequency of the emitted photon, SR is the photon scattering rate and k is the number of uncoated surfaces that the light passes through before the detector. The fraction of light collected by the lens, known as the solid angle, is given by

$$Solid\ Angle = \frac{\pi r^2}{4\pi d^2}, \tag{3.9}$$

where r is the radius of the lens and d is the distance from the lens to the MOT. The responsivity is dependent on the photodiode and is provided by the manufacturer. For our photodiode, this is 0.55 at 780 nm. The photon scattering rate is given as

$$SR = \frac{s\pi\Gamma}{1 + s + 4(\delta/\Gamma)^2}, \tag{3.10}$$

where s is the saturation parameter $\frac{I}{I_s}$, where I is the intensity of the light, I_s is the saturation intensity for isotropic light, δ is the detuning, and Γ is the linewidth

of the D2 transition. For Rb 85, the saturation intensity is 3.895 mW/cm^2 and the linewidth is 6.01 MHz.

We also view the fluorescence of the MOT using two Supercircuits PC-23C security cameras fed to TV screens. Each lens has an adjustable focus to image the MOT. We view the MOT from the top and the side. We do not use the output for any quantitative analysis, but we do use it for optimization of the MOT and FORT.

Our final fluorescence detection technique flashes the cold atoms, either MOT or FORT, with both trapping and re-pump light some time after the trap has been turned off. This excites the cold atoms in the region, which then decay and emit a photon. The fluorescence is imaged on a PCO Tech Pixelfly qe CCD camera with a Navitar Zoom 7000 lens. The camera (which is also used for our absorption measurements) is a 1392 by 1040 pixels CCD with a pixel size of 6.45 μm by 6.45 μm and designed for sensitivity in the near IR. The lens used is pre-assembled and adjusted to focus on the MOT/FORT region. The camera is controlled by an interface provided by PCO Tech through USB and triggered by a TTL pulse. The interface displays the output of the camera, controls the type of trigger (TTL or manual), the rate at which pictures are taken, the exposure time, the binning, and the image size. The minimum time between two images is 5 μs. After imaging the atom cloud, we image the background when no atoms are present, but with the trapping and re-pump beam on. The images are imported into *Mathematica* and

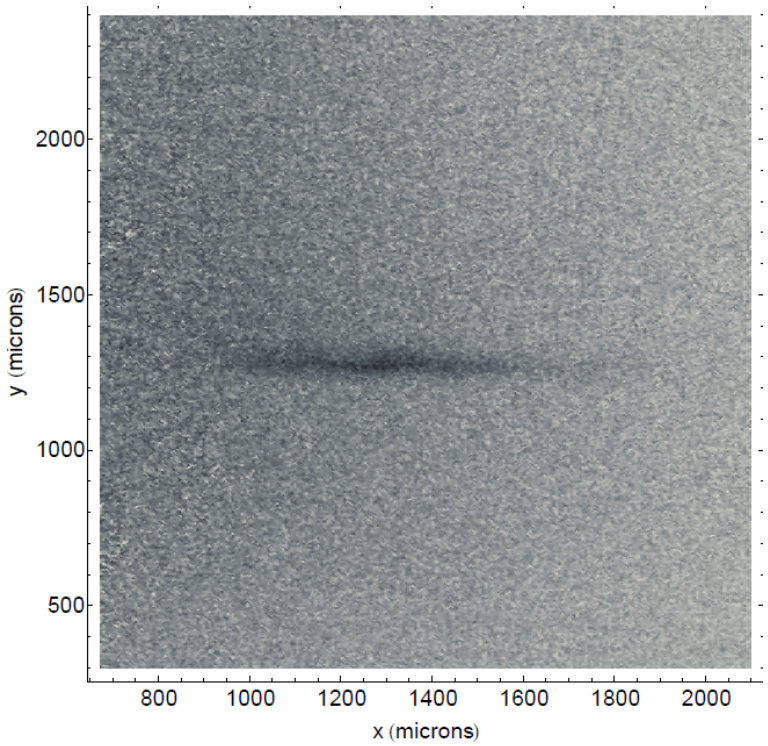

Figure 3.21: A fluorescence image of the FORT created by our 808 nm high power laser and magnified by approximately 11. The image is given in false contrast.

subtracted. We fit the cloud to a Gaussian,

$$f(a, x, \eta, u, \Psi, b) = aexp(-((x - x_0)^2/(2\eta^2) + (y - y_0)^2/(2\Psi^2))) + b, \qquad (3.11)$$

where a is the amplitude, x_0 is the center of the cloud in the x, y_0 is the center of the cloud in the y, η and Ψ are the standard deviation in each dimension, and b is the offset. Multiplying η and Ψ by 2.33 provides the FWHM of the cloud in each dimension. We extract the waist of the cloud in each dimension and integrate the real image over three times this region to determine the arbitrary signal of the cloud. We use this number to optimize the FORT number in our initial alignment.

The magnification of the atom cloud due to the lens is determined by two different methods. For a quick determination, we place a mirror between the camera and the cloud and place a ruler at the focus of the lens. By counting the number of pixels in 1 mm, we determine the magnification. To more precisely determine the magnification, we take images of the MOT or FORT at various times after the trap is turned off. The rate at which the center of the cloud falls is modeled by kinematic equations as,

$$s(t) = s_0 + \frac{1}{2}g't^2, \tag{3.12}$$

where t is the time, g' is the magnified gravity constant, and s_0 is the initial position. We determine the center of the cloud from our Gaussian fit. By comparing g' to the actual value of g, we determine the magnification.

Next, we determine the temperature of either the MOT or the FORT from a time of flight (TOF) measurement. By taking multiple measurements at different times after turning off the trapping potential, we are able to measure the expansion of the cloud in the radial dimension. We assume a ballistic expansion in each dimension,

$$r = (r_0^2 + \frac{k_b T}{m}t^2)^{\frac{1}{2}}, \tag{3.13}$$

where r_0 is the initial radius at $t = 0$, k_b is the Boltzman constant, T is the temperature, and m the mass of Rubidium. This measurement is not as accurate

as those taken with absorption imaging because of the outward pressure created by the trapping and re-pump beam, but should yield results of the correct order of magnitude.

3.7.2 Absorption Imaging

Our more commonly used method in data taking is absorption imaging. This method provides more accurate atom numbers and cloud size than fluorescence, while providing direct information on the density. The set-up for this technique differs when imaging a MOT cloud versus a FORT, but the general theory remains the same. When a beam passes through the cloud of atoms, the intensity is reduced. The intensity is given by Beer's law as

$$I = I_0 e^{-OD}, \tag{3.14}$$

where I_0 is the initial intensity before the medium, and OD is the optical density. Solving for the optical density,

$$OD = ln\left(\frac{I_0}{I}\right). \tag{3.15}$$

We take three images, the image of the probe laser I_0, the image with the cloud I, and a picture with both the probe and the atomic cloud off I_{Dark}. The optical

density becomes

$$OD = ln\left(\frac{I_0 - I_{Dark}}{I - I_{Dark}}\right). \tag{3.16}$$

Next, we scan all of the pixels in the image for any outliers. We move through the data set and average 9 pixels, a center pixel, its neighbors, and its nearest neighbors. There can be outliers due to noise or readout error, as mentioned in [65]. We remove those pixels by comparing pixels to their neighbors, and if they are outside 4 standard deviations of the average, the pixel is replaced with the average. We then bin the data, reducing it by a factor of 9. Without binning, the data set is too large to handle and the computation time is too long. Next, the averaged pixel information is converted into a position by considering the pixel size, and if necessary, the magnification. Next, we fit the optical density to a Gaussian distribution as done in the fluorescence imaging section. From the fitting parameters, we determine the full width at half the maximum distance in each dimension, the atom number (N) and the peak density,

$$N = \frac{a2\pi\eta\Psi}{\sigma_0}, \tag{3.17}$$

$$\text{Peak Density} = \frac{N}{(2\pi)^{3/2}\Psi^2\eta^2}. \tag{3.18}$$

An example of an absorption image of the MOT is shown in Figure 3.22.

The experimental set-up for both the MOT absorption and the FORT absorption are shown in Figure 3.25. In each instance, the sequence begins by flashing

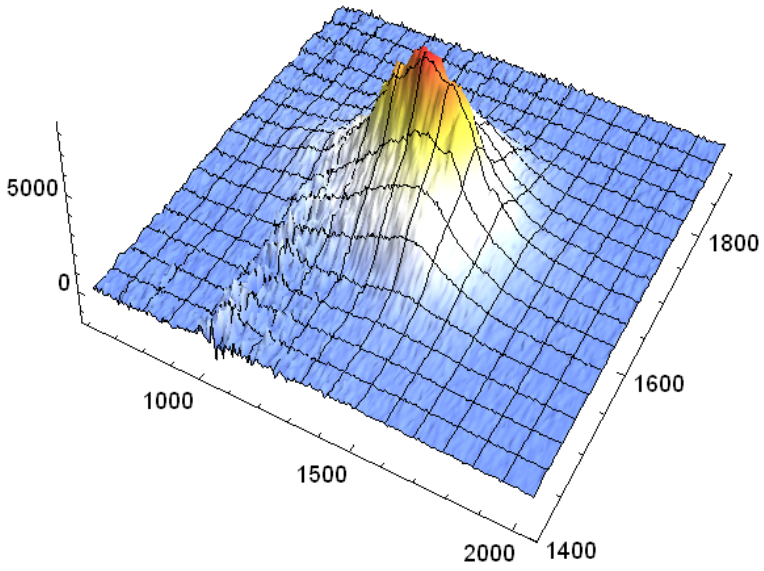

Figure 3.22: The absorption image of our FORT imported into *Mathematica*. The vertical axis is arbitrary signal, while the x and y are in microns.

the re-pump beam to drive the population to the $F = 3$ state. Next, a collimated Gaussian probe laser tuned to the $4S_{1/2}\ F = 3 \rightarrow 4P_{3/2}\ F = 4$ transition passes through the region containing the atom cloud. The beam is circularly polarized, driving the cycling transition to increase the signal to noise, and weak enough that the detector is not saturated. As the probe passes through the atom cloud, a shadow is left in its place. In the case of the MOT, the distortion is large enough that it can be seen by passing the beam directly onto a CCD camera. The FORT has additional optics because of its small size leading to the diffraction of the probe beam around the cloud. For this, we use two achromatic lenses (150 mm and 250 mm) to magnify the image of the shadow. The first lens is placed a focal length away from the cloud, while the second lens is placed its focal length away from the CCD. We determine the magnification using the gravity method as described in fluorescence imaging, as well as the temperature of the MOT and the ODT.

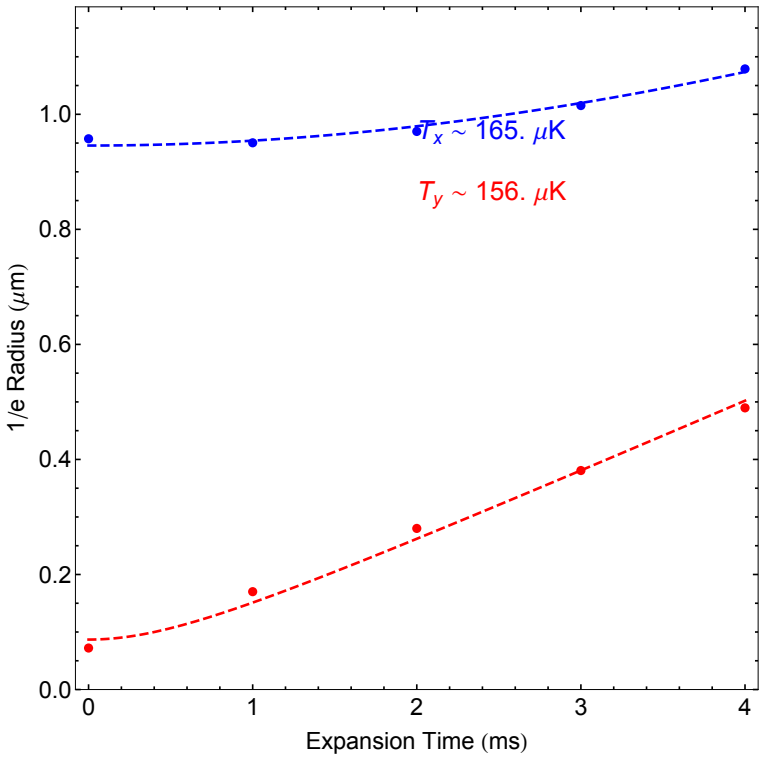

Figure 3.23: A fit to a time of flight measurement in each dimension of the FORT. By fitting the points, we arrive at a temperature near 160 μK.

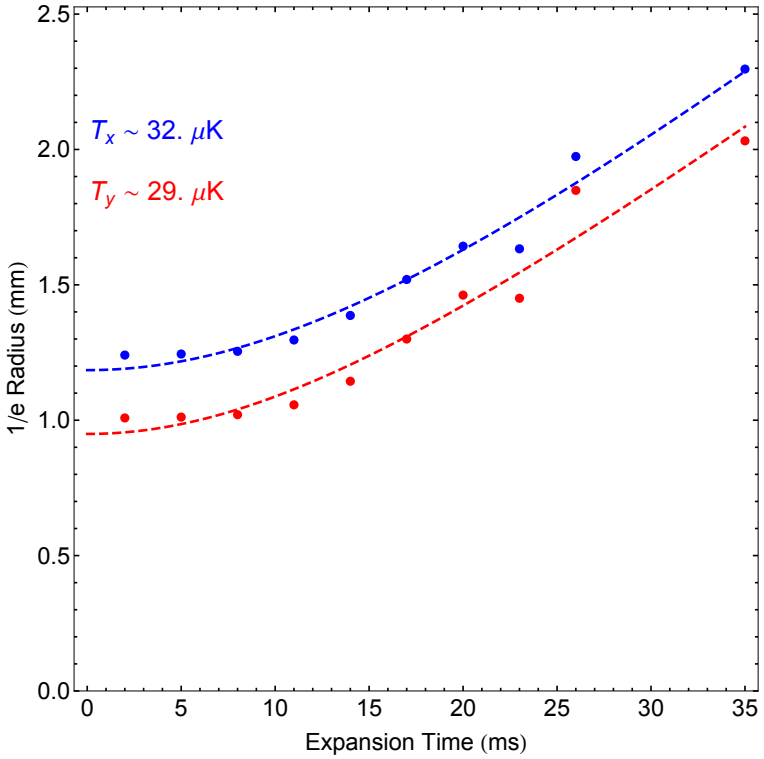

Figure 3.24: A fit to a time of flight measurement in each dimension of the MOT. By fitting the points, we arrive at a temperature near 30 μK.

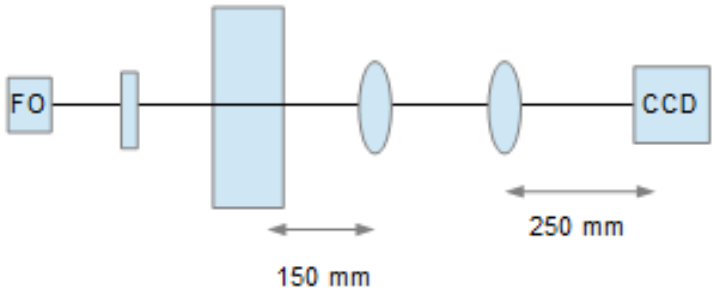

Figure 3.25: The probe light from a fiber optics (FO) is collimated and sent through the MOT and imaged on a CCD camera. When imaging an optical dipole trap, we insert two archromatic doublet lens after the MOT. The first lens (f=150 mm) is placed 150 mm from the MOT. The second lens (f=250 mm) is 250 mm from the camera.

Chapter 4

Permanent Magnet Zeeman Slower

4.1 A Clip-On Zeeman Slower Using Toroidal Permanent Magnets

Magneto-optic traps (MOT) are a staple in many cold atom experiments. Two primary methods of loading a MOT are to capture the cold tail of the background vapor [70] or to load from a slowed atomic beam [45]. In the latter case, an atom is slowed through the absorption of light from a counter-propagating laser detuned to the red of an atomic transition to compensate for the Doppler shift. A common method to account for the changing Doppler shift as the atom is slowed is a Zeeman slower [71]. It uses a position-dependent magnetic field to shift the energy levels of the atom so it remains in resonance with the laser and continues to be slowed.

In the first demonstration of Zeeman slowing, atoms enter a large magnetic field that decreases to zero, with the $m_F = |F| \rightarrow m_{F'} = |F+1|$ cycling transition driven by σ^+ polarized light [71]. However, the atoms leave the slower in resonance with the laser and their direction of motion may be reversed. In a second approach [72], the atoms enter a region of zero magnetic field. The field increases and σ^- polarized light drives the $m_F = |F| \rightarrow m_{F'} = -|F+1|$ cycling transition. As the atoms leave the slower, the magnetic field quickly decreases to zero and the atoms

decouple from the laser. Another approach uses a zero-crossing Zeeman slower, where the magnetic field starts with a positive (negative) value and ends with a negative (positive) value, while maintaining the general shape of a σ^+ (σ^-) slower [73]. Advantages of a zero-crossing slower include a smaller absolute magnetic field and the atoms decouple from the laser field as they exit the slower. Because level degeneracies occur when going through the zero-crossing region, a re-pump laser is needed to prevent spin precession [3].

Most Zeeman slowers are made using electromagnets, where numerous coils with differing number of turns of wire create a spatially-varying axial magnetic field. Electromagnetic Zeeman slowers can require currents large enough that active cooling of the slower is necessary. A permanent magnet Zeeman slower (PMZS) does not require a power source, is not in danger of electrically shorting, and does not heat the chamber (which can cause vacuum degradation). Some permanent magnet slowers have been demonstrated utilizing strong rare-earth magnets. Cheiney *et al.* [74] use NdFeB magnets in an eight-pole Halbach configuration to create a σ^- Zeeman slower, while Ovchinnikov has demonstrated a permanent magnet Zeeman slower using a series of magnetic dipoles [75, 76] to slow alkali and alkaline earth metals. Reinaudi *et al.* [77] have created a configurable permanent magnet Zeeman slower using servomotors to adjust the field in real-time to optimize slowing. Lebedev *et al.* [78] use a series of self-assembled spherical magnets to create the necessary field profile.

We present a guide to constructing a zero-crossing σ^+ Zeeman slower using a series of toroidal, flexible rubber magnets. The slower is cut longitudinally so that it "clips on" the vacuum chamber for easy attachment and removal for vacuum maintenance and baking. We simulate ^{85}Rb atoms slowed by our design and find an atomic flux similar to other slowers.

While the general theory of Zeeman slower construction is well known [73], we summarize some results that are relevant to the construction of a zero-crossing slower. We assume a two-level system, whose excited and ground states (energies E_e and E_g) experience linear Zeeman shifts, $\mu_e B$ and $\mu_g B$, and have a zero-magnetic-field energy separation of $\hbar\omega_o$. In one dimension, the magnetic field necessary to maintain a laser of frequency, ω resonant (to maintain maximum acceleration) with the atomic transition as the atom slows is given by:

$$\alpha B(z) = \Delta + kv(z), \tag{4.1}$$

where $\alpha \equiv (\mu_e - \mu_g)/\hbar$ accounts for the difference in Zeeman energy shifts between the ground and the excited state, $\Delta = \omega - \omega_o$ is the detuning, $k = 2\pi/\lambda$ is the laser wavenumber, and $v(z)$ is the spatially varying speed of the atoms along the Zeeman slower. If an atom of initial speed v_o begins slowing at $z = 0$ and comes to a final velocity v_f at $z = z_o$, the magnetic field is given by:

$$\alpha B(z) = \Delta + kv_o\sqrt{1 - \frac{z}{z_o}}. \tag{4.2}$$

To minimize the magnitude of the magnetic field for a zero-crossing Zeeman slower, we set $B(0) = B$ and $B(z_o) = -B$. This fixes $\Delta = -kv_o/2$, and the magnetic field becomes:

$$B(z) = \frac{kv_o}{\alpha}\left(\sqrt{1 - \frac{z}{z_o}} - \frac{1}{2}\right). \tag{4.3}$$

To determine the specifications of the slower, a speed v_o is chosen. The length of the slower is then given by $z_o = (v_f^2 - v_o^2)/2a$ where $a = \eta a_{\max}$ is the acceleration, $a_{\max} = \hbar k\Gamma/2m$ is the maximum acceleration (assuming saturation), Γ is the natural linewidth of the excited state, and η is a phenomenological parameter that accounts for imperfections in the apparatus. Previous models show that $0.4 < \eta < 0.7$ best reproduce actual systems [3, 79].

The desired magnetic field profile is created by a series of magnetic rings. We developed a *Mathematica*™ code that calculates the expected field from N rings of permanent magnets [80]. The physical parameter input includes the length of the slower, the number of magnets, one outer radius for all magnets, magnetization, width, spacing between each magnet, and the orientation. The program calculates the necessary inner radius of each magnet such that the difference between the PMZS field and the ideal field is zero at the center of each magnet. Restrictions are placed on the size of the inner radius such that it is neither larger than the outer radius nor smaller than the inner tube to which it is attached.

We first model a previously demonstrated zero-crossing σ^+ slower [3] using an initial velocity of 365 m/s, a final velocity of 10 m/s, $\eta = 0.72$, and an overall

length of 83 cm. The slower is designed to fit over a tube with an inner radius of 1 cm. We match the ideal profile using 54 permanent magnets with an outer radius of 8.0 cm and a μM equal to 2100 G, where μ is the permeability of the material and M is the magnetization. (2100 G is chosen because it is commercially available.) To provide the negative portion of the field, the 54th, 52th, 50th, 48th, and 46nd magnets are flipped in orientation. Fig. 4.1 shows the predicted magnetic field and the ideal magnetic field profile similar to the slower by Bell *et al.* [3]

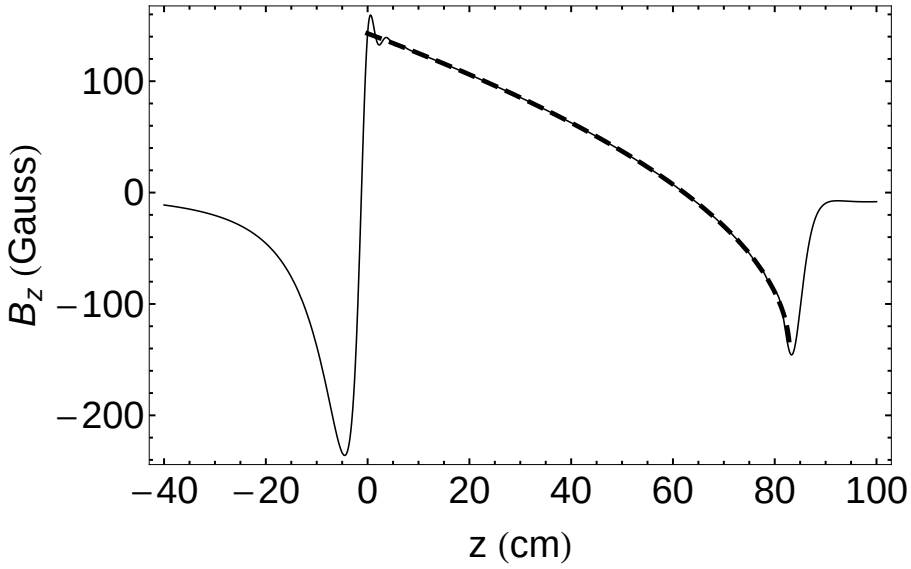

Figure 4.1: The predicted magnetic field profile a PMZS (solid) that closely matches the ideal profile (dashed) given for the zero-crossing slower by Bell *et al.*[3] The predicted magnetic field profile using permanent magnets matches the ideal curve to within ± 1 G between 5 cm and 76 cm.

In the slowing region, the magnetic field at the very beginning and end of the slower deviates from the calculated profile, and we do not expect slowing to occur. This is observed in all of our calculations. However, throughout the rest of the length of the slower, the predicted curve is within ±1 G, implying consistent

cooling given that detuning variations will be within the natural linewidth of the transition. The residual magnetic field may affect experiments less than 20 cm from the output. Since the fringe field is constant, it can be eliminated with bias coils or mu metal.

To experimentally test if a real PMZS could reproduce the theoretical Zeeman slowing magnetic field profile, we built a prototype. Due to apparatus limitations, the length of the slower is 45.72 cm. For the target magnetic field profile, we assume an initial speed of 300 m/s, a final speed of 5 m/s and η equal to 1. The slower consists of 25 magnets, each 1.27 cm wide and with an outer radius of 5.715 cm. A 0.635-cm-wide spacer is placed between each magnet. Figure 4.2 shows the ideal field for the device (Eqn. 4.3) and the predicted field from the PMZS after calculating the necessary inner radii. Calculations show a shorter Zeeman slower uses smaller magnets and makes it easier to match the desired field. Lengthening the slower much over 100 cm makes it challenging to smoothly match the theoretical profile without making the slower heavier and wider.

Our PMZS was fabricated using 50 square flexible magnetic sheets of 11.43 cm x 11.43 cm x 0.635 cm (two of which are glued together to give a thickness of 1.27 cm) from Adams Magnetics. Twenty four rigid Styrofoam rings were cut with an inner radius of 2.67 cm, an outer radius of 11.43 cm and a thickness of 0.635 cm to be used as spacers between the magnets. Placing spacers between the magnets reduces the overall cost of the slower, reduces the weight, and allows for easier

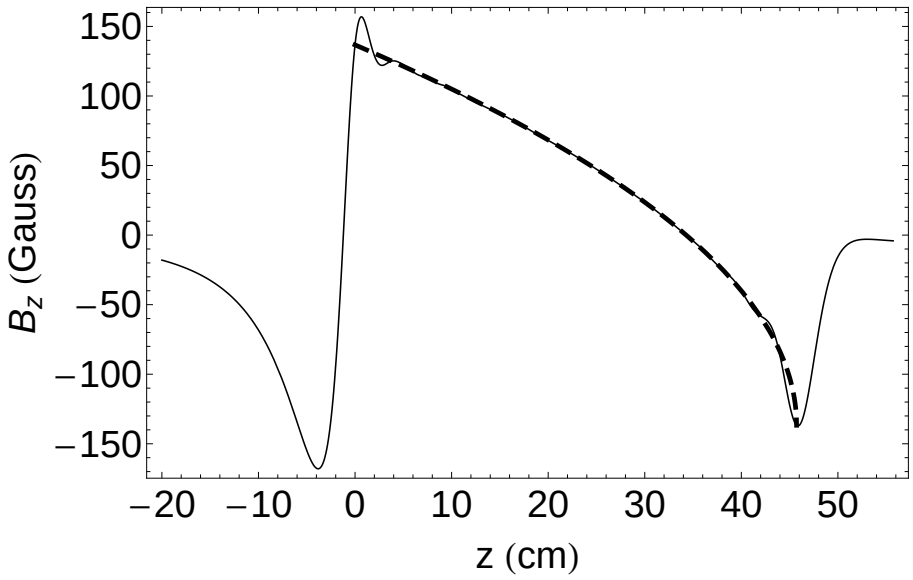

Figure 4.2: The theoretical magnetic field profile for a permanent magnet Zeeman slower (solid) that closely matches the ideal profile (dashed) for the prototype we constructed. The predicted magnetic field profile using permanent magnets matches the ideal curve to within ± 2 Gauss between 4 cm and 42 cm.

construction. This is especially true when creating the negative magnetic field where the orientation of some magnets is reversed. If necessary, one may attain a larger and smoother field by reducing the size of the spacers or eliminating them entirely. For magnets with an inner radius close to the outer radius, a rigid Styrofoam ring was used as filler inside the magnetic ring for support. The magnets and rigid Styrofoam filler were slid over 1 inch polyvinyl chloride (PVC) pipe. We applied glue between each magnet and spacer and between the spacer and the PVC. Unfortunately, the filler absorbed the glue and expanded. We compressed the slower to the intended length; however, the magnet position no longer matched the calculation to the necessary precision. After assembly, the slower was cut

down the middle. A stainless steel shell was attached around each half, the halves connected via screws, and attached to a vacuum tube with an inner radius of 0.5 cm. Figure 4.3 shows a picture of the final product.

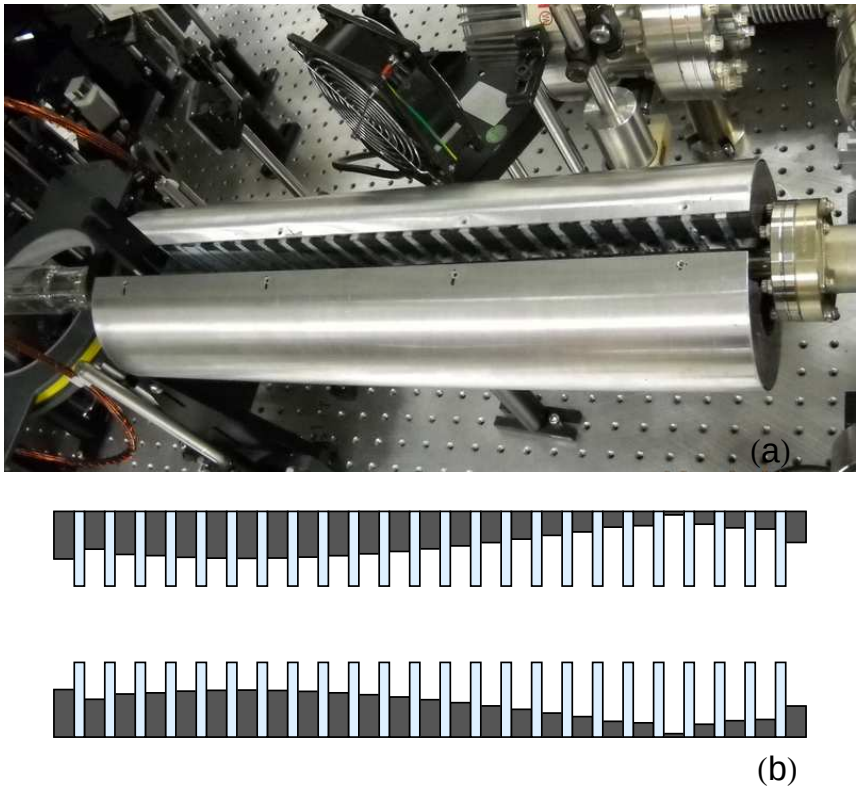

Figure 4.3: (a) A photo of the assembled permanent magnet Zeeman slower. (b) A pictorial representation of the radius of each magnet (varying) and the spacers (constant).

We measured the effect of cutting the magnets in half on the magnetic field. The on-axis magnetic field of a single ring was measured before and after cutting the magnet (Fig. 4.4). The average difference in the magnetic field is 0.37 G. Calculations show a difference of this size will not lead to significant deviations from the expected field. We also measured the variation in the z-component of

the magnetic field of the slower off-axis near the peak magnetic field, along the two radial axes parallel and perpendicular to the cut (Fig. 4.5). The variation from the on-axis field observed over the length of the inner radius of 0.5 cm is small enough to not significantly affect the trajectories. This is verified in the full 3D simulations below. We find the variation is much less at lower fields along the slower. There is a difference between the two components of the magnetic field, indicating an effect from cutting the magnets. However, the effect (<0.5 G) is negligible.

An additional source of error is the variation in magnetization. The specified magnetization of the magnets was $\mu M = 2100$ G. We cut multiple magnets into toroids and measured the value of μM for each magnet by matching the magnetic field profile to a theoretical curve (Fig. 4.4). The average value is 2087 ± 6 G. We simulated the difference in the magnetic field profile for μM equal to 2100 and 2087 G with a fixed inner radius. The maximum deviation over the length of the slowing region is ± 1.5 G. The uncertainty in the measurement of μM is affected by the standard precision of machining (0.005 inches, the precision with which the flexible magnets can be cut is not as high as other materials). This implies that the actual variation in μM may be smaller and that machining the flexible magnets to a higher precision will lead to an increased accuracy in matching the desired profile.

The axial magnetic field profile of the PMZS was measured by a Hall probe

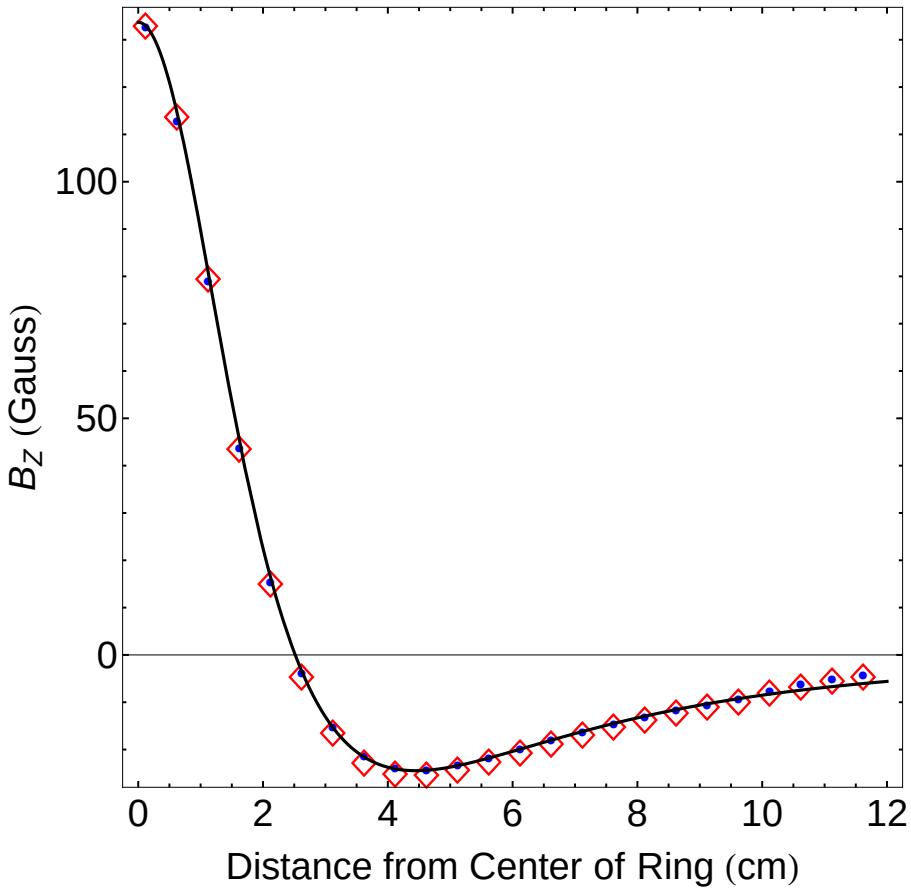

Figure 4.4: The magnetic field profile along the axis of a single permanent magnet toroid before cutting (solid circle) and after cutting (open diamonds) overlapped with the simulated curve. The average difference in the magnetic field before and after cutting is 0.37 G.

(Lakeshore Model 420) in one-cm increments on a translation stage. Figure 4.6(a) shows a comparison between the measured magnetic field profile of the PMZS and the predicted field profile. The average deviation from the expected field between 1 cm and 42 cm is 4.6 G. Over the first centimeter and the last 3 cm of the slower, the average difference is larger as predicted by our model and cooling is not expected in this region (Fig. 4.2). The deviations in the center region are also larger than

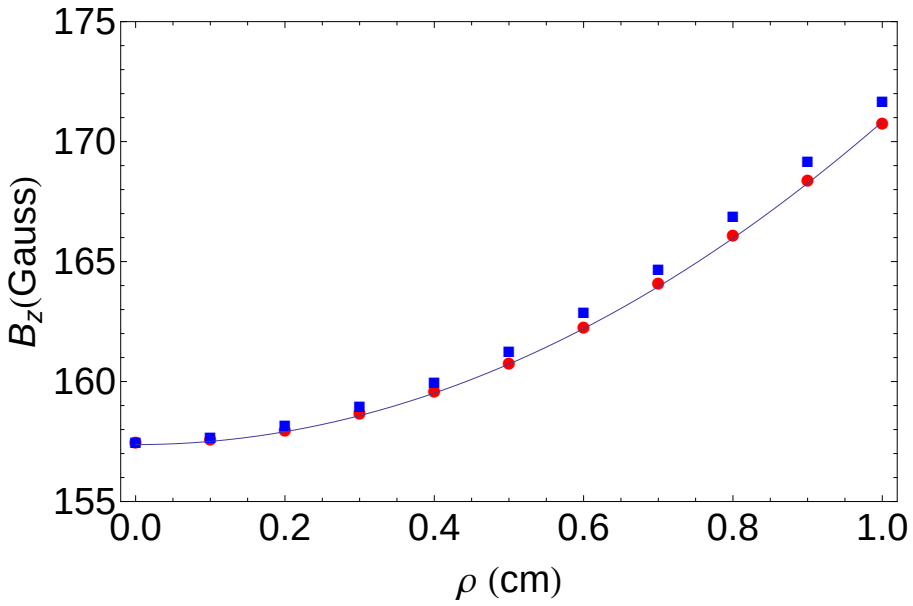

Figure 4.5: The z-component of the magnetic field as a function of the radial coordinate, ρ measured near the field maximum ($z = 0.88$ cm), both parallel (red circles) and perpendicular (blue squares) to the direction of the cut of the slower. The theoretical magnetic field curve (solid line) is given as a function of distance from the axis. While the curve extends to 1 cm, the tube has a physical radius of 0.5 cm.

expected from our model.

To test the variations of the field as a function of ρ, we also measured the z-component of the field along the z-direction for a fixed off-axis position, $\rho =$ 0.78 cm (Fig. 4.6b). We compare this to a theoretical field that uses a Taylor expansion of the on-axis magnetic field to fourth order in ρ [81]. The off-axis predicted field varies from the on-axis desired field on the order of a few Gauss within the first and last 2.5 cm of the slower, but varies less than 0.2 Gauss elsewhere. When comparing the measurement to the predicted field, we find similar trends to the on-axis comparison, with dips in the magnetic field near 10 cm and

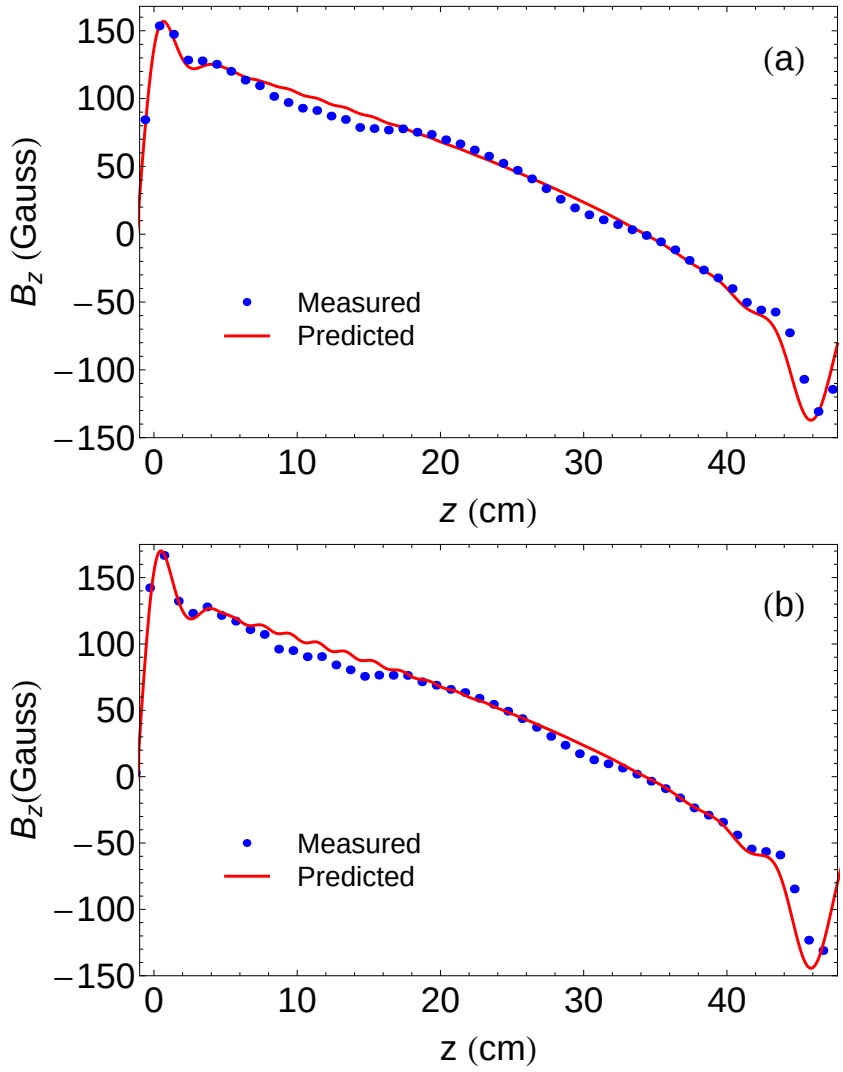

Figure 4.6: (a) The measured (dots) and predicted (solid) magnetic field profile for the PMZS prototype. The average deviation from the expected field between 1 cm and 42 cm is 4.6 G. (b) The measured (dots) and predicted (solid) magnetic field profile off-axis for the PMZS prototype at a radius of 0.78 cm.

28 cm, and a higher field at the end of the slower.

The most significant error is due to the magnet misalignment caused by the compression of the slower to the correct length after the glue was absorbed by the filler material. The resulting positions of the magnets were measured and found to

deviate from the desired values by amounts as large as 0.55 cm. Calculating the magnetic field given the *measured position* of each magnet, we found deviations in the field on the order of the error observed. Using non-absorbing material as spacers or constructing a plastic shell to hold the magnets will reduce the position error down to the size of the machined material, usually 0.001 inches. With this change, we predict the resulting field will match the ideal field in the slowing region to $\pm$ 1 G.

We use a Monte-Carlo simulation to predict the total flux and final velocity distribution of atoms passing through a Zeeman slower. We randomly select atoms that can potentially be slowed and captured by a MOT given their radial and axial velocity from a Maxwell Boltzmann distribution of atoms emitted by an effusive source. We model the acceleration of the atoms by the slowing laser as [73],

$$a(z,\rho) = \frac{\hbar k \Gamma}{2m} \frac{s_0}{1 + s_0 + \frac{4}{\Gamma^2}[\delta_0 + k v_z(z,\rho) - \alpha B_z(z,\rho)]^2}, \tag{4.4}$$

and solve the Newtonian equations of motion. The Monte-Carlo simulation is three-dimensional in magnetic field and trajectories.

Figure 4.7 shows a variety of velocity curves for atoms without radial velocity both on- ($\rho = 0$) and off-axis ($\rho = 1$ cm) for our theoretical slower that matches the profile of that from Bell *et al.*[3] The laser is detuned to the red of the $F = 3$ to $F = 4$ transition by 1.6 GHz with an s_0 of 27, which corresponds to a beam with a power of 160 mW and a $1/e^2$ radius of 1 cm. Atoms with an initial velocity

below 35,000 cm/s are cooled to approximately 3,500 cm/s, well within the typical capture velocity of a MOT. We find that atoms leaving the slowing region off-axis have a slightly higher final velocity due to the larger magnetic field, but still within the capture range of the MOT. The magnetic field before $z = 0$ cools lower-velocity atoms prematurely, and prevents some from reaching the MOT. Full three-dimensional simulations show that 27% of the possible atoms based on their axial and radial velocity are slowed too early and do not reach the MOT assuming the magnetic field keeps the atoms in resonance with the slowing laser. However, as described by Dedman *et al.*[79], when

$$\frac{2m\alpha}{\hbar k^3\Gamma}\frac{dB}{dz}(\alpha B - \Delta) > 1, \tag{4.5}$$

atoms are unable to stay in resonance with the laser field and are no longer cooled. The field shown fails this condition at -7.5 cm, so atoms are no longer pre-cooled at this point. Thus, our calculations are a lower limit, since we expect a large fraction of those predicted to be lost in the simulation to be recovered in the experiment. Atoms initially at 120 °C leave a collimation tube ($r = 0.5$ cm) 30 cm from the start of the slower. The atoms pass through an 83 cm slowing region with a radius of 1 cm and travel 20 cm farther to the capture region. We calculate a flux of 4.8×10^8 atoms s^{-1} cm^{-2}, comparable to other slowers at a similar temperature [74]. Also, the simulations assume a simple effusive source, and improvements have been demonstrated to increase the initial number of atoms to be slowed [3].

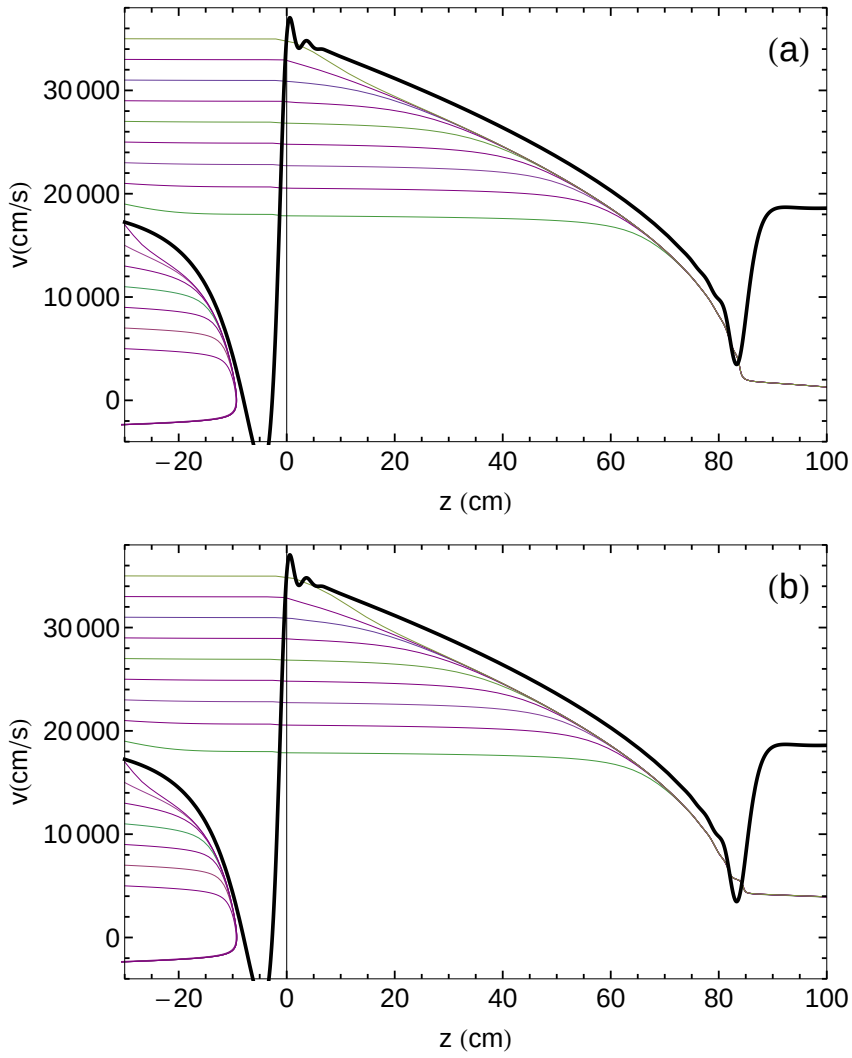

Figure 4.7: Simulated velocity curves (a) on-axis and (b) off-axis ($\rho = 1$ cm) for the Zeeman slower similar to the slower by Bell et al.[3]. The magnetic field profile is shown in black.

Figure 4.8 shows a variety of velocity curves for atoms without radial velocity both on- ($\rho = 0$) and off-axis ($\rho = 1$ cm) for our prototype slower. The laser is detuned 1.2 GHz below the $F = 3$ to $F = 4$ transition with an s_0 of 26, which corresponds to a beam with a power of 41 mW and a $1/e^2$ radius of 0.5 cm. We

see cooling of atoms with a maximum initial velocity of 29,000 cm/s to 1,500 cm/s. Similar to the previous calculation, the simulations predict 25% of the flux is slowed too early, but we expect that to be conservative, since the field violates the condition in Eqn. 4.5 before the atoms are lost. With a Zeeman slower tube radius of 0.5 cm and oven temperature of 90 °C, we calculate an atomic flux of 0.8×10^8 atoms s^{-1} cm^{-2}. However, this prototype is a proof-of-principle device to re-create the theoretically predicted field and is not explicitly optimized for loading flux.

There are several future extensions and improvements. We have used our code to model a standard σ^+ (non-zero crossing) slower. The desired profile can match the ideal profile to within $\pm$ 1 Gauss. The larger field requires a larger outer radius (18 cm), or higher magnetization material. To improve the design and roundness of the magnets, one can machine each half of the magnetic ring separately and then assemble the slower at the end. This method would remove the field asymmetry seen in Fig. 4.5, but increase the amount of material needed and the construction time. The most critical improvement is the use of solid (non-porous) material for the spacers.

The advantages of using flexible permanent magnets over electromagnets include no excess heating, no risk of electrical shorts, and no power source. We provide a simple design that can be removed easily, and theoretically matches a previously demonstrated zero crossing slower [3]. We built and tested a prototype

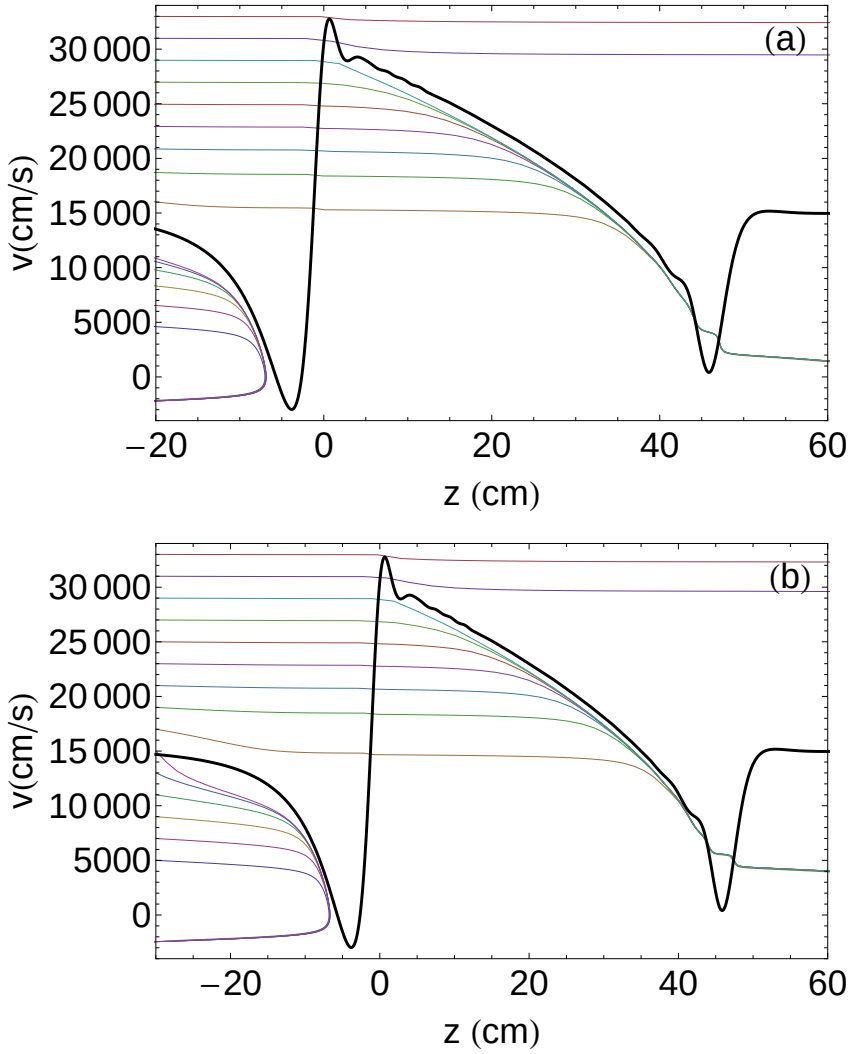

Figure 4.8: Simulated velocity curves (a) on-axis and (b) off-axis for the prototype Zeeman slower. The magnetic field profile is shown in black.

that demonstrates the ability to closely reproduce the fields for a zero-crossing Zeeman slower. Simulations predict an atom flux comparable to other slowers at similar temperatures.

Chapter 5

Observation of Feshbach Optimized Photoassociation

5.1 Introduction

Previous work by Miller *et al.* [48] identified photoassociation resonance lines in $^{85}Rb_2$ between 12530 cm^{-1} and 11630 cm^{-1}. In their analysis, they distinguish single excited molecular vibrational lines beyond 12450 cm^{-1}, and differentiate between the 1_g and the 0_g^- excited molecular states. The same group investigated Feshbach resonances using photoassociation [58]. The study focuses specifically on the 0_g^- state of $^{85}Rb_2$. From this study, they measured the Feshbach resonance for the $|F{=}2, m_F{=}2\rangle$ of the 0_g^- state to have a peak near 164 $\pm$ 7 G and a width of 5.9 $\pm$ 2.1 G. Our theory for similar states predicts both the position and width of the resonance to be consistent with their report.

Our goal is to combine the two processes of photoassociation and a Feshbach resonance to observe lines previously unobserved in the 0_g^- state of $^{85}Rb_2$. As mentioned in the introduction, the goal of the study is to map out the molecular potential to improve theoretical curves for $^{85}Rb_2$ that are used in a variety of experiments.

5.2 General System Set-up

The set-up for the system has already been discussed in Chapter 3, but I will cover the points necessary for the extension to FOPA. We currently use one laser for the FORT and photoassociation. The laser has a linewidth of approximately 40 GHz (1 cm^{-1}=33 GHz) and power of 2.3 W at 805 nm. The beam is focused to a waist of approximately 20 μm, leading to a trap depth of 8.7 mK. The laser is passed through a zero-order half wave plate at 805 nm. We use a zero-order wave plate because it is less sensitive to changes in frequency than a multi-order wave plate. The wave plate allows us to rotate the polarization of the laser to investigate the predicted polarization effects on the PA rate [2].

The Feshbach resonance is induced by a pair of Helmholtz coils powered by a power supply with up to 400 A. We typically do not go above 70 A, and not for a long period of time (hundreds of ms) with seconds between each duty cycle. The magnetic field coils for the magneto optical trap are placed inside the Feshbach resonance coils. This aligns the two fields and ensures that the magnetic field from the Feshbach coils is at the center of the MOT.

Prior to running the experiment, we optimize the magnetic field and the photoassociation/FORT laser. We first calibrate the magnetic field for the Feshbach resonance. The current supply must be turned on at least one hour prior to taking data to stabilize the electronics and temperature. Of that hour, the supply is running at low current (roughly 6 A) for approximately 30 minutes. After 30

minutes, a voltage is sent from the computer via LabVIEW to the current supply. The output voltage from LabVIEW and corresponding output current from the supply are calibrated, and we calculate the voltage to magnetic field conversion. We initially used a high current IGBT switch on the larger current supply similar to the switch used on the MOT coils. However, the LabVIEW voltage to current conversion was too variable and unstable over short time periods (on the scale of minutes). We removed the switch and the voltage to current conversion became repeatable on a day to day basis.

Next, the Ti:S output is optimized for power and mode. First, the full power beam is expanded and attenuated using a neutral density filter. Placing the neutral density filter directly in the beam path when the laser is full power and its original size will burn a hole in the filter. The output of the Ti:S is monitored while the output couplers are adjusted on the outside of the laser box. The two vertical output couplers are adjusted iteratively to maximize power. The same is done for the horizontal couplers, and then the vertical is re-done, and the horizontal. This process is repeated until no power increase is observed. The typical power at 805 nm is 2.3 W. The output couplers should require only very small adjustments day-to-day. Adjusting the output couplers will change the path of the Ti:S slightly. The focus of the laser, and therefore position of the FORT, may need to be re-positioned after adjusting the output couplers.

The laser is tuned to the desired frequency, and we monitor the mode of the

laser on a white index card. The frequency of the Ti:S is chosen based upon theoretical maxima in the Feshbach optimized photoassociation rate for the 0_g^- state as calculated by our group [2]. The output mode of the laser will cycle between Hermite Gaussian and Gaussian modes as it is tuned. A Hermite Gaussian mode will not focus down well and the trapped atom number and density will be significantly reduced, if a FORT forms at all.

During data taking, the mode must be monitored. The Ti:S will drift in frequency, typically increasing in frequency on the order of tenths of an inverse cm every few minutes. We do not have an exact number on the frequency drift due to the large linewidth of the laser. With a linewidth of 40 GHz, changes on the order of 0.1 cm^{-1} do not require an adjustment of the grating. However, the mode of the laser can change while drifting and effect the number of trapped atoms, and therefore must be monitored. The mode can be changed by slightly adjusting the grating, but this can lead to a hop in the frequency. The output couplers can also be changed a small amount, which will not change the frequency, but it will adjust the mode. As long as the change to the couplers is small, the position of the focus will not need to be readjusted.

The sequence for loading the FORT, inducing a Feshbach resonance, and imaging the FORT is shown in Figure 5.1. The process begins by loading a MOT with 10^7 to 10^8 ^{85}Rb atoms, a density of roughly 5×10^9 cm^{-3}, and a temperature between 30 and 100 μK. The density is limited by radiation pressure, as indicated

by the appearance of a flat top MOT. The density cannot be increased by going to a Dark Spot MOT due to experimental limitations. The atoms are loaded into the FORT, the MOT is turned off, and the current to the Feshbach coils is turned on. The atoms remain in the FORT for 500 to 700 ms, which varies based upon how close the Ti:S is to the D1 transition. The turn off and turn on time for the current supply is 30 ms. We use absorption imaging to view the FORT and later extract the atom number and density. After 500 to 700 ms, the FORT contains an atom number of between 10^5 to 10^6 atoms, a peak density of 10^{10} cm^{-3}, and a temperature between 50 and 200 μK.

A LabVIEW code changes the magnetic field from run to run, within the range of 154 G to 166 G in increments of 1 G. We randomize the order of the magnetic field to minimize the chance that a false signal would appear from laser drift or other time dependent variables. Once all the images are taken, they are converted into ASCII and imported into a *Mathematica* code to reduce the data into atom number and density. The atom number and density at each magnetic field are then rearranged into linear order, the atom number is converted into fractional loss, and the final curve maps out the Feshbach resonance.

5.3 Results

We observe 3 different FOPA resonances (Figures 5.2, 5.3, 5.4). An example of a single data run is shown in Figure 5.5. The experimental frequencies are 12323 cm^{-1}, 12425 cm^{-1}, and 12483 cm^{-1}. Comparing to the theoretical predictions for

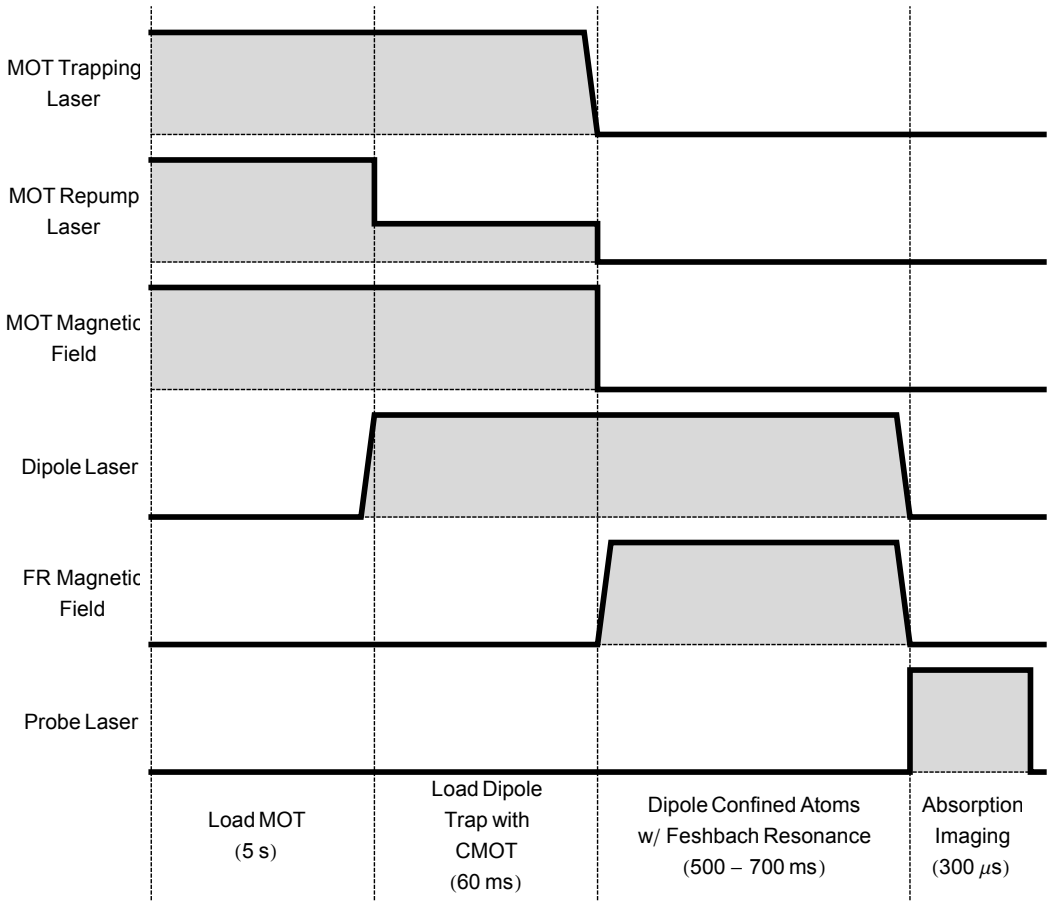

Figure 5.1: The timing sequence used for loading the FORT, inducing the Feshbach optimized photassociation resonance, and imaging. The steps are the same as when loading the FORT, but the duration that the atoms are kept in the FORT is increased, along with the addition of the magnetic field. The atoms are imaged using absorption imaging. The atoms are flashed with re-pump light for roughly 100μs before imaging with the probe laser.

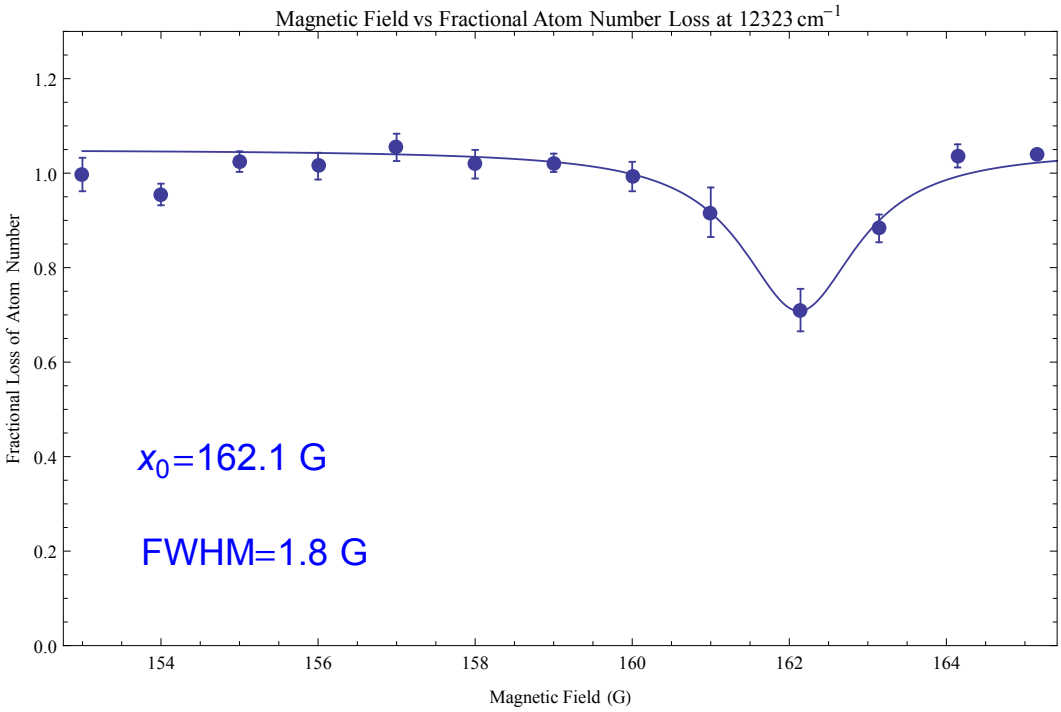

Figure 5.2: The magnetic field vs fractional atom number loss at 12323 cm^{-1}. The data is fit to a Gaussian. The central peak in the Feshbach resonance is found at 162.1 G with a full width at half maximum of 2.04 G. From our calculations, we predict this resonance corresponds to the ν=127 state of the 0_g^- excited molecular curve.

the 0_g^-, these frequencies correspond to the vibrational levels ν=127, ν=140, and ν=150, respectively (Figures 5.6, 5.7, 5.8). We find the experimental frequencies to agree to within 1 cm^{-1} of the theoretical positions. We compare these to the previously measured positions by Miller *et al.* [48]. The difference in frequency for the closest measured photoassociation line are 1 cm^{-1} (ν=127), 2 cm^{-1} (ν=140), and less than 1 cm^{-1} (ν=150). The difference in frequency is most likely due to the large linewidth of [58] and our lasers.

The experimentally measured and theoretically predicted [2] magnetic field

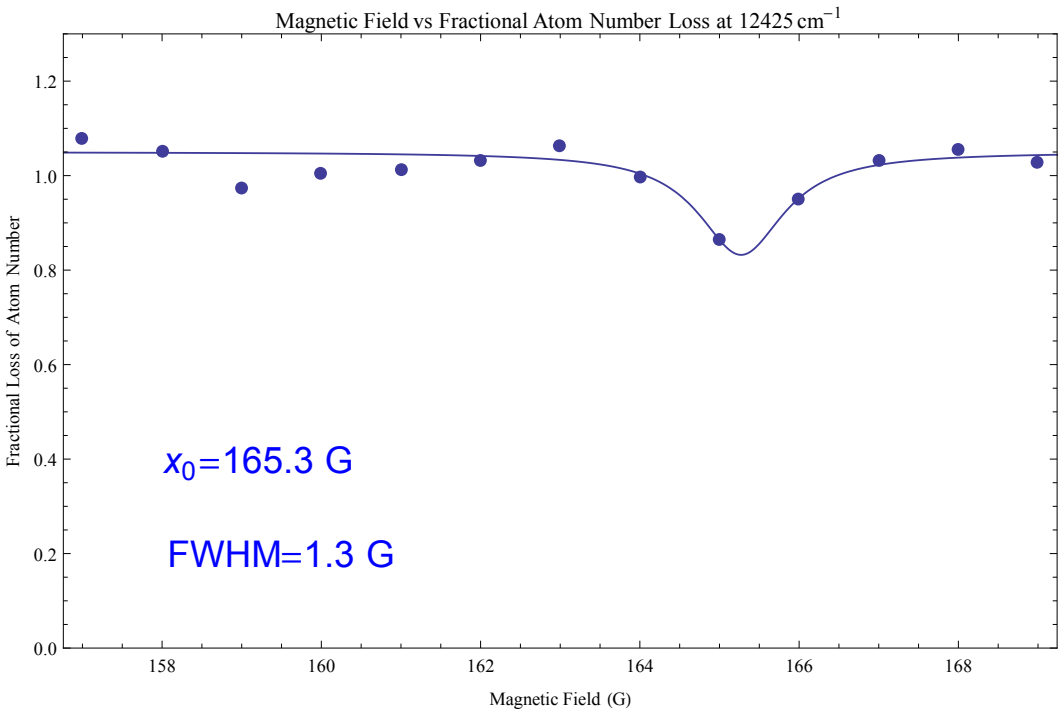

Figure 5.3: The magnetic field vs fractional atom number loss at 12425 cm^{-1}. The data is fit to a Gaussian. The central peak in the Feshbach resonance is found at 162.2 G with a full width at half maximum of 1.8 G. From our calculations, we predict this resonance corresponds to the ν=140 state of the 0_g^- excited molecular curve.

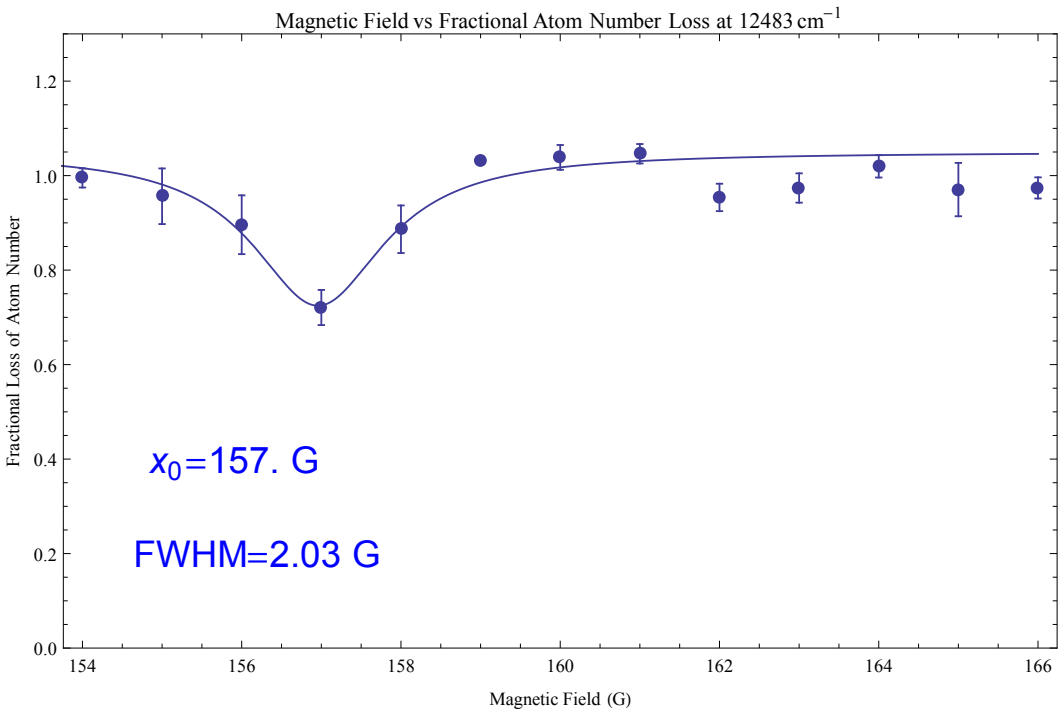

Figure 5.4: The magnetic field vs fractional atom number loss at 12483 cm^{-1}. The data is fit to a Gaussian. The central peak in the Feshbach resonance is found at 156.9 G with a full width at half maximum of 2.3 G. From our calculations, we predict this resonance corresponds to the ν=150 state of the 0_g^- excited molecular curve.

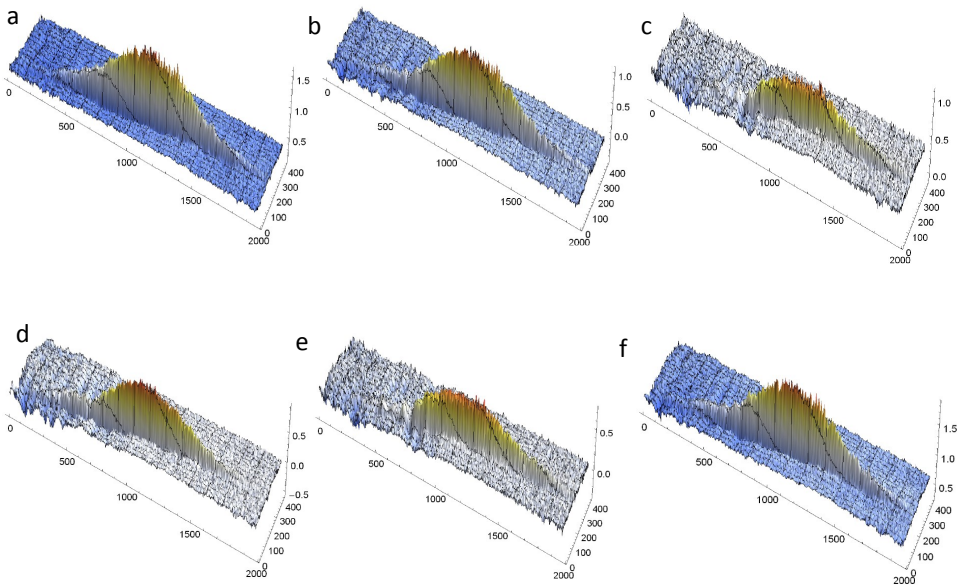

Figure 5.5: Absorption images of the FORT while sweeping the magnetic field through a Feshbach resonance at 12483 cm^{-1}. The magnetic field is swept from 154 to 159 G, with the resonance peaking at 157 G. The horizontal axes are the position in microns, while the vertical is the optical density. The vertical axis does change as the optical density is reduced.

resonance position for each level are 157 G/162 G (ν=150), 162 G/162 G (ν=140), and 162 G/162 G (ν=127). The experimental error in the magnetic field is $\pm$3 G. As shown by our theoretical work [2], the position of the resonance is dependent on the temperature of the atoms until it plateaus near 162 G for higher temperature (Figures 5.12, 5.13). We see a shift in the experimentally measured position of the central peak of the resonance of approximately plus or minus a Gauss. The data was shifted assuming that the shift in the position is due to a temperature variation between data sets. To average the data points for ν=150 and ν=127, the central magnetic field was chosen by where the majority of the central peaks fell.

There is a large discrepancy between the experimentally measured and theoretically predicted width of each of the resonances assuming a temperature of 100 μK. The measured and theoretical widths for each of the levels are 1.8/6.7G for ν=127, 1.3/7 G for ν=140, and 2.03/6.8 G for ν=150. We calculate the theoretical widths by first importing model data (Figures 5.6, 5.7, 5.8) and converting the PA rate to fractional loss. The loss rate (assuming no 3 body collisions because of our low density, even at a Feshbach resonance) is,

$$\frac{dn}{dt} = -K_2 n^2, \tag{5.1}$$

where K_2 is the two-body loss rate, n is the density, and t is the time. As most of the runs show a flat line for the change in atom number as the magnetic field is swept, we assume the background two-body loss rate is constant. We use the PA

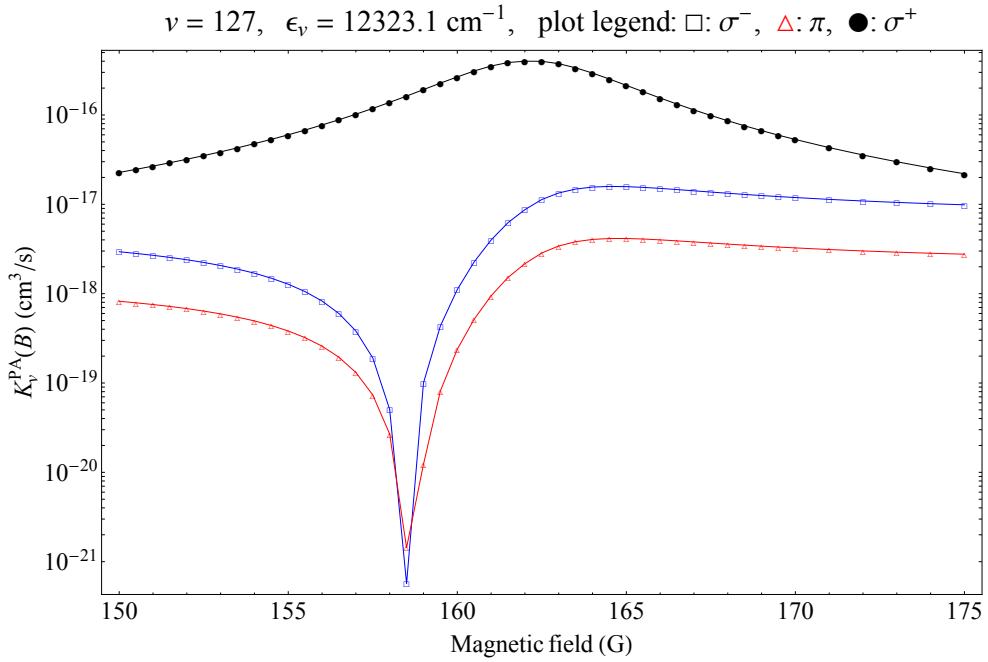

Figure 5.6: The effect of magnetic field on the photoassociation rate for each of the polarizations as the magnetic field crosses the Feshbach resonance [2].The plot is for the ν=127 state of the 0_g^- excited molecular curve and assumes a temperature of 100 μK. The σ^+ polarization dominates as the magnetic field is swept through the resonance, while the other two polarizations are a minimum. We expect any experimental results to only show contributions from the σ^+ light.

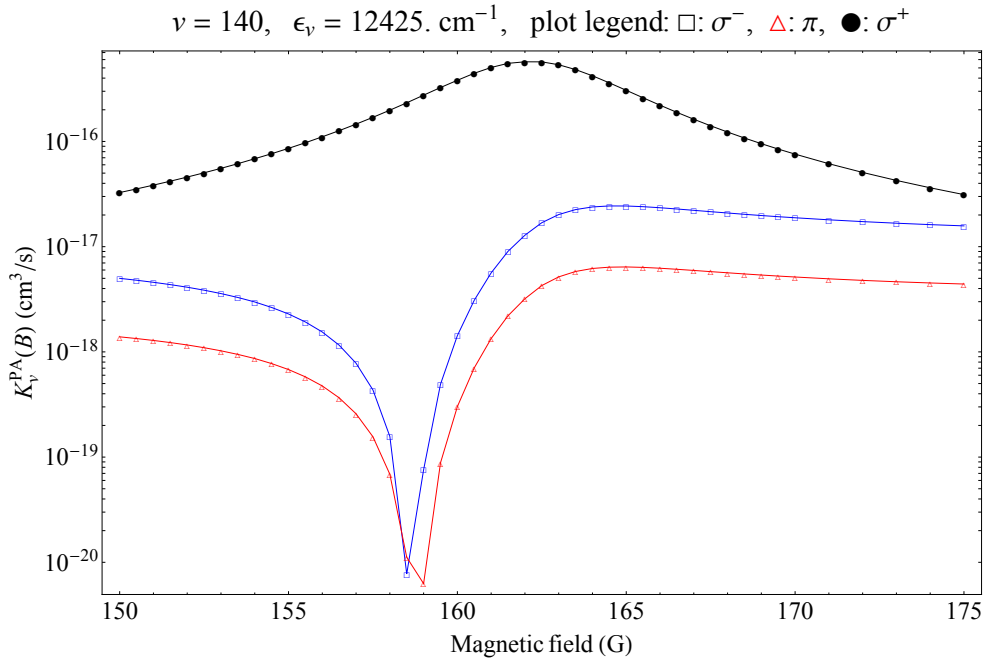

Figure 5.7: The effect of magnetic field on the photoassociation rate for each of the polarizations as the magnetic field crosses the Feshbach resonance [2].The plot is for the ν=140 state of the 0_g^- excited molecular curve and assumes a temperature of 100 μK. The σ^+ polarization dominates as the magnetic field is swept through the resonance, while the other two polarizations are a minimum. We expect any experimental results to only show contributions from the σ^+ light.

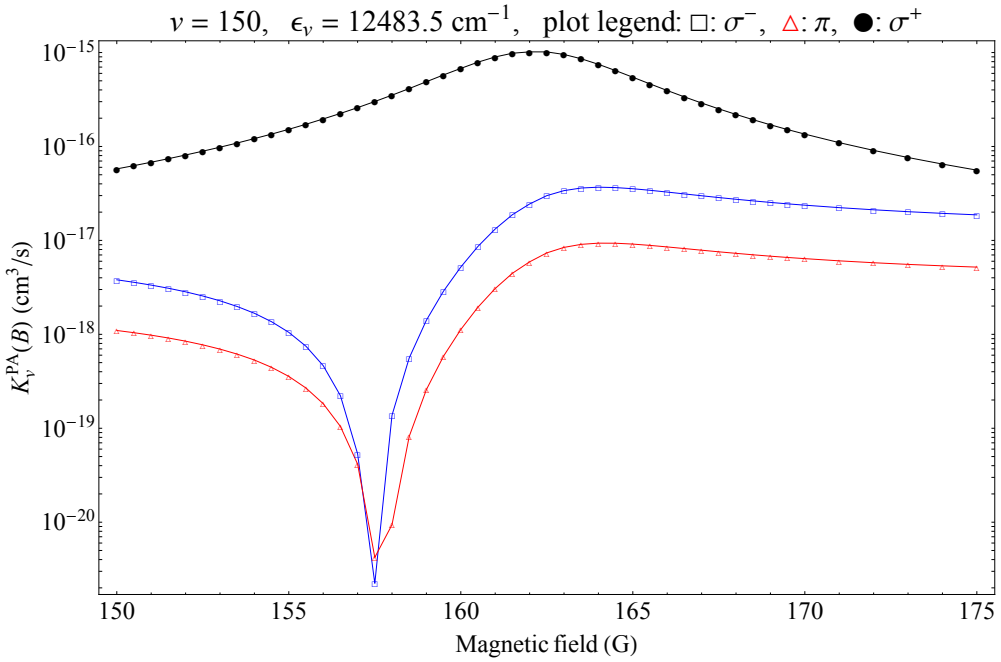

Figure 5.8: The effect of magnetic field on the photoassociation rate for each of the polarizations as the magnetic field crosses the Feshbach resonance [2].The plot is for the ν=150 state of the 0_g^- excited molecular curve and assumes a temperature of 100 μK. The σ^+ polarization dominates as the magnetic field is swept through the resonance, while the other two polarizations are a minimum. We expect any experimental results to only show contributions from the σ^+ light.

rate from [2] times a multiplier that adjusts for the intensity for the value of K_2. Re-arranging the equation, we arrive at,

$$n_f = \frac{n_0}{1 + n_0 K_2 t}, \tag{5.2}$$

where n_f is the final number of trapped atoms after some time t, and n_0 is the initial number of trapped atoms. We then divide by n_0 to arrive at the fraction of atoms lost,

$$\frac{n_f}{n_0} = \frac{1}{1 + n_0 K_2 t}. \tag{5.3}$$

The intensity of the laser is adjusted to match the theoretical fractional loss to the observed experimental loss. The resulting curve is fit to a Lorentzian and the central peak position and the full width at half maximum are extracted (Figures 5.9, 5.10, 5.11).

We attribute the difference between the experimental and theoretical widths to a variety of factors. First, we believe that the temperature of the cloud is more likely closer to 200 μK. As seen in Figures 5.12 and 5.13, the width of the resonance decreases as the temperature of the cloud increases. Secondly, the shot-to-shot variations in the data leads to an ambiguity in the measured fractional loss. The number of data sets averaged are 7 and 4 runs for 12323 cm^{-1} and 12483 cm^{-1}, respectively. The small number of data sets leads to the noise from individual sets having a larger effect in the data, increasing the uncertainty of the final widths.

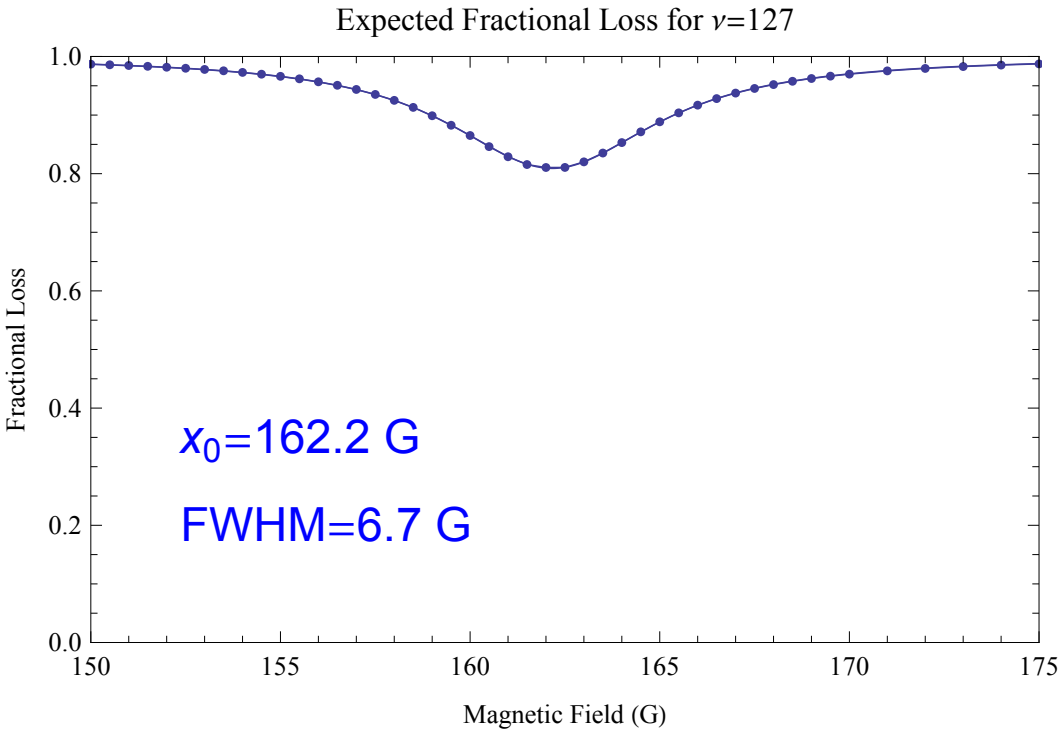

Figure 5.9: The theoretical fractional loss of atoms undergoing a FOPA transition [2]. The theoretical curve (dots) is calculated by converting the σ^+ photoassociation rate from Fig. 5.6 into fractional loss and adjusting the rate so that the peak fractional loss is at roughly the same level as the experiment. The data is then fit to a Gaussian and the position and width are extracted.

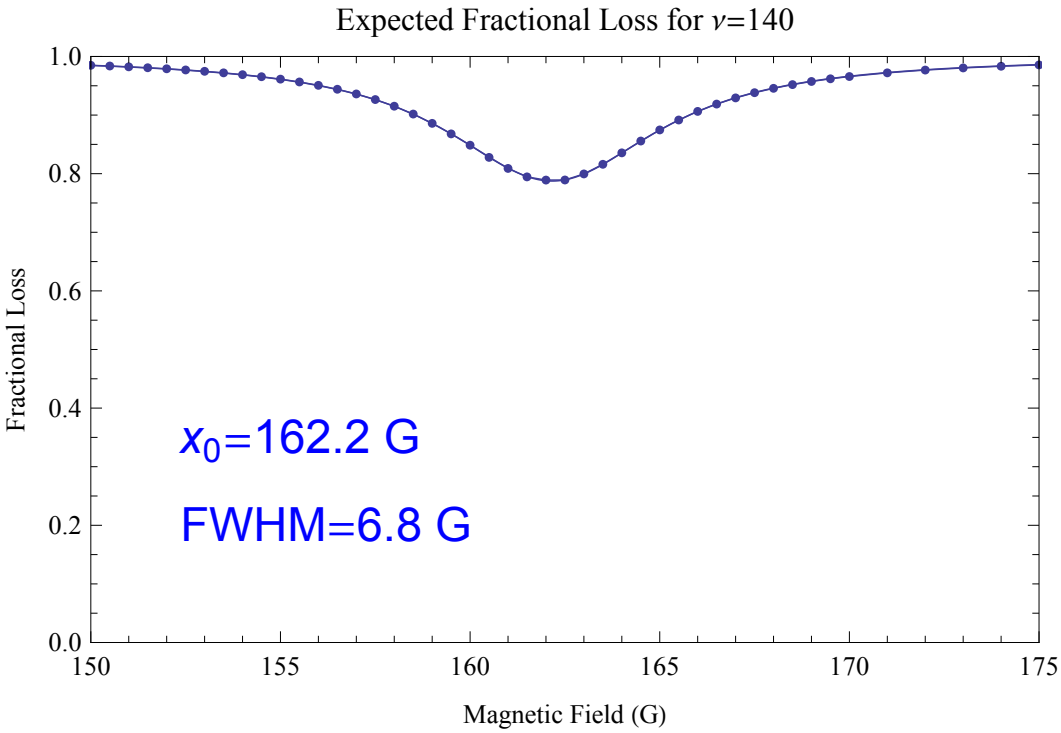

Figure 5.10: The theoretical fractional loss of atoms undergoing a FOPA transition [2]. The theoretical curve (dots) is calculated by converting the σ^+ photoassociation rate from Fig. 5.7 into fractional loss and adjusting the rate so that the peak fractional loss is at roughly the same level as the experiment. The data is then fit to a Gaussian and the position and width are extracted.

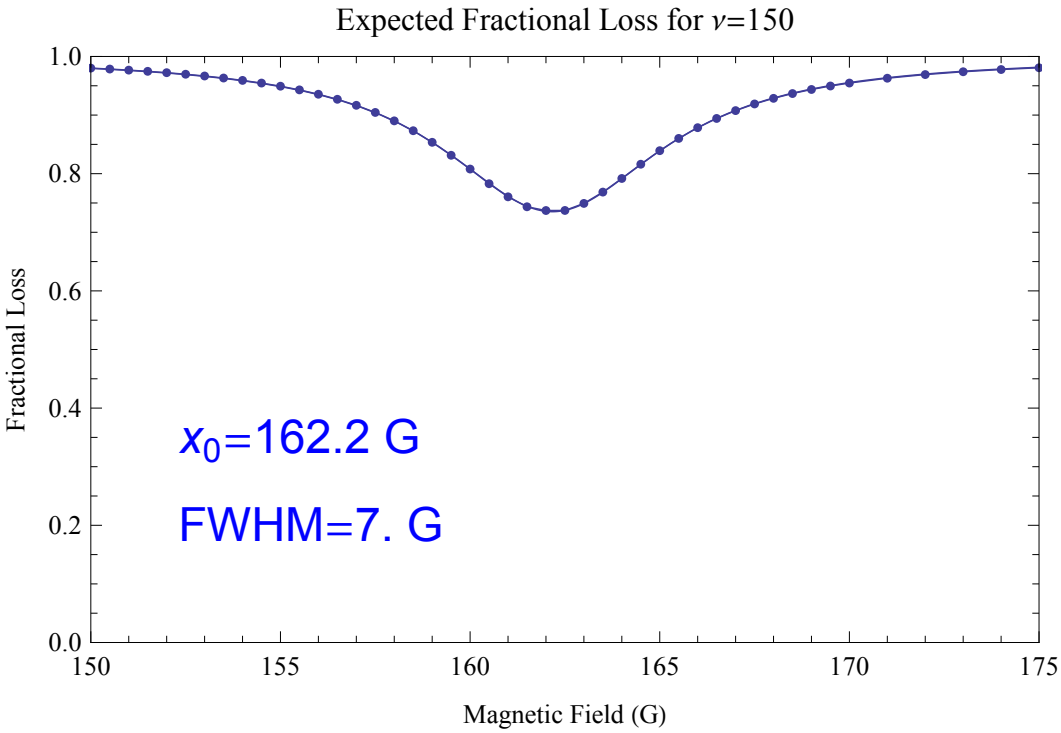

Figure 5.11: The theoretical fractional loss of atoms undergoing a FOPA transition [2]. The theoretical curve (dots) is calculated by converting the σ^+ photoassociation rate from Fig. 5.8 into fractional loss and adjusting the rate so that the peak fractional loss is at roughly the same level as the experiment. The data is then fit to a Gaussian and the position and width are extracted.

Finally, the uncertainty of the frequency of the laser, the relative drift in frequency (in comparison to a standard photoassociation transition linewidth), and the large linewidth would lead to fluctuations in the peak fractional loss. For example, the laser in some of the data sets may have been drifting off resonance. This would lead to a reduction in the photoassociation rate, leading to a narrower linewidth. The effect of moving the laser off resonance in frequency has been verified via our theoretical calculations.

The position of the FOPA resonance is indicative of the temperature of the graph, as mentioned. When looking at the peak position versus the full width at the half maximum, we see a trend for the FWHM to decrease with increasing peak resonance position 5.14. This trend is predicted by our theory as well.

We did study the effect of the polarization on the PA rate. The theoretical photoassociation rate curves show different rates for the different polarizations of the laser (Figures 5.6, 5.7, 5.8). We studied the effects of the FORT polarization in both the π and σ^+/σ^- polarization. Due to the orientation of our PA laser with respect to the magnetic field created by the Feshbach coils, we are unable to create a pure polarization. Because the σ^+ light PA transitions is orders of magnitude higher than the other two polarizations, we assume the signal is from the σ^+ polarization. We do not see any significant difference between data taken with mostly π light and mostly σ^+/σ^- light. We attribute this to the small sample size.

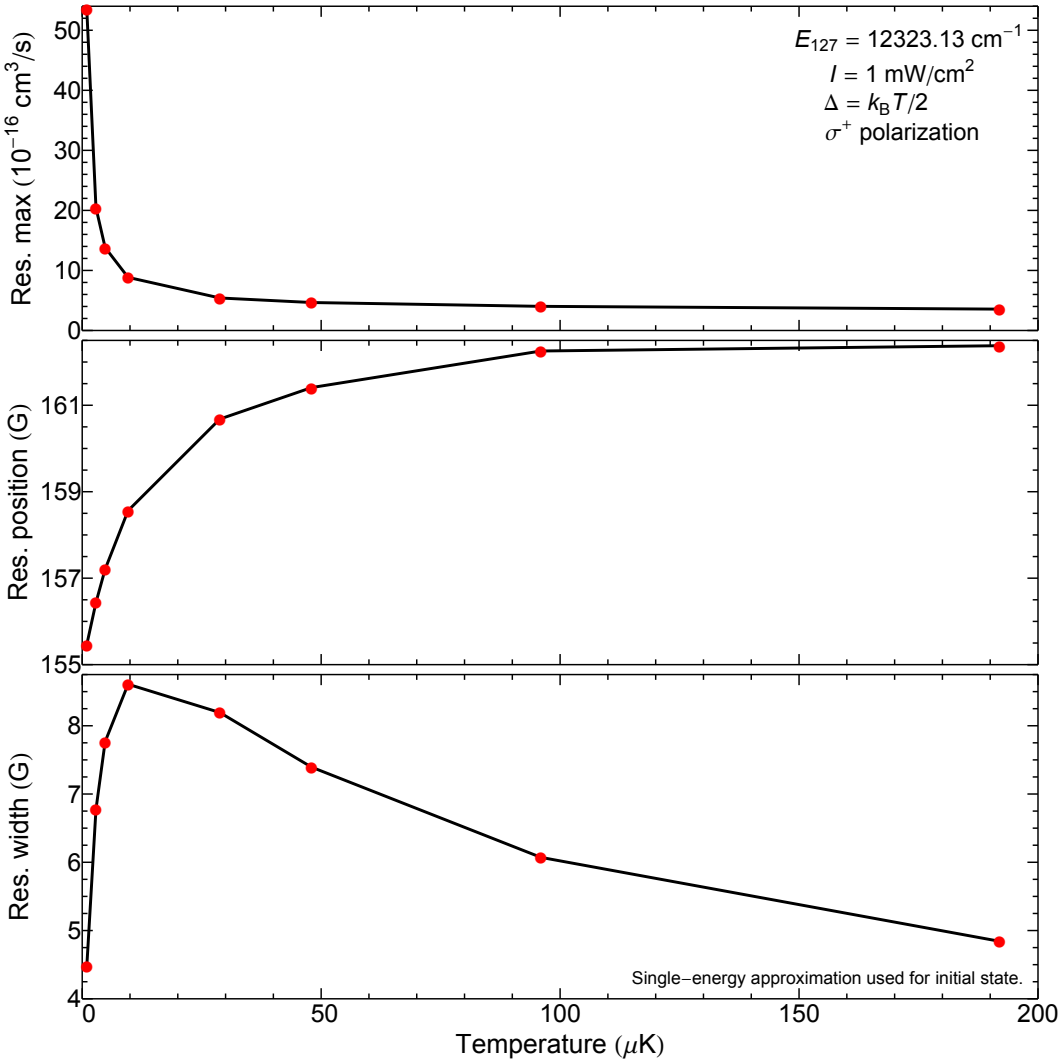

Figure 5.12: The effects of the temperature of the atoms trapped in the FORT on the resonance maximum signal, the resonance position, and the resonance width for the ν=127 state as calculated by [2]. From the theory, we suspect that the temperature of our FORT is over 100 μK for most of the trials.

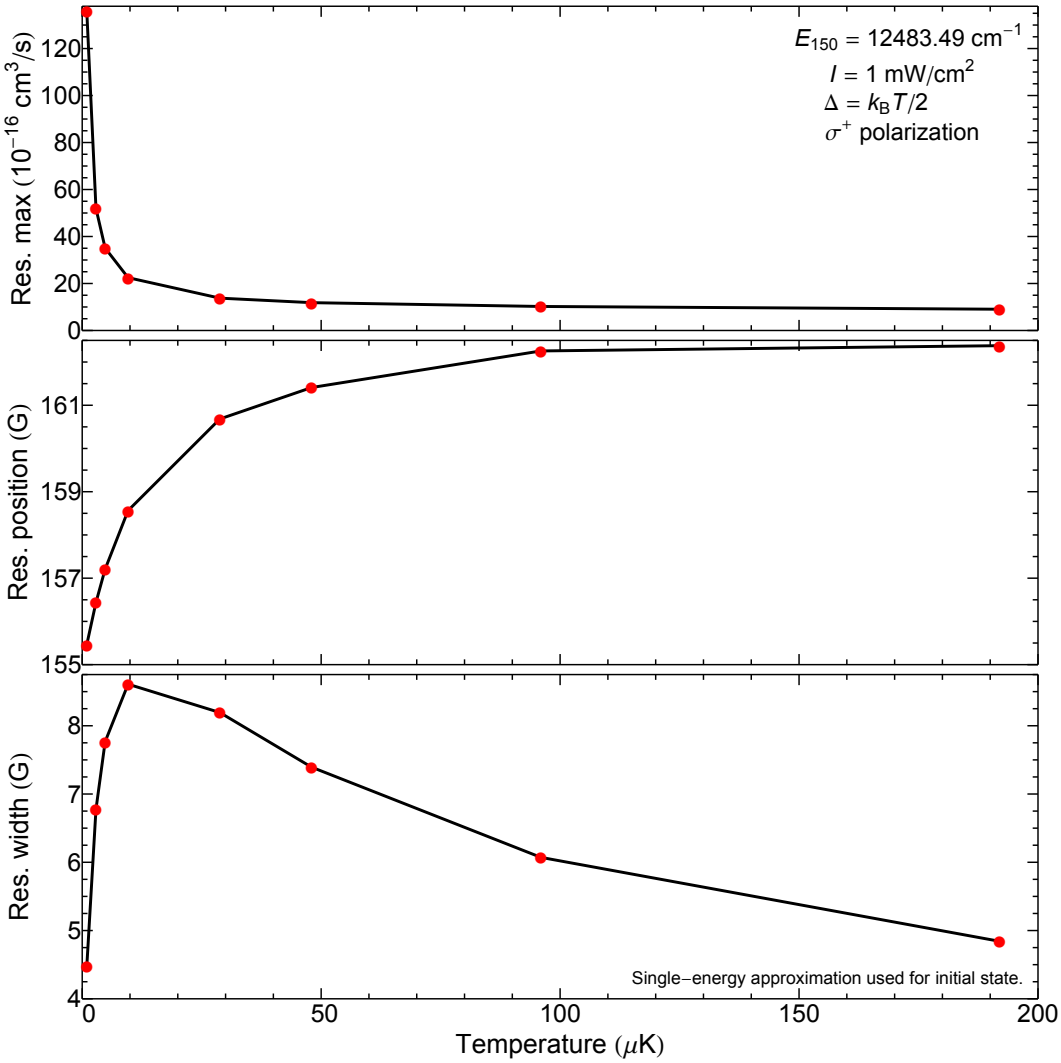

Figure 5.13: The effects of the temperature of the atoms trapped in the FORT on the resonance maximum signal, the resonance position, and the resonance width for the ν=150 state as calculated by [2]. From the theory, we suspect that the temperature of our FORT is over 100 μK for most of the trials.

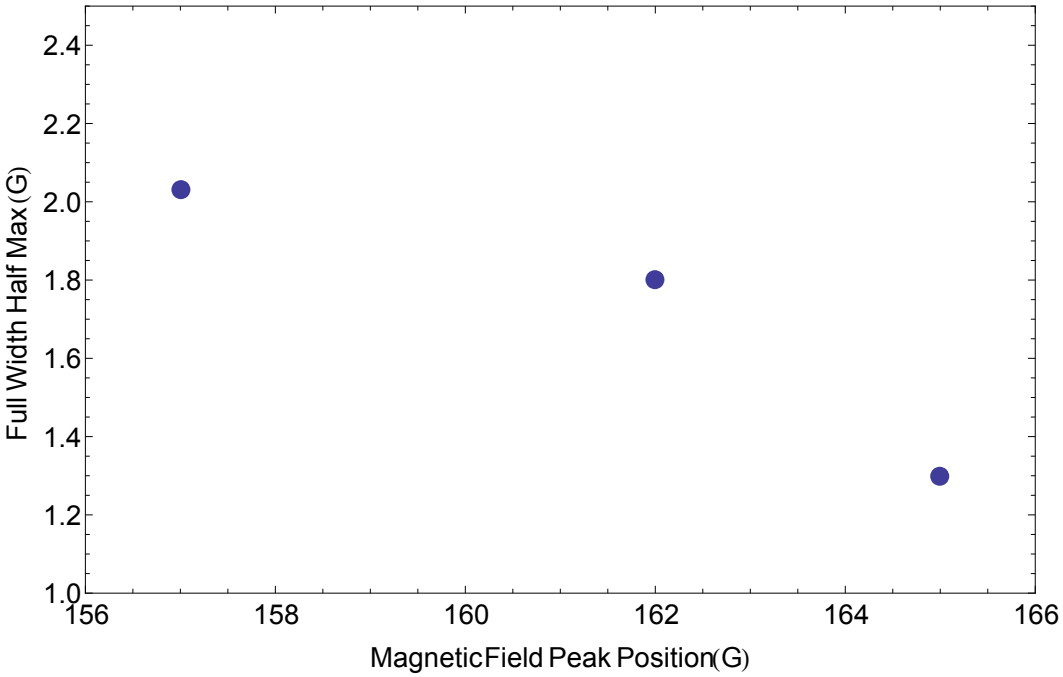

Figure 5.14: The change in the full width at half the maximum of the FOPA resonance versus the position of the peak. A larger peak position is indicative of a larger temperature, which would suggest a smaller full width at half max. This trend is seen in the graph.

We searched multiple transitions, but only saw clear evidence at these three frequencies. We believe we did not see transitions at the other frequencies due to a variety of factors, including PA laser drift, FORT atom loading fluctuations, and a limited number of data sets. More data on a number of transitions will be taken in the near future to explore the transitions more thoroughly. Also, other improvements include a colder sample and a higher density. As seen in Figures 5.12 and 5.13, a colder sample significantly increases the PA rate. Since we suspect that our sample is somewhere near 200 μK, decreasing to 10 μK would lead to an order of magnitude increase in the signal. A possible avenue to reach this temperature is to trap not with an optical trap, but a magnetic trap. This also allows for the atoms to be trapped in a specific magnetically trappable state, such as the $|\mathrm{F}{=}2,\ \mathrm{m}_F{=}2\rangle$, that should lead to a higher signal as all the atoms would undergo the Feshbach resonance. To increase the density while continuing with an optical trap, the beam used for the FORT can be re-directed and focused to form a crossed dipole trap. This will lead to a reduced atom number, but significantly higher atom density.

Chapter 6

Conclusions

This work is a step towards measuring the complete vibrational structure of the 0_g^- excited molecular state. One of the major motivations for measuring the vibrational structure of potential curves is the goal of improved efficiency in the creation and control of cold molecules. Molecules offer extra degrees of freedom as compared to atoms. Cold molecules offer properties to manipulate such as the dipole moment, the rotational structure, and Lambda doublet systems that can be used for quantum computation [5, 6] and quantum memory [7]. Molecules with large polarizabilities can create degenerate Fermi gases with strong anisotropic interactions, which could lead to information on Bardeen-Cooper-Schreefer (BCS) condensation [8]. Cold molecules can be used for coherent control of chemical reactions [8, 9, 10]. They can also be used in tests of fundamental symmetries such as parity and time reversal [11, 12, 13], and in the variation of fundamental constants [14, 15, 16].

We observe 3 different FOPA resonances at 12323 cm^{-1}, 12425 cm^{-1}, and 12483 cm^{-1}, corresponding to the vibrational levels ν=127, ν=140, and ν=150. This is the first measurement of FOPA in $^{85}Rb_2$ this deep into the well in an optical dipole

trap. The experimental and theoretical positions matched to within the linewidth of the laser. The full width at half the maximum for each of the transitions is near 2 G, which is approximately 2.5 to 3 times smaller than the expected width from our theoretical calculations [2] and previous experiments [58]. We attribute the width to uncertainties in the exact magnetic field, a small number of data sets, and the large linewidth of our photoassociation laser. We see a variation in the magnetic field position of the peak fractional loss. We believe this movement is due to fluctuations in the temperature of the FORT. Our theory predicts a significant difference between the PA rates for different polarizations of the laser field; however, we do not observe a difference. A possible explanation is that we do not have pure polarization of the PA laser because of its orientation with respect to the magnetic field. Also, we do not have enough statistics and there are too many variables to be conclusive.

We present the design of a zero-crossing Zeeman slower for ^{85}Rb using rings of flexible permanent magnets. The design is inexpensive, requires no power or cooling, and can be easily attached and removed for vacuum maintenance. We show theoretically that such a design can reproduce a magnetic field profile of a standard zero-crossing Zeeman slower. Experimental measurements of a prototype and comparisons to theoretical simulations demonstrate the feasibility of the design and point toward future improvements. Simulations show an atom flux similar to other Zeeman slowers. Ultimately, we did not implement the Zeeman slower in our

system because of the large magnetic field deviations from the expected magnetic field profile.

We also show the first operation of a dipole trap at 808 using a higher power low cost multi-mode laser diode. Normal optical dipole traps can be very expensive to set-up and difficult to align if they are outside the visible or near infrared. We have designed an inexpensive system for use in undergraduate teaching laboratories using a 4 W multi-mode laser that cost less than $100. We have formed a far off resonance trap (FORT) using the 808 laser and imaged the FORT via fluorescence imaging. We did not have the optics set up at the time to investigate it with absorption imaging, and we are unable to speak to the atom number or densities. We are working to make the set up easier and study it with absorption imaging.

The experiment is very promising as it moves forward, but there will be multiple changes. The vacuum system has been failing, leading to limits on the density of the MOT and FORT. A new system would have a lower vapor pressure, leading to longer lifetimes in the optical dipole trap and hopefully higher densities. It could also be loaded by a Zeeman slower to maintain a pressure differential, and create quick and efficient loading of the MOT. A second issue is the limitations placed on the system from the glass vacuum cell and its high reflectivity. We are unable to implement a Dark Spot MOT because of the high reflectivity of the glass. This leads to re-pump light being present in all areas of the MOT. As seen by our flat top MOT, we are radiation pressure limited, which effects the transfer efficiency

into the MOT.

Because the system needs to be upgraded, the system will most likely move to a magnetic trap. The specific state we are observing, the $|F = 2, m_F = -2\rangle$ is magnetically trappable. The atoms can be loaded from a MOT, transfered in a magnetic trap, and then moved to the magnetic field for the Feshbach resonance. A magnetic trap would allow us to have a lower temperature while having a high intensity photoassociation laser. Using a single laser for both driving a photoassociation transition and forming an optical dipole forces the laser beam to be intense and near resonance, leading to warm atoms. The lower temperature from a magnetic trap could increase the PA rate by an order of magnitude. Alignment will also be easier, because the magnetic coils for both the magnetic field trap and MOT can be overlapped, ensuring the MOT is aligned with the magnetic trap.

The Ti:S will also be upgraded to have a narrower linewidth. A typical PA resonance has a width in the tens of MHz. Sub-MHz linewidth Ti:S lasers are now common, and will lead to well resolved FOPA resonances. It will also lead to a much improved measurement of the PA lines for ^{85}Rb without using FOPA. As mentioned, the most recent survey of the PA lines above the D1 line is from the 90's. The advancements in laser technology make a better measurement of the PA positions and widths a more much attainable goal.

Bibliography

[1] Dalibard, J. and Cohen-Tannoudji, C. *Optical Society of America* **6**(11) (1989).

[2] Dizikies, J. *Theoretical Study of Feshbach Optimized Photoassociation in* $^{85}Rb_2$. PhD thesis, University of Oklahoma, (2015).

[3] Bell, S. C., Junker, M., Jasperse, M., Turner, L. D., Lin, Y.-J., Spielman, I. B., and Scholten, R. E. *Review of Scientific Instruments* **81**(1), 013105 (2010).

[4] Semczuk, M., Li, X., Gunton, W., Haw, M., Dattani, N., Witz, J., Mills, A., Jones, D., and Madison, K. *Phys. Rev. A* **87**(052505) (2013).

[5] Zadoyan, R., Kohen, D., Lidar, D., and Apkarian, V. *Chemical Physics* **266**(323), 2–3 (2001).

[6] DeMille, D. *Phys. Rev. Lett.* **88**(067901) (2002).

[7] Rabl, P., DeMille, D., Doyle, J., Lukin, M., Schoelkopf, R., and Zoller, P. *Phys. Rev. Lett.* **97**(033003) (2006).

[8] Carr, L., DeMille, D., Krems, R., and Ye, J. *New Journal of Physics* **11**(055049) (2009).

[9] Buchler, H., Demler, E., Lukin, M., Micheli, A., Prokofev, N., Pupillo, G., and Zoller, P. *Phys. Rev. Lett.* **98**(060404) (2007).

[10] Krems, R. *Phys. Chem. Chem. Phys.* **10**(4079) (2008).

[11] Hudson, J., Sauer, B., Tarbutt, M., and Hinds, E. *Phys. Rev. Lett.* **89**(023003) (2002).

[12] Shafer-Ray, N. *Phys. Rev. A* **73**(34102) (2006).

[13] Hudson, J., Kara, D., Smallman, I., Sauer, B., Tarbutt, M., and Hinds, E. *Nature* **476**(493) (2011).

[14] Hudson, E. R., Lewandowski, H., Sawyer, B., and Ye, J. *Phys. Rev. Lett.* **96**(143004) (2006).

[15] Kozlov, M. G. *Rhys. Rev. A* **80**, 2 (09).

[16] Chin, C., Flambaum, V. V., and Kozlov, M. G. *New Journal of Physics* **11**(055048) (2009).

[17] Barry, J. F., McCarron, D. J., Norrgard, E. B., Steinecker, M. H., and DeMille, D. *Nature* **512**, 286–289 (2014).

[18] Abraham, E. R. I., McAlexander, W. I., Sackett, C. A., and Hulet, R. G. *Phys. Rev. Lett.* **74**(1315) (1995).

[19] Bahns, J. T., Gould, P. L., and Stwalley, W. C. *Advances in Atomic, Molecular, and Optical Physics* **42**(172) (2000).

[20] Aziz, S., Aymar, M., and Dulieu, O. *Eur. Pys. J. D* **31**(195) (2004).

[21] Tiemann, E. *Cold Molecules*, chapter 4, 179–200. Wiley-VCH (2009).

[22] Stwalley, W. and Wang, H. *Journal of Molecular Spectroscopy* **195**(194-228) (1999).

[23] Viteau, M., A, C., Allegrini, M., Bouloufa, N., Dulieu, O., Comparat, C., and Pillet, P. *Science* **321**(232) (2008).

[24] Vala, J., Dulieu, O., Masnou-Seeuws, F., Pillet, P., and Kosloff, R. *Phys. Rev. A* **63**(013412) (2001).

[25] Luc-Koenig, E., Kosloff, R., Masnou-Seeuws, F., and Vatasescu, M. *Phys. Rev. A.* **70**(033414) (2004).

[26] Brown, B. L., Dicks, A. J., and Walmsley, I. A. *Phys. Rev. Lett.* **96**(173002) (2006).

[27] Koch, C. P., Kosloff, R., and Masnou-Seeuws, F. *Phys. Rev. A* **73**(043409) (2006).

[28] Homer, A. and Roberts, G. *Phys. Rev. A* **78**(053404) (2008).

[29] Koch, C. P., Ndong, M., and Kosloff, R. *Faraday Discuss* **142**(389) (2009).

[30] Koch, C. P., Luc-Koenig, E., and Masnou-Seeuws, F. *Phys. Rev. A* **73**(033408) (2006).

[31] Mur-Petit, J., Luc-Koenig, E., and Masnou-Seeuws, F. *Phys. Rev. A* **75**(061404) (2007).

[32] Kurznetsova, E., Pellegrini, P., Cote, R., Lukin, M. D., and Yelin, S. F. *Phys. Rev. A* **78**(021402) (2008).

[33] Shapiro, E. A., Shapiro, M., Pe'er, A., and Ye, J. *Phys. Rev. A* **75**(013405) (2007).

[34] Kohler, T., Goral, K., and Julienne, P. S. *Rev. Mod. Phys.* **78**(1311) (2006).

[35] Ni, K. K., Ospelkaus, S., de Miranda, M. H. G., Pe'er, A., Neyenhuis, B., Zirbel, J. J., Kotochigova, S., Julienne, P. S., Jin, D. S., and Ye, J. *Science* **322**(231), 5899 (2008).

[36] Ospelkaus, S., Pe'er, A., Ni, K. K., Zirbel, J. J., Neyenhuis, B., Kotochigova, S., Julienne, P. S., Ye, J., and Jin, D. S. *Nat. Phys.* **4**(622), 8 (2008).

[37] Dulieu, O., Julienne, P. S., and Weiner, J. *Phys. Rev. A* **49**(607) (1994).

[38] Jones, K., Tiesinga, E., Lett, P., and Julienne, P. *Reviews of Modern Physics* **78**, 483–535 (2006).

[39] Abraham, E. *Photoassociative spectroscopy of collisions between ultracold lithium atoms.* PhD thesis, Rice University, (1996).

[40] Townes, C. H. and Schawlow, A. L. *Microwave Spectroscopy.* McGraw-Hill Book Company, Inc., (1955).

[41] Bergeman, T.

[42] Movre, M. and Pichler, G. *Journal of Physics B: Atomic, Molecular and Optical Physics* **10**(2631) (1977).

[43] Harold Metcalf, P. v. d. S. *Laser Cooling and Trapping.* Springer, (2001).

[44] Lett, P., Watts, R., Westbrook, C., Phillips, W., Gould, P., and Metcalf, H. *Phys. Rev. Lett.* **61**(169) (1988).

[45] Raab, E., Prentiss, M., Cable, A., Chu, S., and Pritchard, D. *Physical Review Letters* (1987).

[46] Grimm, R., Weidemuller, M., and Ovchinnikov, Y. *Advances in Atomic, Molecular, and Optical Physics* **42**(95-170) (2000).

[47] Crepaz, H. *Trapping and cooling rubidium atoms for quantum information.* PhD thesis, University of Innsbruck, (2006).

[48] Miller, J. D., Cline, R. A., and Heinzen, D. J. *Phys. Rev. Lett.* **71**(14) (1993).

[49] Bahaa Saleh, M. T. *Fundamentals of Photonics.* Wiley- Interscience, (2007).

[50] Kuppens, S., Corwin, K., Miller, K., Chupp, T., and Wieman, C. *Physical Review A: Atomic, Molecular, and Optical Physics* **62**(013406) (2000).

[51] Lett, P., Julienne, P., and Phillips, W. *Ann. Rev. Phys. Chem.* **46**, 423–452 (1995).

[52] Chakraborty, D., Hazra, J., and Deb, B. *Journal of Physics B: Atomic, Molecular and Optical Physics* (2011).

[53] Chin, C., Grimm, R., Julienne, P., and Tiesinga, E. *Reviews of Modern Physics* **82**, 1225–1286 (2010).

[54] Claussen, N. R. *Dynamics of Bose-Einstein condensates near a Feshbach resonance in Rb.* PhD thesis, University of Colorado, (2003).

[55] Roberts, J. *Bose-Einstein Condensates with Tunable Atom-atom Interactions: The First Experiments with Rb BEC.* PhD thesis, University of Colorado, (2001).

[56] Claussen, N., Kokkelmans, S., Thompson, S., Donley, E., Hodby, E., and Wieman, C. *Phys. Rev. A* **67**(060701(R)) (2003).

[57] Ogilvie, J. *Academic Press* (1998).

[58] Courteille, P., Freeland, R., Heinzen, D., Abeelen, F., and Verhaar, B. *Phys. Rev. Lett.* **81**(1), 69–72 (1998).

[59] Tolra, B., Hoang, N., Jampens, B. T., Vanhaecke, N., Drag, C., Crubellier, A., Comparat, D., and Pillet, P. *Europhys Lett* **64**(171) (2003).

[60] Pellegrini, P., Gacesa, M., and Cote, R. *Phys. Rev. Lett.* **101**(053201) (2008).

[61] Deiglmayr, J., Pellegrini, P., Grochola, A., Repp, M., Cote, R., Dulieu, O., Wester, R., and Weidmuller, M. *New J. Phys.* **11**(055034) (2009).

[62] P. Pellegrini, R. C. *New J. Phys.* **11**(055047) (2009).

[63] Gacesa, M. and Cote, R. (2014).

[64] O'Hanlon, J. *A User's Guide to Vauum Technology.* John Wiley and Sons, (1989).

[65] Lewandowski, H. *Coherences and correlations in an ultracold Bose gas.* PhD thesis, University of Colorado, (2002).

[66] Carl Wieman, L. H. *Rev. Sci. Instrum* **62**(1) January (1990).

[67] Overstreet, K., Franklin, J., and Shaffer, J. *Rev. Sci. Instrum.* **75**(4749) (2004).

[68] Corwin, K. *A Circularly Polarized Optical Dipole Trap and Other Developments in Laser Trapping of Atoms*. PhD thesis, University of Colorado, (1997).

[69] Schwettmann, A. *Atom Chip Setup for Cold Rydberg Atom Experiments*. PhD thesis, University of Oklahoma, (2012).

[70] Monroe, C., Swann, W., Robinson, H., and Wieman, C. *Phys. Rev. Lett.* **65**, 1571–1574 Sep (1990).

[71] Phillips, W. D. and Metcalf, H. *Phys. Rev. Lett.* **48**, 596–599 Mar (1982).

[72] Barrett, T. E., Dapore-Schwartz, S. W., Ray, M. D., and Lafyatis, G. P. *Phys. Rev. Lett.* **67**, 3483–3486 Dec (1991).

[73] Metcalf, H. J. and van der Straten, P. *Laser Cooling and Trapping*. Springer-Verlag New York, Inc, (1999).

[74] Cheiney, P., Carraz, O., Bartoszek-Bober, D., Faure, S., Vermersch, F., Fabre, C., Gattobigio, G., Lahaye, T., Guery-Odelin, D., and Mathevet, R. *Rev Sci Instrum* **82**(6), 063115 (2011).

[75] Ovchinnikov, Y. B. *Optics Communications* **276**(2), 261 – 267 (2007).

[76] Ovchinnikov, Y. B. *Eur. Phys. J. Special Topics* **163**, 95–100 (2008).

[77] Reinaudi, G., Osborn, C., Bega, K., and Zelevinsky, T. *J. Opt. Soc. Am. B.* **29**(729-731) (2012).

[78] Lebedev, V. and Weld, D. http://arxiv.org/abs/1407.5372.

[79] Dedman, C. J., Nes, J., Hanna, T. M., Dall, R. G., Baldwin, K. G. H., and Truscott, A. G. *Review of Scientific Instruments* **75**(12), 5136–5142 (2004).

[80] Krzyzewski, S. P., Akin, T. G., Dahal, P., and Abraham, E. R. I. http://nhn.nhn.ou.edu/∼abe/research/FOPA/index.html.

[81] Perigo, E., Faria, R., and Motta, C. *IEEE Transactions of Magnetics* **43**, 3826–3832 (2007).